technische universität
dortmund

Fakultät Physik
Experimentelle Physik 2
Otto-Hahn-Straße 4a
D-44227 Dortmund
www.e2.physik.tu-dortmund.de

Nuclear spin dynamics of donor-bound electrons in GaAs

Dissertation
presented to the Faculty of Physics of the
TU Dortmund University, Germany,
in partial fulfillment of the requirements
for the degree of Doktor rer. nat.
by

Pavel Sokolov

Supervised by

Prof. Dr. Dmitri Yakovlev

Assistant Supervisor

Dr. Mikhail Petrov

Accepted by the Faculty of Physics of the TU Dortmund University, Germany

Examination board:
Prof. Dr. Dmitri Yakovlev
Prof. Dr. Dieter Suter
Prof. Dr. Götz S. Uhrig
Dr. Dominik Elsässer

Dortmund, 2020

experimentelle
physik 2

Pavel Sokolov
Campus Nord, Experimentelle Physik 2a
Technische Universität Dortmund
Otto-Hahn-Straße 4a
D-44227 Dortmund

I would like to thank all the people who have supported me during my Ph.D. studies!

First of all, I would like to thank the head of Experimentelle Physik 2a Prof. Dr. Manfred Bayer for giving me the opportunity to perform these studies in one of the best-equipped labs.

I am very grateful to my scientific supervisor Prof. Dr. Dmitri Yakovlev for the guidance, fruitful discussions and invaluable help.

Furthermore, I would like to thank Dr. Mikhail Petrov and Dr. Kirill Kavokin at Saint Petersburg State University for productive collaboration, which resulted in several published papers, experimental insights and many fruitful discussions. As well as Prof. Dr. Sergey Verbin and Dr. Maria Kuznetsova at Saint Petersburg State University and Dr. Mladen Kotur at the Ioffe Institute for outstanding support and assistance during the experimental research and preparation of the publications.

I am grateful to Prof. Dr. Ivan Ignatiev at Saint Petersburg State University for introducing me to the experimental methods used in this work and for helping me with my first steps in the new lab environment.

I thank Prof. Dr. Dieter Suter for carefully proofreading the entire manuscript and his feedback on it.

I would like to thank all my colleagues and friends in our office (Alexey Danilov, Dr. Daniel Schmidt, Bernd Berger, Dr. Johannes Thewes, Gang Qiang and Walter Warkentin) for the good working atmosphere and having a nice and interesting time.

I would like to thank Lars Wieschollek and Thomas Stöhr for their excellent technical support. Special thanks to Michaela Wäscher and Katharina Sparka for their great administrative support. They very patiently solve and explain all administrative affairs that I encountered throughout my work at the TU Dortmund.

Finally, I want to thank all other recent and former members of E2 for the great and friendly atmosphere. Thank You all very much!

Contents

1 Introduction

The scope of this work is the nuclear spin dynamics of the donor-bound electron in gallium arsenide (GaAs). This dynamics has been studied experimentally by optical spectroscopy concerning two aspects, time-resolved Hanle effect, and three-stage experimental protocol including optical pumping and measuring the difference of the nuclear spin polarization before and after a dark interval of variable length. For an overview, a short introduction to the electron-nuclear spin physics and scientific relevance of the conducted studies will be given.

1.1 Survey of electron-nuclear spin physics in semiconductors

The first step in the study of spin-dependent phenomena was made by Robert Wood in 1924 when even the concept of electron spin had not existed. In a pioneering article, the initially observed high degree of polarization of mercury vapor fluorescence resonantly excited by polarized light was discovered by Wood and Ellett [WE24]. In this paper, they discovered a phenomenon that is well known nowadays as the Hanle effect (i.e., depolarization of the luminescence by the transverse magnetic field). From a classic point of view, the reason for this effect is the decrease in the average projection of the electron spin on the direction of the observation axis. At continuous polarized light excitation, this precession leads to a decrease of the circular polarization degree of the luminescence as a function of the transverse magnetic field [Dya17]. Usually, the Hanle effect is measured as the dependence of polarization on the external transverse magnetic field. After this, Hanle was carried out detailed studies of this phenomenon and provided the quantitative physical description [Han91].

Spin physics research did not receive much attention until 1949, while Kastler and Brossel started the first studies of optical orientation processes in atomic vapors [Dya17]. The experimental approaches and ideas, which are widely used nowadays in the modern semiconductor spintronics, originate from these first experimental works. Examples of such approaches are the creation of a non-equilibrium distribution of atomic angular moments by optical excitation, manipulating this distribution by applying *dc* or *ac* magnetic fields, and detecting the result by studying the luminescence polarization. As it was shown, the relaxation times for the atomic angular moment decay can be very long, especially in the case when hyperfine splitting is significant due to the involvement of the nuclei [Dya17]. In the field of atomic vapor physics, a deep understanding of spin-related phenomena was very useful for laser physics development. After some time of the research in the spin physics of semiconductors, many important applications have been born, such as gyroscopes and wide-range magnetometers, etc.

The first observation of optical orientation in a semiconductor was done in 1968 by Georges Lampel [Lam68]. A pleasant surprise was that free conduction band electrons (holes) that get spin-polarized, as opposed to atom-bonded electrons. However, it was sufficient for the polarization of the lattice nuclei even though the degree of electron polarization was still small. The nuclear spin polarization was detected by a conventional NMR technique. These successful measurements were continued at Ioffe Institue in St. Petersburg and Ecole Polytechnique in Paris, from the seventies of the twentieth century.

The main feature of the electrons and nuclei in semiconductors reveals itself in the processes of electron spin relaxation due to the interactions with nuclei, which do not have counterparts in atomic vapors, where atomic spin polarization also relaxes due to collisions between atoms, the exchange interactions and primarily due to collisions with the wall of cuvette where the vapors are inclosed. The crucial physical reason for interactions between nuclei and electron consists in the fact that, usually, each electron is covered or spread over a region with a large number ($\sim 10^5$) of surrounding nuclei [MZ12], which, in turn, permits one to joint actions of the polarized nuclei on the electron spin in terms of averaged nuclear field (also called as an Overhauser field) of polarized spins. In principle, this nuclear field can reach as large as 5.3 T for GaAs [SFK+01]. It should also be noted that the longitudinal nuclear-spin relaxation time observed in semiconductor crystals is much longer compared to atomic vapors.

The general methods of optical spin orientation borrowed from similar to those from atom study were successfully used for determining basic parameters, i.e., the photoexcited electron lifetime and spin relaxation time, the g-factor, and the parameters of the spin-orbit and hyperfine interactions. To the current state of spin physics in semiconductors, several relatively new optical methods are still providing new insights on the optical orientation processes [HB16]. Also, an in-depth analysis of the circular polarization degree of the recombination photons is GaAs-based structures allowed to discover a large number of physical phenomena providing substantial evidence of nonlinear behavior of the electron-nuclear spin system. The most striking examples of such phenomena can be bistability, hysteresis, and undamped oscillations of the PL circular polarization degree [MZ12].

Recently, the spin physics of electrons and nuclei in semiconductors continues to reveal new bright phenomena, mainly in advanced nanostructures [Dya17, UMA+13]. However, even in otherwise very well studied bulk semiconductor materials, like GaAs, the understanding of the electron-nuclear spin dynamics, first discovered in the 1970s [PLSS77] (see also [MZ12]) has considerably progressed during recent years [KDV+16, VCS+17, Sca17]. The application of modern optical techniques like Faraday rotation [GCG+13], spin noise [RKS+16], and time-resolved photoluminescence [SPK+17], combined with more traditional techniques of magneto-optical spectroscopy and NMR [ES04], allowed identifying the underlying mechanisms of spin and energy relaxation in the intertwined spin systems of nuclei and resident charge carriers [VCS+17].

1.2 Motivation and scope of the research

Modern computer processors are nowadays approaching limits due to their quantum limitations. The conventional electronics is based on measuring the small electrical charge of electrons passing through electronic circuits. An alternative approach based on novel materials could be the solution, which instead relies on the fundamental quantum-mechanical property a spin.

In the last two decades, many researchers are strongly motivated by the fascinating prospects of manipulating and controlling sophisticated quantum systems and potential applications of quantum information computation. The basic requirements that apply to a device based on quantum bits include the ability to scale a quantum bit system, simplicity of creating and reading of the quantum state, long coherence time, and universal set of quantum gates. Given these considerations, there have been numerous attempts to control and create qubits in different systems: quantum flux in superconductors, electronic states of ions and atoms, the polarization state of photons, electron and nuclear spin in semiconductor quantum dots and molecular systems. Concerning nuclear and electron spin states are of particular interest in the field of solid-state qubits manipulating where individual charge and spin carriers can be strongly decoupled from their environment so that the processes destroying the quantum coherence in bulk are largely suppressed [HB16].

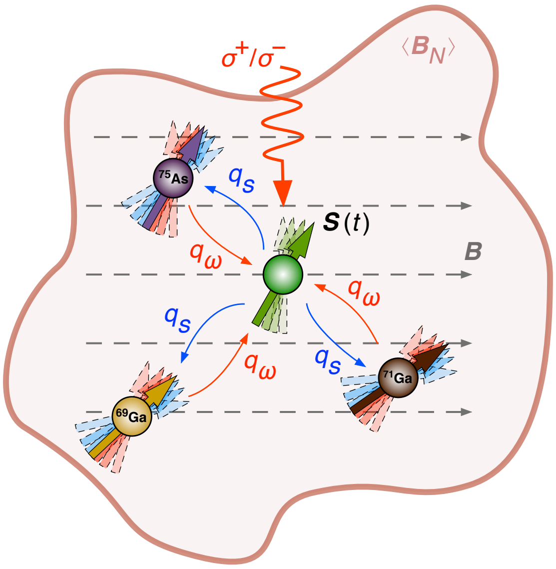

Figure 1.1: Sketch showing the electron-nuclear spin system of the n-doped GaAs including 3 different lattice isotopes (^{71}Ga, ^{69}Ga and ^{75}As) and interactions within it.

Electron spin in the solid body can be compared with the Earth turning around its axis while rotating about the Sun and having a spin either "up" or "down". On the other hand, the traditional electronic devices (for example, an ordinary semiconductor transistor) use the charge to represent the operating information as zeros and ones. In the case of *spin*tronics, the two-electron spin state can be used to represent the quantum bit of information, which can be measured because it generates a tiny magnetic field. To read such a quantum bit, many different experimental methods and approaches can be used, from purely optical to electrical, with various combinations possible [HB16].

Recent studies of the doped semiconductors have demonstrated coherent electron spin-transfer already over macroscopic distances with spin coherence time exceeding several hundreds of nanoseconds [KA98, KA99a]. Such materials can be potentially used as building blocks for spintronic devices. It is worth mentioning the fact that the spin injection into a semiconductor has proved difficulty, pushing forward the only successful approach involves a classical injection of spins from magnetic semiconductors[MBSA01, OYB$^+$99]. Moreover, strange as it may sound, but in more than half a century of research into the processes of relaxation of the angular momentum of nuclear spins in doped semiconductors, the significant blank spaces in such an exciting area of physics have not filled. Many questions that could not be answered before, at the moment, could be explored with the advent of new and more advanced physical devices and experimental methods. A part of this actively developed field is the physics of relaxation processes in the spin system of interacting localized electrons in n-type GaAs is the subject of this dissertation. GaAs is a vital semiconductor and already commonly used to manufacture devices such as infrared emitting diodes, laser diodes, integrated circuits at microwave frequencies, and photovoltaic cells.

This work is concentrated on the nuclear spin system (NSS) in GaAs. The one main focus area of this dissertation can be defined. It is optical manipulation of the nuclear spin ensemble interacting with a donor-bounded electron in n-type GaAs. Special attention in carrying out the research was given to the detailed study of the nuclear spin relaxation times under a wide range of controlled physical conditions of the experiments. Since the optical operation of a mesoscopic nuclear spin ensemble is a complex and nonlinear process that involves transferring the angular momentum and energy between nuclear spins and optically-oriented localized electrons (see figure 1.1), the fundamental optical methods and initial experimental ideas that were formed a structure of this dissertation trace back to the studies of spin-related phenomena in atomic vapors (as mentioned in section 1.1).

2 Theoretical background

The Gallium Arsenide (GaAs) is a compound of the two chemical elements gallium (Ga) and arsenic (As). Thanks to a successful combination of properties, GaAs takes second place after silicon in modern electronic technology. The creation of GaAs-based devices began in the early 1950s. In 1952, two significant results were obtained: Shockley invented a field-effect transistor, and Welker suggested to use $A^{III}B^{V}$ compounds as a semiconductor in electronic devices [SCK00]. The key advantages of GaAs over Si is higher saturated electron drift velocity and low field mobility than Si. This leads to faster-operated devices [SN06]. In the early 60s, the most common microelectronic devices were bipolar transistors. The first GaAs transistors were described in 1961 by the American scientists M. Jones and E. Wurst [EW14]. GaAs was the first compound semiconductor to extend the frequency of operation of active devices beyond what was possible with Si. GaAs components first started to make a significant impact on the commercial wireless markets in the early 1990s [EW14].

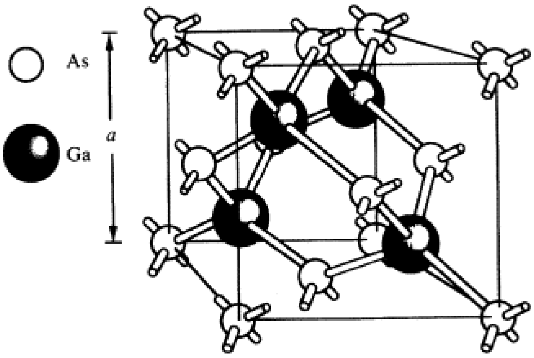

Figure 2.1: Zincblende structure of GaAs showing the relative positions of arsenic and gallium atoms [McL86].

GaAs crystallizes in the zincblende lattice with the gallium and arsenic atoms, each occupying sites on one of the two face-centered-cubic (f.c.c.) sublattices that make up this structure. A unit cell of this material is shown in figure 2.1. One can see that each arsenic atom has four gallium nearest neighbors, and each gallium atom has four arsenic nearest neighbors arranged in a tetrahedral structure. The dimension of the conventional unit cell is 0.565325 nm at room temperature, and the density of this material is 5.32 gcm^{-3} [McL86].

The energy bandgap of GaAs tends to decrease as the temperature is increased. This is caused by the fact that the interatomic spacing expands when the amplitude of the atomic vibrations increases due to the higher thermal energy. This effect is described by the material linear expansion coefficient. An enlarged interatomic spacing reduces the potential energy barrier seen by the electrons, which in turn reduces the value of the GaAs energy bandgap $E_\mathrm{g} = 1.441$ eV (at 300 K).

2.1 GaAs band structure

GaAs is a promising technology platform and has already demonstrated successful applications as a key component, including waveguide integrated single-photon sources and integrated single-photon detectors. At present, GaAs is widely used in research for a better understanding of future semiconductor quantum circuits capable of manipulating quantum states with light.

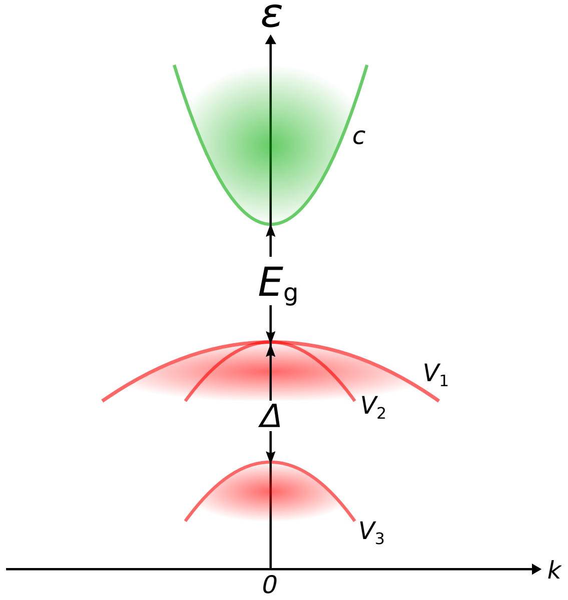

Figure 2.2: Simplified GaAs band structure at Γ – point, where c is conduction band, ϵ is energy, V_1 is heavy-hole (hh) band, V_2 is light-hole (lh) band and V_3 is split-off (so) band. Here, $\Delta = 0.34$ eV is the split off band energy and E_g is band gap.

The band structure of GaAs is well known. The bottom of the conduction band and the top of the valence band are situated at the center of the Brillouin zone (Γ – point.)

The simplified GaAs band structure is schematically shown in Fig. 2.2 without taking into account comparatively small terms caused by the absence of an inversion center. The conduction band (c) is twice spin degenerate, while the valence band consists of three twice degenerate sub-bands, which are hh, lh, and so sub-bands. The minimum and maximum in Fig. 2.2 are associated with Γ_6 representation for conduction band, Γ_8 for hh and lh bands and Γ_7 for so - band respectively. The absence of an inversion center leads to a small spin splitting of the bands and a small shift of the top of the valence band from $\mathbf{k} = 0$. The effect described above is not significant for considering the optical transitions but, at the same time, can significantly affect the process of spin relaxation. Since the energy states of the heavy holes zone are not initially spherical but have a cubic symmetry, it results in the deviation of the hh zone to far from Γ – point. It should be noted that the nonparabolicity of the conduction band is due to its interaction with the valence band. Thus, the nonparabolicity of hh and lh bands is associated with their mutual interaction and significantly affects the selecting rules of optical transitions.

2.1.1 Conduction band

The Bloch function describes the electron state in the conduction band:

$$\psi^c_{\mathbf{k}m} = u_m e^{i\mathbf{k}r}, m = \pm\frac{1}{2}, \tag{2.1}$$

where Bloch amplitudes $u_{\pm1/2}$ differ in direction of the spin:

$$u_{1/2} = S\uparrow, u_{-1/2} = S\downarrow. \tag{2.2}$$

Here S denotes an equal part of the s-type Bloch amplitude and invariant to crystal symmetry transformations.

Near Γ-point energy spectrum is quadratic and isotropic with effective mass m_e:

$$\epsilon_c(\mathbf{k}) = \frac{\hbar^2\mathbf{k}^2}{2m_e}. \tag{2.3}$$

The absence of an inversion center reveals itself as cubic in $\mathbf{k}$ terms in the electron Hamiltonian in the conduction band with taking into account Dresselhaus terms [MZ12]:

$$\hat{H} = \frac{\hbar^2\mathbf{k}^2}{2m_e} + \frac{\hbar}{2}\hat{\sigma}\cdot\Omega(\mathbf{k}), \tag{2.4}$$

where $\hat{\sigma}$ are Pauli matrices, and $\Omega(\mathbf{k})$ is a vector

$$\Omega_x(\mathbf{k}) = \alpha\hbar^2(m_e\sqrt{2m_eE_g})^{-1}k_x(k_y^2 - k_z^2), \tag{2.5}$$

where m_e is the electron effective mass, Ω_y and Ω_z may be substituted from Eq.2.4 by cyclic permutation of indices $\{x, y, z\}$. In this case, the indices coincide with the crystalline axes [100], [010] and [001], and the value of the spin splitting is given by the dimensionless coefficient $\alpha = 6 \times 10^{-2}$ (GaAs). Therefore, an effective magnetic field depending on the quasimomentum acts on the electron spin due to the absence of an inversion center.

2.1.2 Light-hole band, heavy-hole band and split-off band

If the energy is much smaller than spin-orbit splitting Δ (near Γ-point), the four-electron state with defined $\mathbf{k}$ is described with following wave functions:

$$\psi_{KM}^{(1,2)} = e^{i\mathbf{k}\cdot r}\sum_{\mu}\chi_{M\mu}u_{\mu}^{(3/2)}, M = \left\{\pm\frac{1}{2}, \pm\frac{3}{2}\right\}, \tag{2.6}$$

where $M = \pm 3/2$ belong to hh band, $M = \pm 1/2$ to lh band. Index μ changes in range from $\mu = \pm 1/2$ to $\mu = \pm 3/2$. $u_{\mu}^{(3/2)}$ transforms as eigenfunctions of z-component of the angular momentum operator J_z with total value of 3/2. The exact expressions for Bloch amplitudes are

$$\begin{aligned}
u_{3/2}^{(3/2)} &= -\frac{\sqrt{2}}{2}(X+iY)\uparrow, \\
u_{-3/2}^{(3/2)} &= \frac{\sqrt{2}}{2}(X-iY)\downarrow, \\
u_{1/2}^{(3/2)} &= \frac{\sqrt{3}}{3}\left[-\frac{\sqrt{2}}{2}(X+iY)\downarrow + \sqrt{2}Z\uparrow\right], \\
u_{-1/2}^{(3/2)} &= \frac{\sqrt{3}}{3}\left[\frac{\sqrt{2}}{2}(X-iY)\uparrow + \sqrt{2}Z\downarrow\right].
\end{aligned} \tag{2.7}$$

Here (X, Y, Z) is the coordinate part of the Bloch p-type amplitudes transforms as (x, y, z)-coordinates. The energy spectrum with coefficients $\chi_{M\mu}$ can be found from the solution of the following equation

$$\hat{H}\chi_M = \epsilon_M\chi_M, \tag{2.8}$$

where χ_M is the column of the $\chi_{M\mu}$ coefficients with different μ, $\hat{H}$ is the Luttinger Hamiltonian.

For spherical approximation the Luttinger Hamiltonian:

$$\hat{H} = \frac{\hbar^2}{2m_0}(\gamma_1 + \frac{5}{2}\gamma)\mathbf{k}^2 - \frac{\hbar^2}{m_0}\gamma(\mathbf{k}\cdot\mathbf{J})^2, \gamma = (2\gamma_2 + 3\gamma_3)/5, \tag{2.9}$$

where m_0 is the free electron mass, $\gamma_1, \gamma_2, \gamma_3$ are the Luttinger's parametrs and J_x, J_y, J_z are the 4×4 angular momentum matrices.

The energy spectrum of light and heavy holes is given by

$$\epsilon_{hh} = \epsilon_{\pm 3/2} = \frac{\hbar^2\mathbf{k}^2}{2m_{hh}}, \epsilon_{lh} = \epsilon_{\pm 1/2} = \frac{\hbar^2\mathbf{k}^2}{2m_{lh}}, \tag{2.10}$$

where $m_{hh} = m_0/(\gamma_1 - 2\gamma)$ and $m_{lh} = m_0/(\gamma_1 + 2\gamma)$ are hh and lh masses.

If the interaction energy is comparable to the spin-orbit splitting, mixing of states in a light-hole band and split-off band occurs. This mixing results in nonparabolicity of the energy spectrum in these bands. Therefore, the light-hole spectrum takes a form of

$$\epsilon_{V2} = -(A + \frac{1}{2}B)\mathbf{k}^2 + \frac{1}{2}\Delta - \frac{1}{2}(9B^2\mathbf{k}^4 + 2B\Delta\mathbf{k}^2 + \Delta^2)^{1/2}, \tag{2.11}$$

and split-off (so) band

$$\epsilon_{V3} = -(A + \frac{1}{2}B)\mathbf{k}^2 + \frac{1}{2}\Delta + \frac{1}{2}(9B^2\mathbf{k}^4 + 2B\Delta\mathbf{k}^2 + \Delta^2)^{1/2}, \tag{2.12}$$

where A and B quantities are related to the effective masses of light and heavy holes by

$$A = -\frac{\hbar^2}{4}\left(\frac{1}{m_{lh}} + \frac{1}{m_{hh}}\right), B = -\frac{\hbar^2}{4}\left(\frac{1}{m_{lh}} - \frac{1}{m_{hh}}\right). \tag{2.13}$$

It should be mentioned that the situation considered above is valid only when $\epsilon \ll E_g$ and $\Delta \ll E_g$. In particular, in this work the condition when $\epsilon \simeq E_g(\text{GaAs}) = 1.519$ eV at $T = 5$ K is always satisfied.

2.2 Optical orientation in the n-type semiconductors

The reason of the edge luminescence is band-to-band transitions: $c \to hh$ and $c \to lh$. In p-type semiconductors the edge luminescence comes from the recombination of photoexcited electrons with equilibrium holes (which polarization is zero). For high excitation levels, or in n-type material excited holes may participate in the recombination. At excitation with optically polarized light, the average angular momentum of light and heavy holes is 1.25 (in the units $\hbar$); this value can be summed with the average electron spin -0.25 to give unity angular momentum for the absorbed photon [MZ12]. It should be added that due to the strong coupling between the hole quasimomentum and angular momentum in GaAs, the optical orientation rapidly vanishes. It follows that hot holes are oriented and the orientation of thermalized holes is close to zero.

The total intensity of the PL with polarization $\mathbf{k}$ is given by

$$I \sim \int \sum_{mm'M} F_{mm'}\left(D_{m'M}\mathbf{e}\right)\left(D_{mM}\mathbf{e}\right)^{\star} \, \mathrm{d}^3\mathbf{k}, \tag{2.14}$$

where $F_{mm'}(\mathbf{k}) = \sum_M (D_{mM}\mathbf{e})(D_{m'M}\mathbf{e})^{\star}$ is the density matrix of thermalized electrons with unit polarization vector $\mathbf{e}$ (mm' are the spin indices of the electron in the conduction band assuming the values $\pm 1/2$, and summation index M is responsible for two degenerate states in each sub-band of the valence band). If the exciting light is circularly polarized, $\mathbf{e} = (\pm e_x - ie_y)/\sqrt{2}$ where e_x and e_y are unit vectors in the plane perpendicular to the direction of the light beam. In equation 2.14 the quantities $D_{m'M}$ and D_{mM} denote the amplitudes of the dipole moments being equal to the transitions matrix elements $D_{m'M} = \langle m'|\hat{D}|M\rangle$, where index M assumes that values to be $\pm 3/2$ or $\pm 1/2$ for $c \to hh$ or $c \to lh$ transitions and $\hat{D}$ is the dipole moment operator.

It should be noted that the angular momentum conservation is the most crucial part of the optical photo-generation of carriers and optical transitions. Just like elementary particles, the electromagnetic wave has angular momentum. Photons of right or left polarized light carry the angular momentum which projection on the direction of their propagation (helicity) equal to $+1$ or -1 in the units $\hbar$. Linearly polarized photons are in a superposition of these two states.

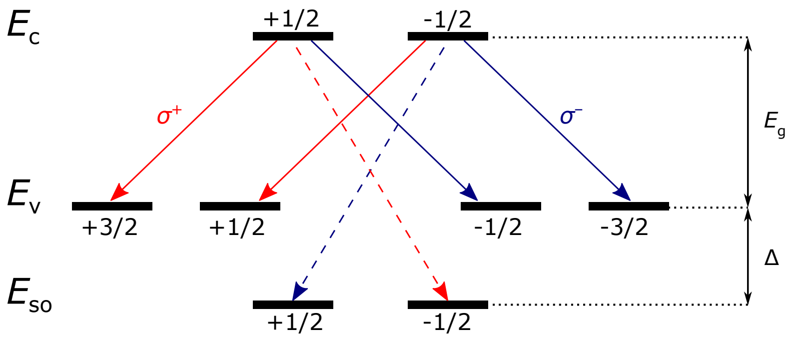

Figure 2.3: Optical transitions between levels with 1/2 and 3/2 spin projections [the bands of light and heavy holes, and the split-off band (E_{so})] and the levels with 1/2 spin projection (the conduction band) during an emission of the polarized photons [MZ12].

In case when circularly polarized light is absorbed, this angular momentum is spread between the photoexcited electron and hole according to the selection rules determined by the semiconductor band structure. Since the valence band E_v has a complex structure, the distribution of the moments depends on the value of the momentum of the created electron-hole pair: p and $-p$. It can be shown that averaging over directions p, the result is the same as in optical transitions between states with $+3/2, +1/2, -1/2, -3/2$ (for light and heavy holes) and $+1/2, -1/2$ (for conduction band E_c). All possible transitions between these states for the absorption of a right circularly polarized light with corresponding relative probabilities are shown in figure 2.3.

2.3 Role of the spin relaxation

It is known that at time $t = 0$ average spin of the thermalized electrons S at constant excitation differs from an average spin of photoexcited electrons S_0. For n-type semiconductor, the electron lifetime τ is several times longer than electron energy relaxation time, and the majority of electrons are thermalized and situated in the conduction band, and spin relaxation time is described by a specific time τ_s [MZ12].

In situation when $\tau_s \gg \tau$ the value of average spin is equal to S_0 and for excitation with $E = \hbar\omega < E_g + \Delta$ (only $hh \to c$ and $lh \to c$ transitions are possible) the limiting value for the polarization is -0.25 (the minus sign is due to the orientation of the average electron spin to the direction of the photon angular momentum).

On the other hand, if $\tau_s \ll \tau$ the optical spin orientation of the electron is nearly completely destroyed during τ and generally, the S dependence on S_0 is given by the following equation

$$S = S_0 \frac{\tau_s}{\tau + \tau_s}. \tag{2.15}$$

The values of τ and τ_s may vary from a sample to sample, depending on the concentration of the impurities, defects, major carriers, and experimental conditions (temperature and magnetic field).

2.3.1 The Hanle effect in GaAs

The depolarization of the electron spins in a transverse magnetic field is known as the Hanle effect. Parsons made the first observations of the Hanle effect in a semiconductor in 1969 [Par69]. Nowadays, this effect is widely used for studying the optical orientation in semiconductors.

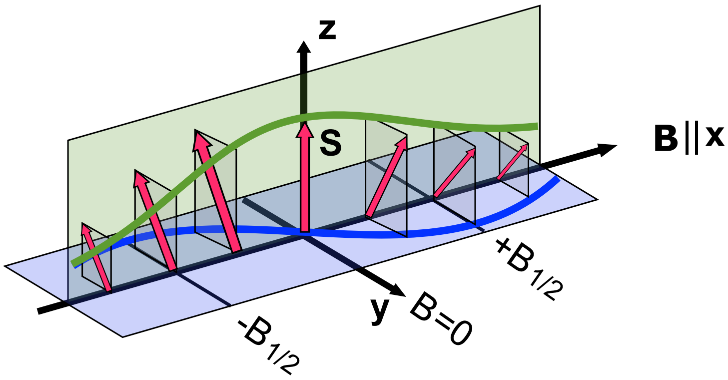

Figure 2.4: The Hanle effect diagram. The Non-Equilibrium Spin Distribution (NESD) that is initially wholly aligned along z-direction with the transverse magnetic field applied along the x-direction. All spins starting to rotate in the yz-plane with Larmor frequency. The transverse magnetic field tilts the NESD in y-direction and the precession induces a dephasing in the spin ensemble, thereby reducing the overall spin polarization and the z-component of the spin polarization by half of its initial value.

The Hanle effect can be understood as an electron spin precession around the magnetic field B with Larmor frequency $\Omega = \mu_B g B/\hbar$ (where μ_B is the Bohr magneton, and g is the electron g-factor). This precession leads to the decrease of the average projection of the electron spin on the direction of the observation, which in turn defines the degree of circular polarization of the luminescence. In case when B_x is perpendicular to the direction of the light wavevector $\mathbf{k}$, the spin component along with the excitation axis changes with frequency Ω and the spin lifetime of the electron is given as

$$\frac{1}{T_s} = \frac{1}{\tau} + \frac{1}{\tau_s}, \tag{2.16}$$

where τ is the electron lifetime in the conduction band and τ_s is the spin relaxation time. Equation 2.16 reflects two causes of spin vanishing: recombination and spin relaxation. In case when the electron suffers many rotations around the magnetic field B during the time T_s, after the establishment of thermodynamic equilibrium the electron polarization S is much smaller than initial polarization $S \ll S_0$. In figure 2.5 the Hanle effect for electron spin S in GaAs is demonstrated.

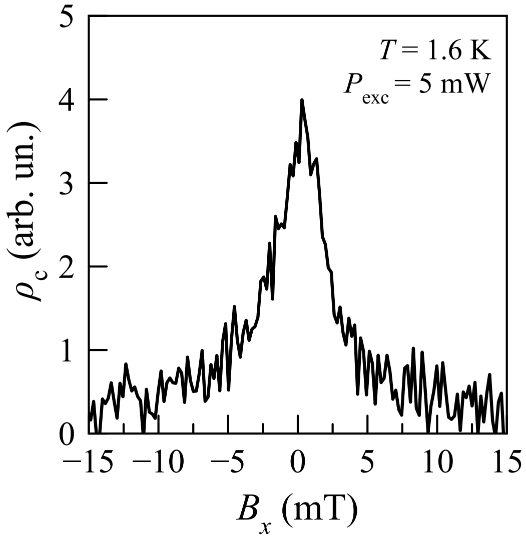

Figure 2.5: Circular polarization degree versus transverse magnetic field (the Hanle effect) for n-type GaAs.

Taking into account statistics of the spin ensemble, after excitation time equal to t the electron spin component reads as

$$S_z = S_0 \cos(\Omega t) \exp(-t/\tau_s). \tag{2.17}$$

Averaging this expression with the function of lifetime destribution, $W(t)$, the equation for S_z takes the following form

$$S_z = S_0 \int_0^\infty W(t) cos(\Omega t) e^{-\frac{t}{\tau_s}} dt, \tag{2.18}$$

where $W(t) = \tau^{-1}\exp(-t/\tau)$ for thermalized electrons. Solution of equation 2.18 gives the well known Hanle equations [MZ12]:

$$S_z(B) = \frac{S_z(0)}{1 + (\Omega T_s)^2}, \ S_z(0) = S_0 \frac{\tau_s}{\tau + \tau_s}. \tag{2.19}$$

The determination of τ and τ_s times is possible after measuring the circular polarization degree in zero magnetic fields and calculating the half-width on the half-maximum (HWHM) of the Hanle curve. After determining $B_{1/2} = \hbar/(g\mu_B T_s)$ one can find τ_s and τ for known electron g-factor.

For n-type GaAs under optical excitation, the electron spin polarization penetrates to the depth of the sample of the order of the spin diffusion length $L = \sqrt{D\tau_s}$ with spin lifetime τ_s characterizing the recombination process in the surface layer and with the speed of spin diffusion D. One of the main features of n-type samples is the fact that one of the processes determining the "spin lifetime" in the surface layer is spin diffusion. Depolarization of electrons leads to a changing gradient of the orientation degree and, therefore, spin diffusion becomes magnetic-field dependent and the shape of the Hanle curve depends on the intensity of the exciting light [MZ12].

2.4 Nuclear spin system

For all GaAs isotopes (^{75}As, ^{71}Ga and ^{69}Ga) forming the NSS and having the spin $I = 3/2$ the following statement is true: NSS is sufficiently isolated from the lattice owing to long spin-lattice relaxation time T_1 (from a sub-seconds to a few days [MZ12]) depending on the lattice temperature and concentration of the paramagnetic impurities [Abr61]. On the other hand, the interactions inside the NSS bath are characterized by much shorter times of about a few milliseconds. The central interaction, in this case, is the dipole-dipole interaction of nuclear magnetic moments, when each nucleus experiences a fluctuating local magnetic field $B_L \sim \mu_I/a^3$ (where a is a lattice constant) created by the surrounding nuclei with magnetic moments μ_I. This field can differ from system to system, but, usually does not exceed a few Gauss. The internal NSS interaction time determines the T_2 time when NSS reaches thermodynamic equilibrium.

In the situation when $B = 0$, the dipole-dipole interaction between nuclear spins does not violate the value of the total nuclear spin and leaves it equal to zero. In the presence of an external magnetic field ($B \neq 0$), the average nuclear spin $\langle I\rangle$ is described by the following expression

$$\langle I\rangle = \frac{I(I+1)}{3}\frac{\mu_I B}{k_B\Theta_N}, \tag{2.20}$$

where Θ_N is the nuclear spin temperature. The detailed description of the nuclear spin temperature concept will be given in chapter 2.6.

The Hamiltonian of the nuclear spin system in an external magnetic field consists of two terms: $H = H_Z + H_d$, where $H_z = (\mu_I/I)B\sum_n \hat{I}_n$ is the Zeeman energy for all nuclei and H_d is the energy of spin-spin interactions. T_2 characterizes the time of effective energy exchange between Zeeman and spin-spin reservoirs at $B \lesssim B_L$ and leading to the establishment of a common spin temperature Θ within the considered system. In case when $B \gg B_L$ the T_2 increases (T_2 can be even longer than T_1), and, it is advisable to describe each of the single parts of NSS two-term Hamiltonian (Zeeman and spin-spin terms) by different temperatures [Gol08].

2.4.1 Overhauser field

In the description of the nuclear spin system in the GaAs, there is the fact that the electron localized on a shallow donor interacts simultaneously with a large number of nuclei. For a shallow donor in GaAs, the Bohr radius is $a_B \approx 10$ nm so that 10^5 lattice nuclei are situated in the localization region of the electron. Under these conditions, the definition of a mean nuclear (Overhauser) field fits very well.

If there is non-equilibrium mean spin polarization of lattice nuclei, the electron is affected by the mean Overhauser field:

$$B_N = \frac{\sum_n A_n \langle I_n \rangle}{\mu_B g}. \tag{2.21}$$

In equation 2.21 the sum runs over all the nuclear isotopes and $\langle I_n \rangle$ is the means spin of these isotopes. For example, the possible total nuclear magnetic field for GaAs is ~ 5.3 T [PLSS77].

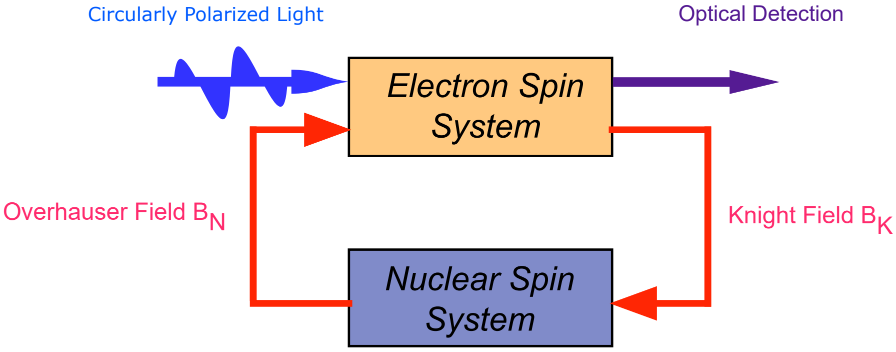

Figure 2.6: Schematics of the process of optical orientation, which consists of the transfer of spin polarization to nuclei from oriented electrons and the effective fields experienced by electrons and nuclei.

Recent studies for GaAs unstressed quantum dots give, in accordance with equation 2.21, the maximum achievable Overhauser field with one hundred percent polarization of all isotopes (^{71}Ga,^{69}Ga and ^{75}As) is approximately 8.3 T [CUZ$^+$17].

Figure 2.6 shows the interaction between the electron and NSS under optical pumping leading to the optical orientation and formation of the Overhauser field. The electron and nuclear spins are coupled via hyperfine interaction (Knight field) and the effective nuclear magnetic field (Overhauser field), and this is shown by red arrows in Fig. 2.6. The excitation with circular polarization light (blue arrow) creates an average electron spin polarization S_0, which could be also detected by optical means (purple arrow). The electron field acts on the nuclei and polarizes them, and the nuclear spins, therefore, act back on the electron via the Overhauser field. This is known in the literature as a nonlinearly coupled electron-nuclear spin system [MZ12, Dya17, HB16].

2.4.2 Nuclear field effects in the longitudinal magnetic field

A nonzero Overhauser field $B_N \neq 0$ acts on the electron spins in the same way as an external magnetic field and should reveal itself in any situation where the electron spins have some non-equilibrium polarization. This effect is related to the influence of the effective magnetic field on the electron spin relaxation rate. It means that there are several reasons how the Overhauser field can reveal itself in the optical orientation experiment. One is the influence of the orientation degree of photoexcited electrons on the electron spin relaxation time.

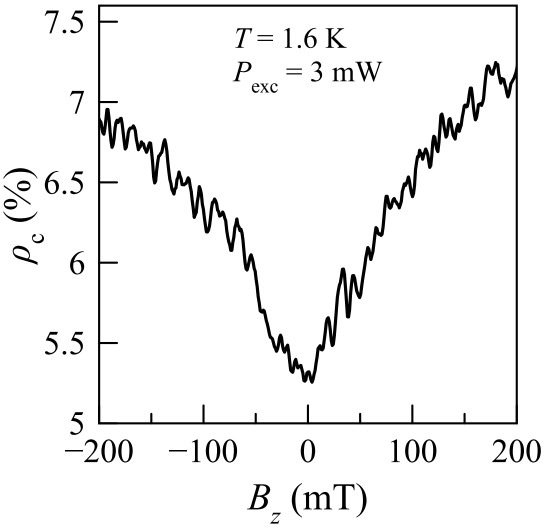

Figure 2.7: Magnetic-field dependence of the circular polarization degree for GaAs at Faraday geometry ($B_x = 0$).

Figure 2.7 shows the experimental results on optical orientation in a longitudinal magnetic field (Faraday geometry). One can see that with the increasing magnetic field, the degree of circular polarization increases, which in turn means that the electron spin relaxation rate decreases due to the suppressive effect of an external magnetic field.

In 1961 Abragam [Abr61] proposed the expression which describes the dependence of electron spin relaxation time τ_s on the magnitude of the longitudinal field:

$$\tau_s(B) = \tau_s(0)(1 + \Omega^2 \tau_c^2), \tag{2.22}$$

where τ_c is a characteristic correlation time of the fluctuating magnetic field determined the electron spin relaxation time $\tau_s \gg \tau_c$. At the presence of the Overhauser field $B_N \neq 0$ the quantity Ω in equation 2.22 defines the total magnetic field acting upon the electron spin: $\Omega = (g\mu_B/\hbar)\,|B + B_N|$.

2.4.3 Manifestation of the nuclear field in the oblique magnetic field geometry

It is known that under conventional geometry of the Hanle effect when the magnetic field B_x is aligned perpendicular to the average electron spin, the nuclear spin polarization is zero [MZ12]. This statement can be violated in the case of small external fields where an essential role is played by the Knight field acting on nuclear spins [Dya17]. In this case, the nuclear spin polarization that arose in the dynamic polarization by oriented electrons is proportional to the scalar product $(\mathbf{B} \cdot \mathbf{S})$.

On the other hand, the situation is different when the angle between the external magnetic field and the exciting polarized light beam differs from 90°. In this case, the Hanle effect is observed in an oblique magnetic field, causing the appearance of the Overhauser field, directed along or opposite to the direction of the external magnetic field and participating in depolarization fo electrons. The nuclear polarization is created by the longitudinal component (concerning the external field) of the electron spin. The formed Overhauser field either decreases or increases (depending on its sign) the transverse component of the electron spin. The typical curve of the luminescence depolarization in an oblique magnetic field, measured in GaAs at continuous-wave excitation, is shown in figure 2.8.

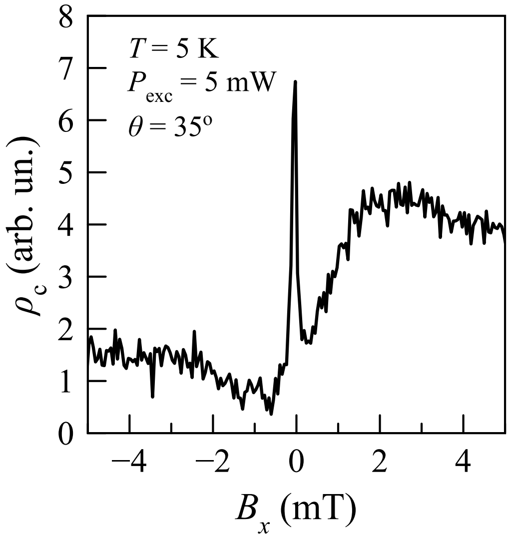

Figure 2.8: Dependence of the circular polarization degree along the direction of the excitation ($\mathbf{k}$) on the external transverse magnetic field (B_x) measured for the bulk p-type GaAs. The angle between B_x and $\mathbf{k}$ is $\theta = 35^{\circ}$.

The steady-state value of the average electron spin component $\langle S_z \rangle \sim \rho_c$ along the direction of excitation S_0 in an oblique magnetic field B can be written as follows

$$S_z(B) = S_z(0) \left(\frac{\sin^2\theta}{1 + (\Omega T_s)^2} + \cos^2\theta \right), \tag{2.23}$$

where θ is the angle between the field and the exciting light beam and $\Omega = (g\mu_B/\hbar)|B + B_N|$.

Figure 2.8 shows that the shape of the Hanle curve turns out to be symmetrical so that the right maximum orientation corresponds to the value of $B_x \approx -B_N$, in which the Overhauser field partly compensates the external magnetic field. The broadening of the Hanle curve, as well as the narrowing of the displaced maximum, are due to inhomogeneity of the Overhauser field [APBS74]. The peak at $B = 0$ can have some additional fine structure due to the influence of the Knight field [MZ12].

Thus, an analysis of luminescence depolarization in an oblique magnetic field allows finding the values of the Overhauser and Knight fields and the sign of the product $g_e g_n$ of electronic and nuclear g-factors. If the distribution of the electron polarization is spatially inhomogeneous, the electron spin diffusion may have a substantial impact on the Hanle effect [Dya17].

2.4.4 Nuclear spin fluctuations

Since the spin orientation of the unpolarized nuclei changes randomly with time which is much longer than the nuclear spin correlation time $\sim 10^{-4}$ s, all unpolarized nuclei do not contribute to the Overhauser effective field. It comes from the fact that at such time scales the total sum of the spin vectors can be averaged to zero. Taking into account that the electron spin lifetime is much smaller than the nuclear spin correlation time, the local fluctuating field B_{NF} of the unpolarized NSS is pointing in one constant direction and interacts with the electron spin. In case when nuclear spins are not completely polarized this fluctuating field can be evaluated as follows [Dya17]

$$\langle B_{\text{NF}}^2 \rangle = \frac{v_0^2 \sum_n A_n^2 |\Psi(\mathbf{r}_n)|^4 I_n(I_n+1)}{\mu_B^2 g_e^2} \approx \frac{B_{N\text{max}}^2}{N}, \tag{2.24}$$

where N is the number of the nuclei interacting with a single electron. Usually N is of the order of 10^5, i.e. the nuclear spin fluctuation field is about 0.3% of the maximum nuclear field. If $B_{N\text{max}}^2 = 8.3$ T (see previous subsection) and $N \approx 10^5$ a rough estimate of $B_{\text{NF}} \approx 26$ mT for GaAs could be found.

2.5 Nuclear spin relaxation

Essentially, the dynamic polarization is a transfer of angular momentum from electrons to nuclei via the hyperfine interaction. This leads to the electron spin relaxation by nuclei and accompanied by such a spin-transfer which conserves the total spin of the interacting particles. The component of the nuclear spin, collinear to the magnetic field is accumulating due to the long longitudinal nuclear spin relaxation time T_1.

On the other hand, it should be added that there are certain necessary conditions for the dynamic polarization: (i) the nuclear spins should be placed in a magnetic field, either an external one or the mean electron field of spin-polarized electrons; (ii) if the dynamic polarization is induced by spin-polarized electrons or holes, the electron mean spin should not be perpendicular to the magnetic field. As a result, the nuclear polarization and the Overhauser field change their direction to the opposite if the sign of the electron mean spin is inverted (for example, if the helicity of the excitation light is changed) [Dya17].

2.5.1 Nuclear spin relaxation due to hyperfine interaction

For conventional semiconductors, the interaction between an electron and nuclear spins is determined by the Fermi contact interaction [Abr61, Dya17]:

$$H_{\mathrm{hf}} = \sum_n a_n (sI_n), \tag{2.25}$$

where $a_n = v_0 A_n |\Psi(r_n)|^2$, v_0 is the unit cell volume, $\Psi(r_n)$ is the electron envelope wave function at the nth nuclear position, I_n is the nuclear spin operator and A_n is the hyperfine constant (for GaAs: $A_n \sim 100$ μeV). The fluctuation of the Knight field leads to the spin relaxation of the nuclei.

Nuclear spin relaxation time due to interaction with the electron is given as

$$\frac{1}{T_{1e}} = \omega_N^2 \tau_c, \tag{2.26}$$

where τ_c is the correlation time and ω_N is the nuclear spin precession frequency in the fluctuating field created by electrons. The equation 2.26 hold for ω_N^2 [MZ12], if the electron is localized in an area with radius r_0:

$$\omega_N^2 \sim \left(\frac{A}{\hbar N}\right)^2 F_e, \tag{2.27}$$

where N is the number of nuclei in the localization area and F_e is the probability for an electron to be in this area. The fraction $\frac{A}{\hbar N}$ in the equation 2.27 is the precession frequency of a nuclear spin in the magnetic field created by a single electron. The equation 2.27 applies only for localized electrons, and for free, non-degenerate electrons it is not applicable [MZ12].

In the presence of an external magnetic field B equation 2.26 changes as follows

$$\frac{1}{T_{1e}} = \frac{\omega_N^2 \tau_c}{1 + \Omega^2 \tau_c^2}. \tag{2.28}$$

The standard estimate made by Bloembergen in 1954 [BW54] and Abragam in 1961 [Abr61] gives $T_{1e} \approx 10^4$ s for GaAs with $n = 10^{15}$ cm^{-3} at $T = 4$ K.

In case of electrons localized at donor site within a radius of $r_0 \sim a_B$ (where a_B is the Bohr radius) the following estimate for nuclei located in the vicinity of the donor center can be used:

$$\frac{1}{T_{1e}} \approx \frac{A_n^2 v_0^2 F \tau_c}{a_B^6 \hbar^2}, \tag{2.29}$$

where $A_n = 6.2415 \times 10^{-5}$ eV for GaAs, $F = n/N_D$ is the filling factor determined by the process of thermal ionization, i.e. hopping to neighbouring sites or recombination.

Numerical estimation of $T_{1e}(r_0)$ at the distance r_0 from the donor center was first made by Lampel (1968) and Dyakonov (1973) [MZ12]:

$$\frac{1}{T_{1e}(r_0)} = \frac{A_n^2 v_0^2 F \tau_c}{2\pi^2 a_B^6 \hbar^2}\, e^{-\frac{4r_0}{a_B}} \approx 0.1\ s, \tag{2.30}$$

with $r_0 \ll a_B$ and $\tau_c = 10^{-10}$ s. In case of constant optical excitation by circularly-polarized light the hyperfine interaction leads to dynamic nuclear spin polarization of the lattice nuclei with the establishment of the thermal equilibrium in the NSS during T_{1e}. A detailed study of this times for n-doped and p-doped GaAs is given in chapters 5 and 6 of this thesis.

2.5.2 Nuclear spin relaxation due to quadrupole interaction

The quadrupole interaction of the nuclear spins with electric field gradient (EFG) in the crystal volume is given by the following Hamiltonian [Abr61]:

$$H_Q = V_{\alpha\beta} I_\alpha I_\beta, \tag{2.31}$$

where $V_{\alpha\beta}$ are the coefficients proportional to the electric field gradient and the quadrupole moments of each nucleus. In piezoelectric crystals like GaAs, electric field gradients at the positions of nuclei can be induced by uniform electric fields [BMMP63].

The distribution of the electric field gradients at the nucleus causes the quadrupole-induced splitting of the nuclear energy levels. These energy levels remain partially degenerate because of the time-inversion symmetry of the Hamiltonian 2.31. This splitting lies in a wide range of possible energies, for example, the quadrupole splitting for As in AlGaAs alloy corresponds to the Larmor frequency of 17 MHz [BS78]. The quadrupole splitting is also observed for samples with self-assembled quantum dots (QDs) due to mechanical stress [HB16], which was much smaller than 17 MHz due to alloy statistics.

The nuclear spin relaxation can also be affected by the fluctuations of the electric field gradients due to photon-induced crystal lattice deformation. At low temperatures due to the low number of phonons, the nuclear spin relaxation can be induced by quadrupole interaction with electric field gradients of resident charge carriers (e.g., under the donor orbit) [PAK08].

2.5.3 Nuclear spin relaxation due to dipole-dipole interaction

The interaction between nuclear spins is the dipole-dipole interaction [Abr61]. The Hamiltonian of the dipole-dipole interaction is written as follows

$$H_{\mathrm{dd}} = \frac{\mu_N^2}{2} \sum_{n \neq m} \frac{g_n g_m}{\mathbf{r}_{nm}^3} \left[(I_n I_m) - 3 \frac{(I_n \mathbf{r}_{nm})(I_m \mathbf{r}_{nm})}{\mathbf{r}_{nm}^2} \right], \tag{2.32}$$

where $\mathbf{r}_{nm}$ is the translation vector between n and m nuclei. For example, for GaAs each nuclei is affected by a local magnetic field $B_L^{\max} \approx 1.5$ G created by other nuclei [MZ12]. The period of Larmor precession corresponding to this field is of the order of several milliseconds.

The magneto-dipole interaction does not conserve the total nuclear angular momentum, which is partially transferred to the crystal lattice. The nuclear polarization relaxation time is about $T_2 \sim 10^{-4}$ s. In case when the external magnetic field is weak comparing to the local field $B \ll B_L$, all nuclear spins relax with T_2 time. In a strong magnetic field, $B \gg B_L$, the time T_2 characterizes the relaxation of a transverse nuclear spin component which is perpendicular to external field B while the longitudinal spin component decays with time $T_1 \gg T_2$ which is responsible for the Zeeman energy reservoir dissipation.

If the nuclear spin polarization in the bulk of the crystal is not isotropic, then the dipole-dipole interaction leads to a spin diffusion flux into the volume with the diffusion coefficient

$$D \approx \frac{d^2}{T_2}, \tag{2.33}$$

where d is the distance between neighboring nuclei. The diffusion coefficient decreases at large gradients of magnetic fields (e.g. external magnetic field or Knight field) [MZ12].

At a distance from the magnetic ion such that the shift of the nuclear Zeeman frequency, due to the local field of the magnetic ion, is negligibly small. Neglecting the effects of angular anisotropy, then D is given by the formula [Khu69]

$$D = l \frac{a^2}{T_2}, \tag{2.34}$$

where a is the distance between the neighboring nuclear spins and T_2 is the time of the transverse nuclear relaxation. The values given for the numerical coefficient of l in most papers are $1/30$ and $1/50$. In particular, for a simple cubic lattice, $l \approx 1/12$ and more detailed calculation of D was performed in [LG67].

2.6 Nuclear spin temperature concept

In a situation when an external magnetic field is weak or comparable to a local magnetic field of spin-spin interactions, the average projection of nuclear spin on the direction of the external magnetic field is no longer a conserved quantity [Dya17]. This results in a complete disappearance of any nuclear spin polarization with T_2. So, it is expected that no optical cooling of nuclear spins in this field is possible, and the demagnetization process is rapid and ends as a complete depolarization of NSS.

On the other hand, a large number of experimental investigations demonstrate that the conditions described in the previous paragraph are not always filled [PLSS77, LMBI06]. This phenomenon can be described with the help of the spin temperature concept [AP58, PP51]. This concept is based on the general theory of nuclear magnetism in solids [Abr61] and means that the evolution of the NSS is dictated by energy conservation law rather than conservation of the total NSS angular momentum. It can be understood as follows, the NSS spin orientation at weak magnetic field changes the total energy of the nuclear spin reservoir while the process of energy dissipation from nuclear spins to the crystal lattice slows down. As a result, a thermal equilibrium for NSS is established, and the single parameter that can be used to describe it is the nuclear spin temperature of Θ_N [Dya17].

The absolute value of Θ_N can strongly differ from the lattice temperature. In this case, the small external magnetic field induces a quasi-equilibrium orientation of the NSS proportional to the paramagnetic susceptibility of the system χ_N. In principle, the value of the Θ_N can be even smaller, down to several μK for the external field of the order of 100 μT.

The master equation describing the energy balance of the NSS interacting with optically-oriented electrons reads as follows

$$\frac{\mathrm{d}}{\mathrm{d}t}\frac{1}{\Theta} = \frac{1}{T_1}\left(\frac{1}{\Theta_0} - \frac{1}{\Theta}\right), \tag{2.35}$$

where Θ is the spin temperature and T_1 is the nuclear spin relaxation time. The expression for steady-state nuclear spin temperature Θ_0 has the following form

$$\frac{1}{\Theta_0} = \frac{4I}{\mu_I}\frac{B}{B^2 + \tilde{B}_L^2}\frac{S_z - S_0}{1 - 4S_zS_0}, \tag{2.36}$$

where $S_0 = -\frac{1}{2}\tanh\left(\frac{\mu_B g B}{2T}\right)$ is the equilibrium value of the electron spin. The temperature Θ_0 can be both positive and negative. If the external magnetic field is low ($B \leq B_L$) the quantity S_0 in Eq. 2.36 may be neglected.

The average nuclear spin (i.e., Overhauser field B_N) is oriented along the magnetic field or opposite to it:

$$B_N = \frac{4}{3}b_N(I+1)\frac{B(\mathbf{B}\cdot\mathbf{S})}{B^2 + \tilde{B}_s^2 L}, \tag{2.37}$$

where b_N is the total Overhauser field created by nuclei of the same isotope at 100% of their polarization. For instance, the nuclei ^{69}Ga, ^{71}Ga and ^{75}As being polarized up to 100% create fields in GaAs [PLSS77, MZ12]: $b_N[^{69}\mathrm{Ga}] = -13.6$ kG, $b_N(^{71}\mathrm{Ga}) = -11.7$ kG and $b_N[^{75}\mathrm{As}] = -27.6$ kG.

On the other hand, from NMR theory the reciprocal spin temperature reads as

$$\beta = \Theta^{-1} = \frac{2}{\mu_I}\frac{(\mathbf{B}\cdot\mathbf{S})}{B^2 + \xi B_L^2}, \tag{2.38}$$

and, as is well known, a solution of the following first order differential equation:

$$\frac{\partial \beta}{\partial t} = -\frac{\beta}{T_1}. \tag{2.39}$$

Equation 2.38 is obtained for nulcear spin $I = \frac{1}{2}$. The basic analysis of equation 2.38 shows that cooling is impossible at $\mathbf{B} \perp \mathbf{S}$, but it was experimentally found that, however, the electron polarization is affected by the Overhauser field. It is clear that this effect can be explained with the nonequilibrium component of nuclear spin polarization, which occurs during the transverse relaxation time T_2. A large number of experiments demonstrate the effect of NSS cooling in the electron field B_e (always collinear with $\mathbf{S}$) generated by optically polarized electrons [MZ12].

The spin temperature can also be introduced for a system of nuclear spins with $I > 1/2$ taking into account the assumption that the Boltzmann law is relevant for any two energy levels of the nuclear spin in the ensemble. This assumption is true only if the equilibrium between different pairs of energy levels is rapidly established by flip-flop transitions. It should be noted that in the presence of the strong quadrupole interaction when interlevel distances are different and flip-flop transitions are suppressed, this assumption is no longer valid. In case when the nuclear spin temperature is already established, the average nuclear spin can be described with the Brillouin function [Dya17]:

$$\langle I \rangle = \frac{\sum_{m=-I}^{m=I} m \cdot \exp(-m\zeta)}{\sum_{m=-I}^{m=I} \exp(-m\zeta)}. \tag{2.40}$$

The Boltzmann distribution over spin sublevels is characterized by the spin temperature Θ_N, which differs from the lattice temperature and can be negative if nuclear spins are polarized opposite to the direction of the external magnetic field [Dya17].

Taking into account the effective Knight field $B_e = b_e S$, equation 2.38 is modified as follows

$$\beta = \frac{4I}{\mu_I} \frac{(\mathbf{S} \cdot \mathbf{B}) + b_e S^2}{(B + b_e S)^2 + \xi B_L^2}, \tag{2.41}$$

where $1 \leq \xi \leq 3$ is a numerical factor dependent on spin-spin interaction. An analysis of equation 2.41 shows that at $\mathbf{S} \perp \mathbf{B}$, NSS cooling is possible only in the Knight field B_e and can be detected through nuclear polarization amplitude.

The inverse nuclear spin temperature of cooled nuclei is highest for $B = \sqrt{\xi} B_L$ and turns to zero at $B = 0$ or at $B \to \infty$ (see Fig. 2.9). Usually, the nuclear spin temperature achieved by dynamic polarization can be considered as a result of a balance between the energy flow into/out of the NSS (taking into account the sign of the temperature) caused by the non-equilibrium spin flow from electrons in the external magnetic field and opposite energy flow due to heating effect of the fluctuating electron field. After optical excitation is switched off, the electron spin polarization reaches equilibrium within a nanosecond time scale, thereby causing an imbalance in the energy flow and thus warming-up the NSS back toward the lattice temperature.

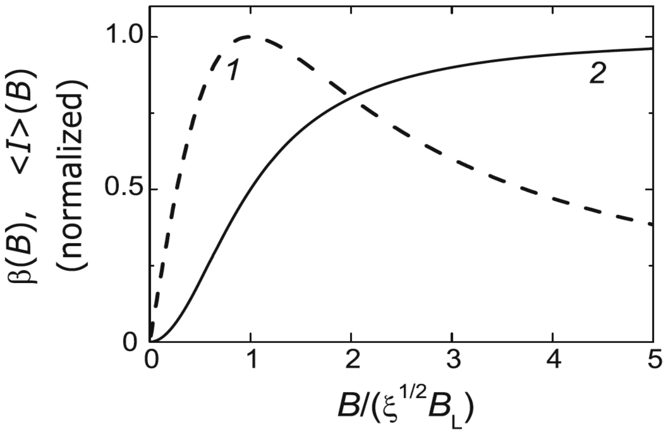

Figure 2.9: Optical cooling of the NSS by oriented electrons [Dya17]. Magnetic field dependencies of the reciprocal spin-temperature (1) and mean spin of the nuclei (2).

It was shown that any fluctuating field (electron, magnetic, or quadrupole) may cause the NSS warm-up [PAK08, KDV⁺16]. For example, in doped GaAs, charge carriers are the primary source of such fluctuating fields at the presence of optical pumping, and nuclear spin relaxation time T_1, in this case, is firmly dependent on doping. This effect is even more pronounced in quantum dots, in particular, after removal of the electron from the singly-charged quantum dot volume affects a significant increase of T_1 from several sub-seconds to hours [LHZ⁺09, MBI07].

Applicability limitations for the spin temperature description

The central tenet of the nuclear spin temperature concept is based on the assumption that the equilibrium in the system of nuclear spins is established much faster than the NSS comes into equilibrium with the crystal lattice. Under ordinary conditions, this statement is true and consists in the fact that $T_2 \ll T_1$. But it should be added that this condition may be violated [MKI09].

For doped semiconductor quantum dots with an odd number of electrons per single quantum dot, the strong hyperfine interaction of an electron with nuclei $\sim 10^5$ can drastically reduce T_1 and make it close in value to T_2 [MBI07, MKI09]. At the same time, the quadrupole interaction can slow down the spin-spin exchange interaction and leads to the splitting of nuclear spin states and the establishment of partial equilibrium inside NSS. Ultimately, this can lead to a violation of the Curie law when changing the sign of the external magnetic field near-zero value.

3 Experimental details

This chapter provides an overview of the main experimental instruments and methods, the function and interplay of the equipment, and configurations of the experimental setup.

3.1 Equipment and setup

3.1.1 Helium-4 cryostats

Bath cryostat

Since this thesis is devoted to the investigation of PL magnetic dependencies at liquid helium temperatures, all samples under study were placed in optical cryostats. The temperature inside cryostat is achieved down to $T = 1.6$ K. The light coming out of the laser gets access to the sample through a fused silica window in the RTI MagnCryo cryostat. The inner diameter of the windows is 20 mm. The bath cryostat RTI MagnCryo with superconducting magnet designed for optical investigations in the magnetic field up to 6 T and different temperatures (1.6 or 4.2 K) was used. The cryostat is a device of open-cycle type designed as a system of coaxial vessels, which includes the outer (cryostat body) and inner (liquid nitrogen and liquid helium tanks) parts. The volume between vessels is exhausted down to 0.13 Pa (10^{-3} mbar). For the regular operation of the cryostat, both tanks are filled with liquid helium and nitrogen. The cryostat itself consists of two vessels. The inner vessel consists of the sample chamber joined with the liquid helium tank, liquid nitrogen tank, and the copper shield. The outer vessel is a cylindrical tank with an opening in the center through which the inner vessel coaxially passes through. The liquid helium tank is attached to the cryostat body via three stainless steel tubes used for the tank filling, as well as for the liquid helium level tests. The liquid nitrogen-cooled copper shield protects the outer surface of the helium tank and the sample chamber. The copper shield is attached directly to the liquid nitrogen tank. Excellent heat transmittance of the copper shield keeps it cold and prevents the heating of the liquid helium tank and sample chamber by the heat flow from the environment. The liquid nitrogen tank is attached to the other vessel via two thin stainless steel tubes that are used for the filling of the tank. The inner vessel tail is equipped with four optical UV-quartz windows. The similar optical windows are located on the copper shield and the outer vessel (cryostat body). The optical windows have an angular separation of 90 degrees. On top of the cryostat, there is a sensor of the liquid helium-meter. The sample holder with a superconducting magnet is placed directly into the inner sample chamber of the cryostat.

Flow cryostat

The standard boiling point of liquid 4He, it is rather uneconomical to use the main 4He bath at 4.2 K as a temperature reservoir and then to regulate the experiment at higher temperatures. It is much more efficient to use the cold gas evaporating from liquid helium and take advantage of its enthalpy for cooling the experiment in a continuous gas-flow cryostat. This allows the storage vessel containing the liquid helium to be separated from the cryostat with the experiment.

For the measurements described in chapters 5, 6 and 7 with compensation of laboratory fields and at small applied magnetic fields, the Oxford cryostat (Microstat He-R) has been used. Figure 3.1 shows the schematic of the cryostat and its main components. Continuous flow cryostat has no internal reservoir to store a supply of cryogen. The liquid helium is supplied from a separate storage vessel through an insulated transfer tube. The transfer tube delivers the liquid helium to a heat exchanger close to the sample space. The gas returning from the heat exchanger then cools the radiation shield and cold finger then it flows out of the cryostat. A thermometer and a heater are mounted on the heat exchanger and can be used with a temperature controller to balance the cooling power of the cryogen and to control the temperature of the sample [Nan13].

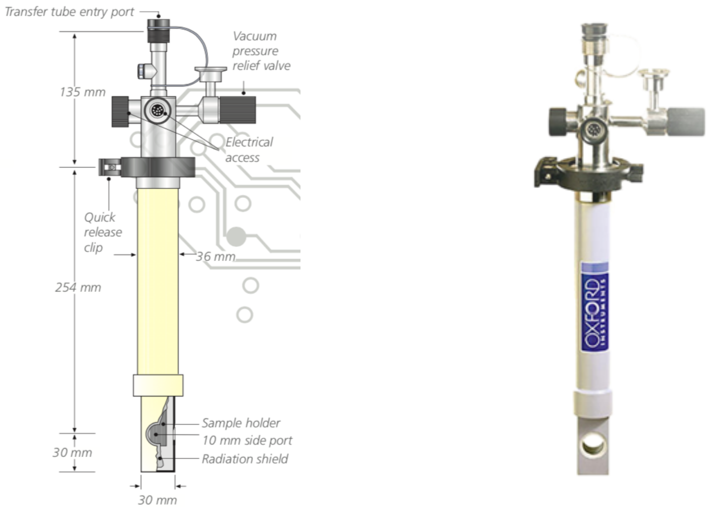

Figure 3.1: Diagram of the MicrostatHe2 with the rectangular tail.

It is possible to maintain a temperature below 4.2 K continuously using the standard gas flow pump (GF4) and the controller (VC-U). Lower temperatures can be achieved using a larger pump, such as the EPS40 rotary pump. The system can also be run using a transfer tube, in which case the pump is attached to a port provided for this purpose on the cryostat.

The sample is mounted in the vacuum on a heat exchanger, and the optical access to the sample is available through the optical windows. The sample space and radiation shields are thermally insulated from the room temperature surroundings by the outer vacuum chamber. This space is pumped to a high vacuum before the cryostat is cooled down but protected against an accidental build-up of high pressure by a pressure relief valve. The rate and, therefore, the cooling power and temperature can be controlled via the setting of a needle valve. The system can easily be automated by applying a solenoid valve in the pumping line, which is controlled by a thermometer on the experiment and an appropriate bridge controller electronics. The advantages of such a design are low consumption of the cryogenic liquid, the temperature variable in a rather wide range up to room temperature, and the apparatus that can be cooled down and warmed up in a short time [Pob07].

3.1.2 Electrooptics

This thesis contains experimental results that are devoted to a study of the time-resolved effects in the NSS. The primary tool in the conducted studies is the polarization/intensity modulation technique. The modulation is widely used in modern experiments to improve the signal-noise ratio. In optical pumping experiments, the polarization and intensity modulation of the exciting light is crucial. Since all processes determining the polarization of the electron-nuclear spin system have some characteristic frequencies within a wide range of values, from a few Hz to some dozens of kHz. What is very important is that under constant light polarization excitation, all these processes are indistinguishable.

Below there is a brief description of electro-optics that made it possible to use modulation techniques to studying of the NSS dynamics in a wide frequency range.

Acousto-optic modulator

The acousto-optic modulator (AOM), which was used in this work consists of the acousto-optic modulator element and the driver electronics. The modulator element contains an optical crystal with a piezo transducer at one side. By applying an RF carrier signal to the piezo transducer, the ultrasonic waves are induced into the crystal. This causes modulation of density and refractive index inside the crystal, which acts as an optical grating for an incident laser beam. A part of the beam is deflected. The deflected part of the beam is frequency shifted by the amount of the applied RF frequency 80 MHz.

To achieve an efficient deflection a resonance condition between the deflecting angle Θ, the acoustic velocity in the crystal v, the RF frequency f_{mod}, and the wavelength of light λ must meet the condition:

$$\Theta = \frac{\lambda f_{\mathrm{mod}}}{v}. \tag{3.1}$$

By changing the field intensity (RF power) the intensity of the deflected beam can be varied. The RF power is controlled by an external TTL generator.

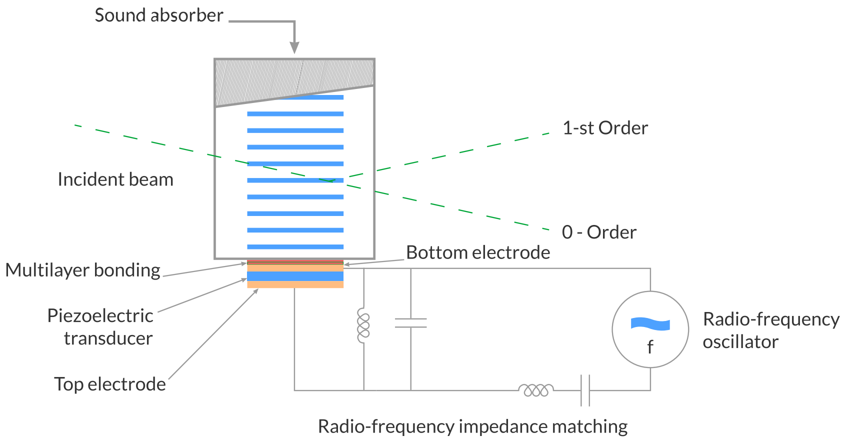

Figure 3.2: Acousto-optic modulation principle [A19].

The maximum modulation speed is limited by the travel time of the ultrasonic wave through the beam (with diameter D_B):

$$t = \frac{D_B}{v}. \tag{3.2}$$

So the beam must be focused on the modulator to achieve fast modulations. On the other hand, the deflection efficiency decreases with decreasing beam diameter, because only a smaller part of the acoustic field interacts with the beam [APE05].

The acousto-optic modulator in the mode of slow intensity modulation (with AOM extinction ratio $< 1000 : 1$ and optical transmission $> 95\%$) in the time range from 10 to 1500 milliseconds was used in chapters 5 and 6 to measure slow NSS relaxation dynamics and NSS relaxation times "in the dark".

Electro-optic modulator

Electro-optic crystals change their optical path length by application of an electric field. This change is polarization sensitive. The difference in path length of orthogonally polarized beams corresponds to one half of the wavelength if the half-wave voltage is applied. In this case, if the crystal is oriented suitably, the polarization direction of the transmitted light rotates by 90°. A variation of the applied voltage allows a quick modulation of the intensity of the transmitted laser beam. Therefore the operation principle of an electro-optic modulator (EOM) can be understood as a retardation plate with an electrically adjustable retardation [QIO19].

The LINOS 0202 EOM provided the modulation of the helicity of the laser light for the experiments in this work. The LINOS 0202 works in a regime of switching half-wave plate, rotating the polarization plane of the linearly polarized light to 90° depending on the voltage applied to its crystal using the digital-input and fully analog high voltage amplifiers LINOS DIV-20 and LINOS LAV-400.

Both voltage amplifiers are controlled by the arbitrary waveform generator (Tabor Electronics 5064). When the voltage adjusted at the "high" state for the amplifier and applied to the EOM, it leads to a rotation of the polarization plane of 90°, while the "offset" voltage corresponds to "low" state and the polarization plane is not changed. Thus, the EOM switches the pump polarization between two perpendicular linear polarization. In combination with the quarter-wave polarization plate, this can be used for the switching between a left-circular (σ^-) and a right-circular (σ^+) polarization of the pumping light.

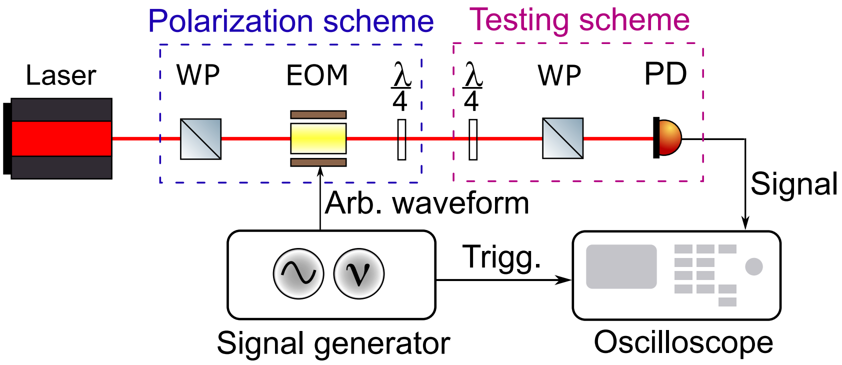

Figure 3.3: Testing schematic of the polarization achieved with the EOM. The red lines denote the laser beam. The optical elements from testing part of the scheme (shown with purple dashed box) are removable in the path of the laser beam on the way to the cryostat. (Optical elements taken from the graphics library [Fra09].)

For the adjustment and operation of the EOM, it is required a linearly polarized laser light. When the intensity of laser radiation is needed to be modulated, an additional polarizer has to be used. The LINOS LM0202P model has an integrated polarizer: Wollaston Prism (WP). The side of the modulator with the analyzer has to be put downstream. The analyzer can be identified easily due to the extra plate used as a polarizer mount. In case of operating an electro-optic modulator between crossed polarizers yields an intensity variation as given by:

$$I = I_0 \sin^2\left(\frac{\pi}{2}\frac{|U - U_{\text{offset}}|}{U_{\lambda/2}}\right), \tag{3.3}$$

where $U_{\lambda/2}$ is the half-wave voltage, I_0 is the input intensity, and U is the signal voltage. Figure 3.3 illustrates the polarization verification scheme (for measuring the achieved degree of circular polarization) for a helicity modulation of the laser beam using LINOS LM 0202 laser modulator. A fast photodiode (Thorlabs DET10A/M) with a load of 50 Ω (in order to achieve the fast rise time of the diode of about one ns) is connected to an oscilloscope to determine the degree of circular polarization for TTL and other arbitrary signals.

Photoelastic modulator

To analyze the PL polarization from the sample, a photo-elastic modulator (Hinds instruments PEM 100) in the registration system was used. A detailed description of the PL polarization registration system in the general scheme of the experimental setup will be provided in section 3.2.1 of this work.

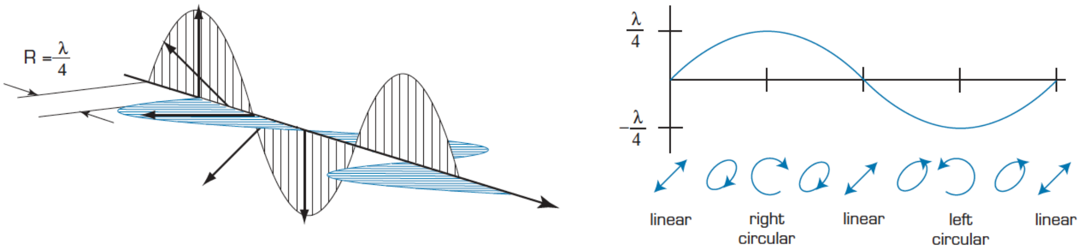

Figure 3.4: PEM quarter-wave retardation scheme [Ins19].

The photo-elastic modulator (PEM) is an instrument used for modulating or varying (at a fixed frequency) the polarization of a light beam. The PEM-100 principle of operation is based on the photo-elastic effect, in which a mechanically stressed sample exhibits birefringence proportional to the resulting strain. The PEM-100 is a resonant device producing oscillating birefringence at 50 kHz. In its simplest form, the PEM head consists of a rectangular bar of a suitable transparent material (fused silica) attached to a piezoelectric transducer. The bar vibrates along its long dimension at a frequency determined by the length of the bar and the speed of a longitudinal sound wave in the optical element material. The transducer is tuned to the same frequency and is driven by an electronic circuit that controls the amplitude of vibration. The oscillating birefringence effect is at its maximum at the center of the fused silica bar.

The PEM-100 in the regime of quarter-wave retardation was used to analyze the state of a polarized PL. Figure 3.4 shows the full retardation cycle versus time and the polarization states at corresponding moments in time. The polarization oscillates between right circular and left circular states, with linear and elliptical polarization states in between. In the registration system, a net circular polarization component will produce an electrical signal in the detector at the modulator frequency f. A net linear polarization component at 45° concerning the modulator axis will produce an electrical signal in the detector at twice the modulator frequency $2f$. The transfer of the reference signals at f from the PEM-100 controller with the Stanford Research two-channel gated photon counter (SR 400) allowing the simultaneous measurement of two circular-polarization components and real-time calculating of the PL circular polarization degree.

3.2 Experimental techniques and configurations

This section provides a detailed description of the experimental setup, the features of the experimental devices and instruments, and a description of all experimental configurations used in this work for obtaining various types of experimental data.

3.2.1 Photoluminescence spectroscopy experimental setup

Photoluminescence spectroscopy is a widely used technique for the characterization of the optical and electronic properties of semiconductors. The relaxation processes can be studied using the time-resolved fluorescence spectroscopy to find the decay time of the photoluminescence. These techniques can be combined with microscopy to map the intensity or the lifetime of the photoluminescence across a sample (e.g., a semiconducting wafer, or a biological sample that has been marked with fluorescent molecules) [Wik19]. The observation of photoluminescence at certain energy can be viewed as an indication that an electron populated a donor state associated with this transition energy. In this work, the time-dependent polarization state of PL spectra provides valuable information about the dynamics of the NSS. In this connection, a typical PL setup was extended and improved, as described below.

An illustration of the experimental setup on optical spin orientation and its detection using polarized luminescence is shown in figure 3.5. The superconducting magnet inside the RTI MagnCryo bath cryostat gives a homogeneous magnetic field perpendicular to the plane of the optical table (xy-plane). For the bath cryostat, the useful volume for the sample ≈ 2 cm^2, while for the flow cryostat ≈ 3 cm^2. The optical axis is parallel to the plane of the optical table. The sample is mounted on the height of the optical axis, and the surface of the sample is oriented orthogonally to it. The laser is operated at photon energies higher than the bandgap of the material of the studied sample. For the continuous wave (CW) laser excitation, a pump solid-state Nd:YAG and a Ti:Sapphire lasers where used. The Ti:Sapphire laser can be tuned in a range of 750–850 nm. The laser beam can be adjusted in intensity using the AOM. The working body (crystal) of the AOM is transparent for the laser light and is periodically deformed with a carrier frequency of 80 MHz (for details, see section 3.1.2). A radio-frequency generator drives the AOM, and the low-frequency modulation of the envelope function for this modulation is controlled by the arbitrary waveform generator (Tabor Electronics 5064). The ramp-up or ramp-down time to reach the highest (lowest) intensity of the outcoming beam is about ten nanoseconds. For appropriate optical adjustment of the AOM, the first-order diffracted beam is split off by a diaphragm. The angle between the incoming light and the AOMs crystal surface is about 10–15°.

The gradient filter and $\lambda/2$ help to further reduce and control the intensity of light when it hits the WP and then passes into the electro-optic modulator. The EOM can rotate the polarization plane by 90° so that horizontally polarized light becomes vertically polarized. The polarization change from horizontal to vertical takes less than fifty nanoseconds (using the digital EOM amplifier). The digital pulse amplifier can apply voltage to the crystals of the EOM with a maximum frequency of 20 MHz, and the analog amplifier can apply voltage with the maximum frequency of 2 MHz. In combination with the $\lambda/4$ wave plate one can excite the sample with right and left-circular polarizations. The EOM can handle light in a range of 650–1000 nm with the maximum laser power of 5 W. A function generator (Tabor Electronics 5064) can control both EOM and AOM synchronously.

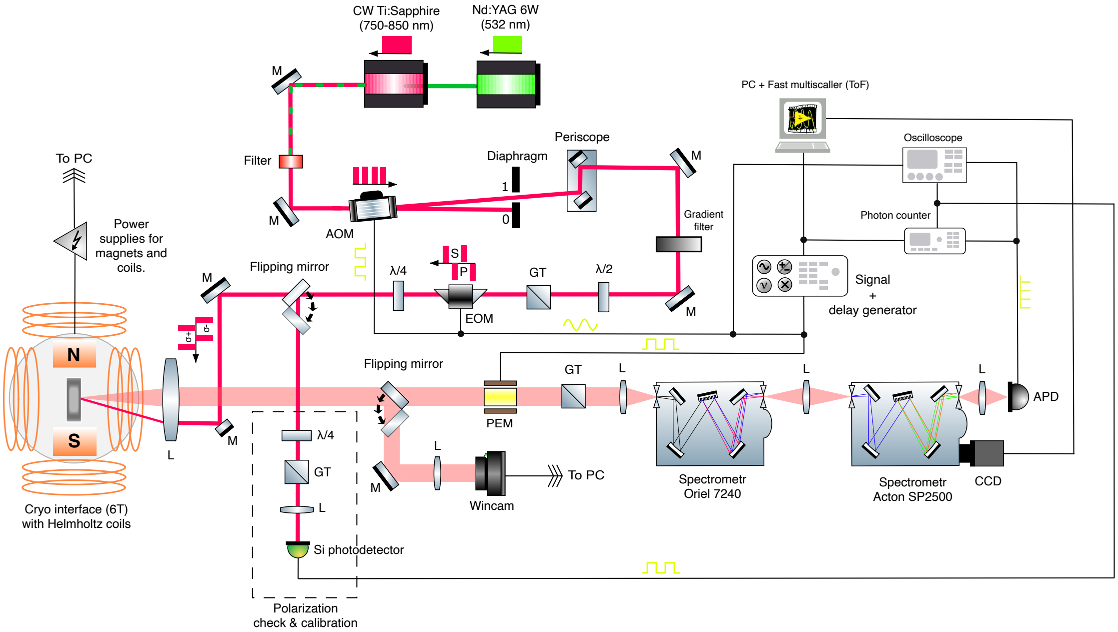

Figure 3.5: The scheme of the experimental setup. The CW tunable laser provided the optical excitation of the studied samples. A system of lenses and mirrors for collecting the resulting PL and coupled it into an spectrometer and avalanche photodiode (APD) was used.

After passing a $\lambda/4$ plate, the polarization state is periodically modulated from left circular to right circular light (σ^+/σ^-). In between, the polarization changes from elliptical to linear. After this step, the polarized laser light is focused on the sample with a $f = 200$ mm achromatic doublet into the spot, which is typical $60 - 100$ μm in diameter. With the help of a video camera, which shows the position of the laser spot on the sample, the control of the beam position relative to the sample geometry can be implemented. The sample is mounted in an optical cryostat that allows the bipolar application of a magnetic field up to 6 T using a superconducting magnet or up to 0.6 T for the Oxford flow cryostat using an external resistive magnet with the additional external 3D Helmholz coils (see figure 3.5). The position of the magnet relative to the sample inside of the RTI MagnCryo cryostat can be changed by replacing an insert with a sample holder and the superconducting magnet. It means that both magnetic filled configurations (Faraday $\mathbf{k} \parallel \mathbf{B}$ and Voigt $\mathbf{k} \perp \mathbf{B}$) are accessible.

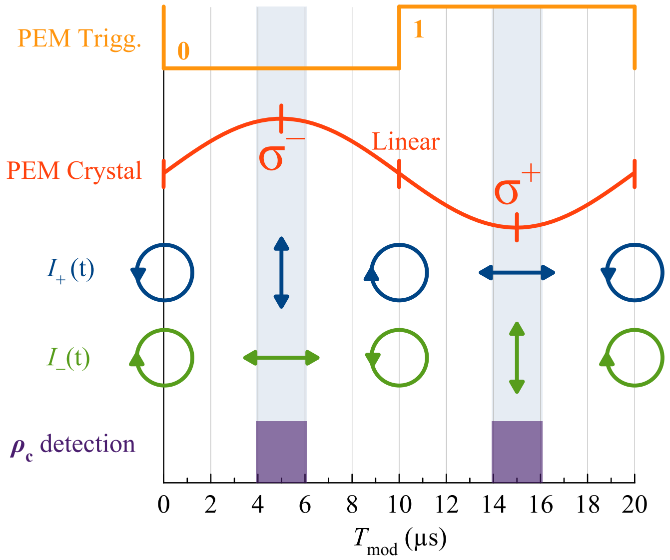

Figure 3.6: $I_+(t)$ and $I_-(t)$ illustrates the development of the polarization detection due to the modulation period of the PEM. At the moment $t = 0$ the polarization for $I_+(t) \sim \sigma^-$ and for $I_-(t) \sim \sigma^+$. The red sine curve indicates the phase of the PEM. The horizontal and vertical arrows indicate the polarization change due to the corresponding position of the phase. The positions of the detector gates with $T_{\text{mod}} = 2 \ldots 5$ μs relative to the PEM modulation are shown at the bottom of the figure with purple rectangles.

The analyzed PL signal from the sample is collimated with achromatic doublet ($f =$ 200 mm) and passed through the PEM and, therefore, the only vertically polarized light component can pass the GW prism while PEM oscillates at 50 kHz. During each period, the piezo crystal induces strain to the fused silica plate crystal of the PEM. When the crystal is compressed, it operates as a $+\lambda/4$ wave plate (with a delay of 5 μs after the trigger signal). When the crystal is stretched, it operates as a $-\lambda/4$ plate (15 μs after the trigger signal). Starting from 5 μs, the polarized PL is converted to vertically/horizontally polarized light after passing GW prism. Figure 3.6 shows the full cycle of the PEM modulation period and PL detection times. Such a combination of PEM and GW prism allows separating the circularly polarized light of the PL.

For the spectral resolution of the PL, two spectrometers were used: half-meter spectrometer (Princeton Instruments Acton 2500i) and 0.125 m hand-operated monochromator (Oriel 7240). The Oriel 7240 uses a hand crank to position the grating, and the Ebert-Fastie design [JH80] features two slits in line with each other, with an out of plane grating. There is a possibility to use only the half-meter spectrometer or both together in a “double-pass” monochromator mode (for reducing scattered laser light in the PL signal). The spectrometer Acton 2500i is an imaging monochromator with three different diffraction gratings (300 gr/mm, 600 gr/mm and 1200 gr/mm) where the light from the entrance slit falls upon the first of two aspherical mirrors so that a collimated beam is reflected onto the diffraction grating mounted on a motorized turret. The grating diffracts the light from the first mirror onto the second aspherical mirror, which collimates and reflects it onto the CCD chip. The silicon CCD Princeton Instruments Spec-10:400R from Roper Scientific is used for acquisition of the PL spectra, control of the pump laser energy, and for setting the APD detection energy respect to the PL spectral dependence of the sample. The 1340 × 400 imaging array has an 8-mm chip height and 27-mm spectral coverage for single and multi-stripe applications. Liquid nitrogen cooling of the CCD chip eliminates dark noise for long exposure times.

For all measurements in this thesis, a grating with 600 g/mm is used. The software "WinSpec/32" is employed to analyze the PL spectrum collected by the CCD. Since the grating spectrally spreads the PL in a horizontal plane, then only the horizontal resolution of the Si-CCD is essential, and the signal of the vertical pixels was integrated. This gives a sufficient CCD resolution equal to 1x1340 pixels. Using the software "WinSpec/32", it is also possible to determine a central wavelength and to direct only the intensity of the central wavelength to APD (SPCM-AQR-14, Perkin Elmer) with a counting rate of 10^6 photons/second.

3.2.2 Measurement of the Hanle effect and the polarization recovery curve

The fundamental method of the spin lifetimes and nuclear field measurement is the CW Hanle configuration of the experimental setup shown in figure 3.5. The standard data acquisition setup for Hanle measurement with or without excitation polarization modulation is shown in figure 3.7. The generator (Tabor Electronics 5064) with first channel A is used to send the modulation to the EOM. At the same time, a TTL signal from the PEM controller is used to trigger the generator. The maximum amplitude on the output of the generator is 10 V peak to peak. The Stanford Research two-channel gated photon counter is calculating many photons during trigger signals coming from the PEM controller, as well as generating a trigger signal (equal to dwell time) for APD in order to reduce the number of "spurious photons" responsible for dark counts outside the counting (dwell) time. The two-channel gated photon counter (SR400) has two independent discriminators, two internal gate generators, and two counters. The photon-counting scheme uses one of the discriminators, but the signal from the discriminator is equally divided into two channels. However, the gates in the two channels are set with different time delays and synchronized with the PEM modulation. Thus, a two-channel count of photons is performed, from where the degree of circular polarization can be calculated. The CCD camera and both power supplies (for superconducting magnet and external 3D Helmholz coils) are controlled with PC using the LabVIEW software via the GPIB-bus interface. Depending on the polarization measurement protocol, a set of different build-in computer programs can be used to operate with the generator (Tabor Electronics 5064).

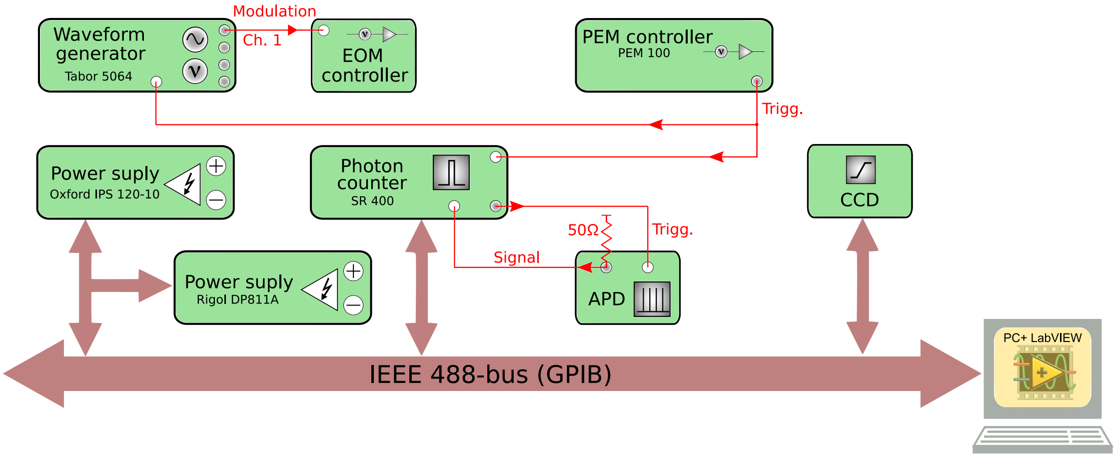

Figure 3.7: Schematic of the data acquisition instrumentation used to obtain Hanle curves. The red lines denote connections made with BNC cables. (See the text for additional details.)

The photon counter can operate in two different modes: (i) collecting the signal from APD upon arrival of the PEM trigger pulse or (ii) counting photons for a given time after the trigger from a generator (Tabor Electronics 5064). The number of the counted photons is weighted, depending on the phase of the PEM (see Fig. 3.6). A developed LabVIEW program uses the absolute values of counted photons I_+ and I_- for σ^+ and σ^- detections phases for calculating circular polarization degree:

$$\rho_c = \frac{I_+ - I_-}{I_+ + I_-}. \tag{3.4}$$

The generator receives information about the phase and modulation frequency of PEM. Therefore, the signal of the function generator is synchronized with the PEM in frequency domain and phase. The accurate gating of the I_+ and I_- intensities is provided by precise time protocols and using digital delay electronics synchronized to the gating the polarization detection scheme such that ρ_c is accumulated when the system is illuminated with light reaching a circular polarization degree above 80% during a single half-period of PEM modulation. In some experiments, to eliminate a possible impact of the nuclear spin polarization, the helicity of the pumping light (between σ^+ and σ^-) is modulated with a waveform generator (Tabor Electronics 5064) at a frequency f_{mod} exceeding several tens of kHz.

It should also be taken into account that the SR400 has a lower pulse count rate than the pulse generation frequency of the photon counter. Therefore, for the correct operation of electronics, the frequency of TTL pulses should not exceed 3×10^5 counts per second. Taking into account the load factor, the channel gates should accumulate approximately 10^5 samples per second. At this count rate, the error of measuring the degree of polarization is $\Delta N/N \approx 0.001 - 0.002$.

The bath RTI MagnCryo cryostat (or flow Oxford cryostat) is oriented in a Voigt (Faraday) geometry and connected to a power supply Oxford IPS 120-10 (or Kepco Bop 100-10MG for external resistive magnet) with a maximum current of 80 A (8 A for the resistive magnet). Taking into account the conversion factors of 15.1 A/T for superconducting and 13.3 A/T for resistive magnets, the following maximum, and safe magnetic fields can be achieved: 6 T for superconducting magnet and 0.6 T for the resistive magnet.

The polarization recovery curve (PRC) can also be measured using the configuration of the experimental setup shown in figure 3.7. The main change in setup for measuring the PRC curves will be only the replacement of the superconducting magnet insert (with Faraday configuration). At the same time, the external Helmholtz coils (see Fig. 3.5) which were used to create an additional longitudinal magnetic field B_z in the experiments for measuring the Hanle curves (Voigt configuration), can be used to create the additional transverse magnetic field B_x (for Faraday configuration). The strength of the longitudinal magnetic field B_z varies between 0 and 3 T. The illumination of the sample is always realized from the same side and window of the cryostat. In both configurations, the lens with $f = 200$ mm focuses the laser beam onto the sample, which is placed inside the strain-free black paper envelope and installed at a holder made of a low temperature-resistant plastic. The helicity of the excitation is modulated in the same way as for the Hanle measurements. The pump modulation frequency was varied from a few tens of hertz to hundreds of kilohertz, measurements of this type are used as a primary tool for the spin inertia measurements in chapter 4 of this thesis.

3.2.3 Measurement of the time-resolved Hanle effect

The experimental setup shown in figure 3.5 has been extended in order to realize various temporal excitation-detection protocols. In this particular case, the circular polarization of the excitation could be modulated between σ^+ and σ^- with frequency f_{mod} from sub-Hertz up to 50 kHz with synchronized detection of the ρ_c during various time intervals. The PL counting is performed in a time window ranging from 20 μs to 500 ms delayed from the excitation trigger by different time delays Δt. The analysis of the PL circular polarization degree is done by using PEM followed by a large-aperture WP. The intensities of the σ^+ and σ^- PL polarization components are obtained by gating the pulses generated by the signal generator synchronously with the PEM modulation. The degree of circular polarization ρ_c with an accuracy of about 0.1% determined by the photon counts accumulated during a single measurement. The excitation modulation, the PL gating time window, and the photon counting gates are synchronized by a precise digital delay generator (Quantum Composer 9520). Thereby, various problems could be addressed, particularly the time-dependent measurement of ρ_c and time-resolved Hanle effect with a polarization modulation is performed.

Figure 3.8 shows the general scheme with devices that were used for the time-resolved

Hanle measurements. The digital delay generator synchronously controls EOM modulation and photon counter accumulating via internal clock generator synchronized to the PEM trigger signal. The digital delay generator controls the modulation frequency and position of the photon counter detection time windows. All signals are transferred to the oscilloscope BNC inputs for additional verification of the modulation-detection protocol.

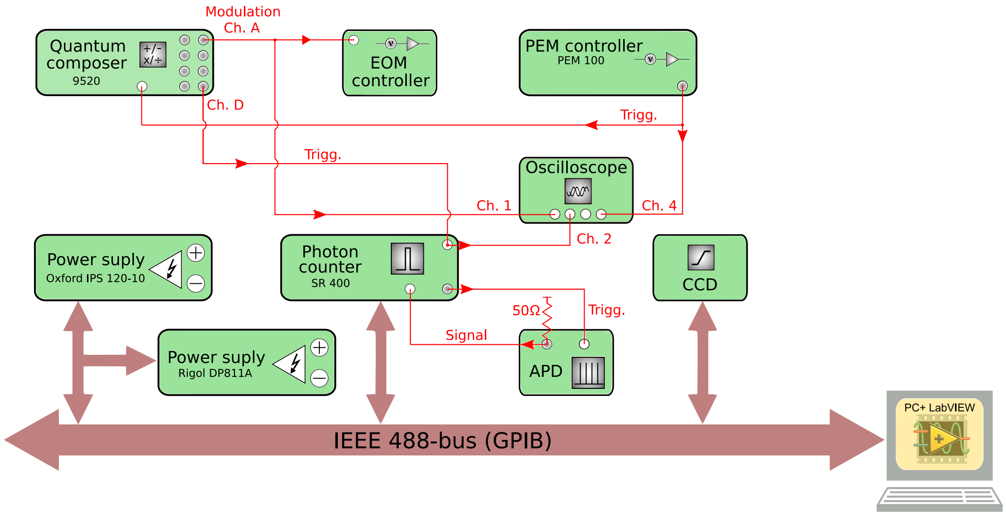

Figure 3.8: Schematic of the data acquisition instrumentation used to obtain time-resolved Hanle curves.

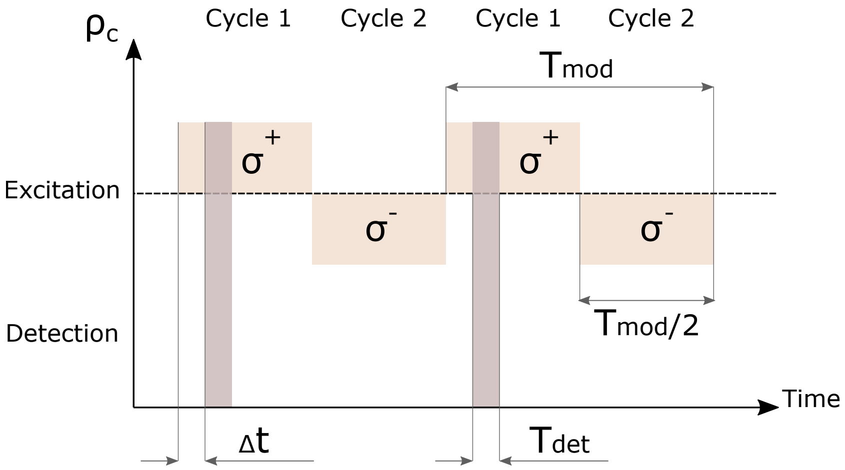

Figure 3.9: Excitation-detection scheme. Start of detection Δt after beginning of cycle 1 or 2 can be varied as well as duration of read out gate T_{det}.

Figure 3.9 illustrates separate detection of the ρ_c with adjustable time resolution inside each half-period of polarization modulation protocol. The square function TTL signals have a sharp rise equal to several nanoseconds with duration controlled with the EOM generator and digital delay generator (Quantum Composer). Therefore, two modulation half-periods (Cycle 1 and Cycle 2) with opposite pumping light helicity are generated, and ρ_c is accumulated during variable time T_{det} in one of the half-periods of excitation modulation (see Fig. 3.9). Time delay Δt before the start of the ρ_c accumulation could also be controlled. By measuring the circular polarization ρ_c depending on Δt with fixed T_{mod} provides the ρ_c time dependence inside the entire modulation period T_{mod}. By choosing a wider detection gate T_{det}, the accumulating time for each measurement decreases. The photon counter operation mode remains the same as for the Hanle curve acquisition at constant excitation polarization (see section 3.2.2), since T_{mod}, T_{det} and Δt are automatically controlled with delay electronics.

3.2.4 Time-of-flight measurements of the nuclear spin relaxation dynamics

For studies of transient nuclear spin polarization, the experimental setup shown in figure 3.10 was used. To access millisecond timescale, therefore, pump pulses cut out of the CW laser beam with an AOM, controlled by the waveform generator (Tabor Electronics 5064). The PL polarization is measured in the reflection geometry at the spectral maximum of the PL polarization. The emitted light passes through the spectrometer and is detected by the avalanche photodiode (APD), followed by the multichannel photon-counting system (PCS). The latter is synchronized with the AOM via the same waveform generator.

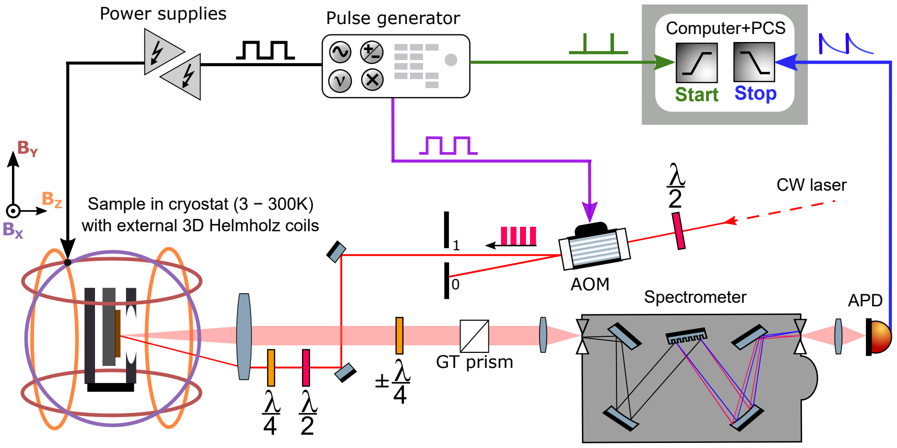

Figure 3.10: Experimental setup designed for time-of-flight (ToF) measurements of sub-second nuclear spin relaxation times "in the dark".

The multichannel photon-counting system utilizes a multiple-event time digitizer: Fast ComTecModel P7886. It was used in the ultra-fast Multiscaler regime with a maximum pulse-width evaluation and the 100 ps precision. The P7886 is capable of accepting one event (stop pulse) in every time bin. Burst/peak count rates of up to 2 GHz can be handled with no deadtime between time bins. For experiments presented in this thesis requiring repetitive sweeps, the spectral data obtained from each sweep was summed, enabling extremely high sweep repetition rates. For measurement of multiple STOP events (photons) in a time range from one μs to several hundreds of milliseconds after START (trigger) pulse, each measurement runs exactly 100 sweeps for every time counting period until it ends.

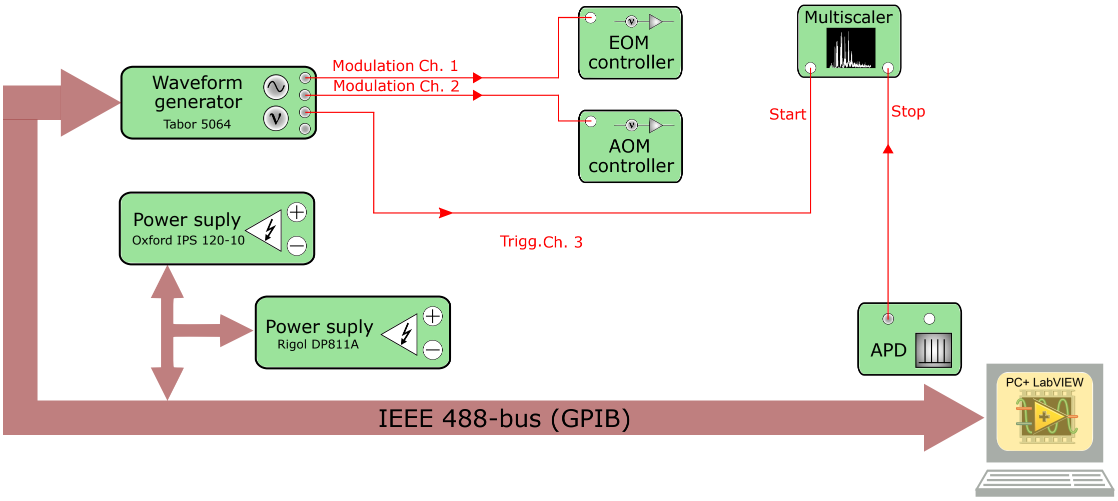

Figure 3.11: Schematic of the data acquisition instrumentation used to obtain the ToF dynamics of the ρ_c.

The waveform generator (Tabor Electronics 5064) is configured to drive two 50 Ω inputs to 1 Volt and not exceeding 2.5 Volts (the absolute maximum ratings of the discriminator inputs). The fourth modulation channel is connected with the START input of multiscaler, while STOP input receives APD photon counts during the SWEEP time of the multiscaler. Any signal on to the discriminator inputs the maximum differential voltage of ±3.0 V between the discriminator and the corresponding threshold voltage should not be exceeded.

The example of basic measurement setup and timing diagram for nuclear spin dynamics measurements “in the dark” presented in the chapter 5 are shown in figure 3.12. For measurement of the arrival time of multiple STOP events (APD counts) [see figure

3.12(b)] in the desired time range after a START (trigger) pulse the P7886 software includes the MCDWIN program which can be installed on Win-PC. Figure 3.12(c) shows the MCDWIN settings window where four main parameters should be configured: Sweep preset, Binwidth, Range, and Inputs. In order to achieve a reasonable signal-to-noise ratio during the measurement of the PL circular polarization degree ρ_c in the time window equal to 1000 ms, the acquisition should run for 100–200 sweeps until it can be stopped automatically after a specified number of sweeps by checking Sweep preset box. In the edit field Range, the length of the spectrum can be entered. A bin width of 2 ns means the highest time resolution. The Binwidth can be chosen from 2 ns up to 16777216 ns. The Inputs button opens the Input Thresholds dialog box, which specifies one of the inputs (NIM or ±2V) for the START and STOP input and the threshold level at the falling edge of the input signal. Voltage level set by hand between -0.8 and -0.25 V. In principle, it is possible to gate the NIM input by the corresponding ±2V input, for this case the checkboxes of both inputs should be marked.

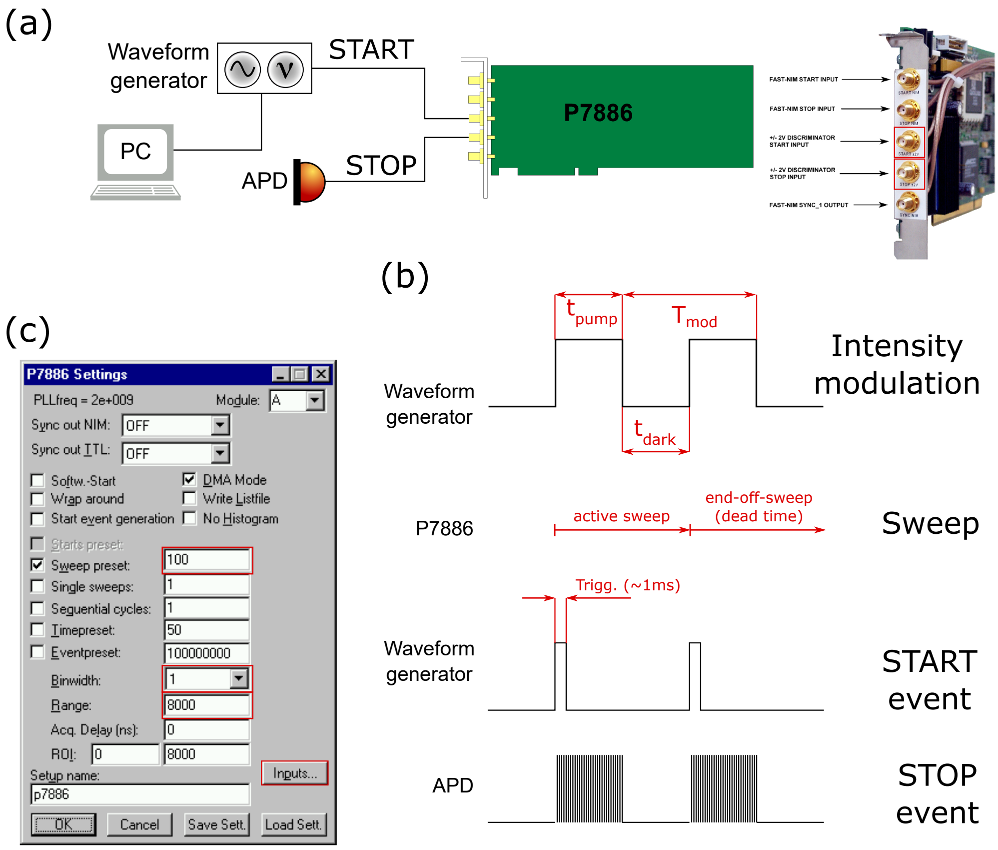

PLLfreq = 2e+009 Module: A
Sync out NIM: OFF
Sync out TTL: OFF
☐ Softw.-Start ☑ DMA Mode
☐ Wrap around ☐ Write Listfile
☐ Start event generation ☐ No Histogram
☐ Starts preset:
☑ Sweep preset: 100
☐ Single sweeps: 1
☐ Sequential cycles: 1
☐ Timepreset: 50
☐ Eventpreset: 100000000
Binwidth: 1
Range: 8000
Acq. Delay (ns): 0
ROI: 0 8000
Setup name: p7886

Figure 3.12: Procedure for ToF measurement. (a) Basic measurement setup. (b) Measurement timing diagram. (c) P7886 settings window.

Thus, without a signal applied, the FAST-NIM inputs will not influence the measurement after the hardware is initialized correctly in order to start the single measurement (Start button). When the selected measurement time range has elapsed the sweep, and so the data acquisition ends. The resulting spectrum of I_+ or I_- is suggested to look like the distribution of the photons with a certain polarization [see figure 3.13(b)]. At the end of the measurement, the program writes two files with the result of measuring (time-resolved number of counted photons) and a service file with data acquisition preferences.

Polarization calibration

In order to measure any time dependence of the ρ_c, the fast multiscaler can be used as a tool for experimental calibration of the exciting light polarization state. The circular polarization of the excitation could be modulated using the EOM (see section 3.1.2) in combination with a $\lambda/4$ wave plate. A waveform generator (Tabor Electronics 5064) was used to trigger the EOM. The square function pulse trains had a sharp rise of a few nanoseconds. Their duration $t = T_{\mathrm{mod}}/2$ could be chosen to be $100\ \mathrm{ns} \leq t \leq 100\ \mathrm{s}$. Thus, two excitation cycles with oppositely circularly polarized excitation were defined and shown in figure 3.13(a).

The time-resolved measurement of the ρ_c is realized in both half-periods of excitation. By choosing a different time resolution for the multiscaler, the ρ_c can be measured and integrated as a function of T_{mod}. Figure 3.13(d) shows that both half-periods are symmetric concerning the excitation polarization switching time but not identical in amplitude, which indicates an imperfect tuning of the polarization elements for the laser beam. With the perfect alignment of the laser polarization, both half-periods in figure 3.13(d) should coincide in amplitude for two different polarization orientations $+45^\circ$ and -45°. This can be achieved by the correct orientation of the modulator relative to the laser beam (normal incidence at the input of the modulator, without refraction in the crystal body) and the correct selection of the offset and high voltage levels using the digital/analog high voltage amplifier. It should also be noted that the state of excitation polarization can be affected by the polarization effect of the cryostat windows and optical mirrors on the way to the sample.

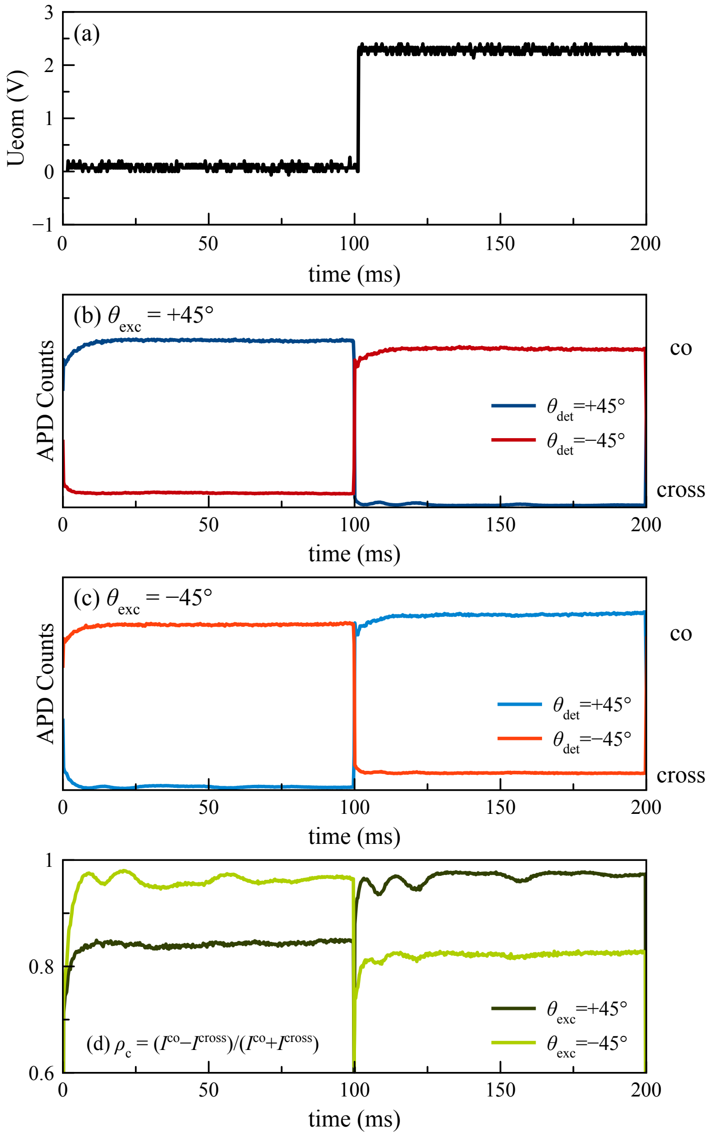

Figure 3.13: Calibration of the data acquisition using laser polarization. (a) Voltage protocol for the EOM. (b) APD signal time dependence for two different half-periods polarization helicities (G prism orientation respect to the polarizer axis is +45°). (c) APD signal time dependence for two different half-periods polarization helicities (GW prism orientation respect to the polarizer axis is −45°). (d) ρ_c time dependence for two different half-periods polarization helicities.

4 Nuclear spin cooling at weak magnetic fields in n-type GaAs

Adapted from Phys. Rev. B **96**, 205205 (2017).

The nuclear spin cooling rate by circularly polarized light is slowing down when the degree of circular polarization is modulated. Nuclear spins can be efficiently polarized when the polarization modulation frequency is smaller than T_1^{-1}. On the other hand, cooling can also be observed at higher modulation frequencies, when $\omega \gg T_1^{-1}$ due to the Knight field created by photoexcited electrons, which changes at the same frequency as the electron mean spin [MZ12]. In case of high modulation frequencies larger than T_2^{-1}, no nuclear spin cooling is possible unless the modulation frequency is equal to the Nuclear Magnetic Resonance (NMR) frequency in the applied magnetic field. Under these conditions, there is an effect known as resonant cooling [MZ12]. At even higher frequencies of intensity modulation, implemented by pulsed lasers with the pulse repetition rate exceeding 75 MHz, the resonantly driven electron spin system can be prepared in a highly excited state maintained at a large transverse magnetic field. Therefore the phase relaxation of the electron spin can be understood as a change of the temperature of the electron spin subsystem, and, to establish a temperature balance, NSS is cooled taking a significantly large Overhauser field [KA99b]. In addition, for strongly localized electron spins in the regime of electron-spin mode locking [GYS+06], e.g., in the single quantum dot, the Overhauser field provides a channel for the frequency focusing of the electron spin coherence [GSY+07]. This phenomenon is an alternative to the deep cooling and used for decoupling the electron spin from the nuclear spin ensemble.

It was shown that the maximal polarization of a single spin can reach 99% [FKI+15]. At the moment, the optimal strategy to achieve a highly polarized mesoscopic nuclear spin state is a subject of discussion while the current record in a single quantum dot is 80% [HB16] and, at least, an order of magnitude lower in quantum dot ensembles or bulk semiconductors. The efficiency of optical cooling of the NSS in the intermediate frequency range, $T_1^{-1} < \omega < T_2^{-1}$, has been investigated neither experimentally, not by a theoretical considerations. This question will be addressed in the current chapter.

A method called "spin inertia" [HZG+15] is adapted to examine the nuclear spin dynamics in n-doped GaAs. As it was shown, the Knight field oscillating synchronously with the electron mean spin provides an off-resonant NSS cooling up to modulation frequencies of the order of T_2^{-1}. On the other hand, the oscillating Knight field warms up the NSS. The competition beta these two processes leads to a cut-off frequency $\omega_{1/2}$ of nuclear spin cooling regime with $T_1^{-1} < \omega_{1/2} < T_2^{-1}$. Knowing the parameters of the electron spin system, one can use the measured $\omega_{1/2}$ to determine the parameters of the nuclear spin correlator, primarily the value of T_2 in weak magnetic fields, which cannot be directly measured by standard NMR techniques [SPK+17]. It should also be noted that T_2 time in solid-state systems is a hard-defined parameter and its measurement in low magnetic fields is complicated by the strong heterogeneity of physical parameters that determine the transverse relaxation time T_2. This question is also addressed in this chapter.

4.1 The investigated sample

The sample under study is a n-doped GaAs epitaxial layer grown by liquid-phase epitaxy on top of a semi-insulating (001) GaAs substrate. The 20 μm epitaxial layer was doped by Si providing a donor concentration $n_\mathrm{d} = 4 \times 10^{15}$ cm^{-3} [DKK+02, DKM+02]. The photoluminescence (PL) is excited by a tunable Ti: Sapphire laser operating at $E_\mathrm{exc} =$ 1.540 eV corresponding to the absorption edge of the GaAs band-to-band transition. The laser is focused on the sample surface through an achromatic doublet (focal distance $f = 200$ mm) into a spot of about 80 μm in diameter and the PL is collimated with the same lens throughout all subsequent measurements (see figure 3.5).

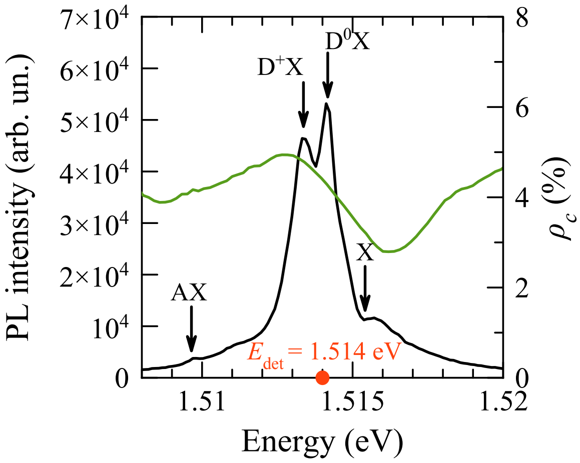

Figure 4.1: PL spectrum (excitation energy $E_\mathrm{exc} = 1.55$ eV) of n-doped GaAs measured at $B = 0$ T and $P_\mathrm{exc} = 5$ mW. Green line shows the spectral dependence of the PL circular polarization degree.

The helicity of optical excitation is controlled by the EOM (see chapter 3.1.2) driven by an analog EOM controller that is used to avoid a possible impact of higher-frequency harmonics as described in chapter 3.1.2. The PL is collected in reflection geometry, spectrally filtered by an 0.125 m fixed-slit monochromator eliminating the residual scattered light, and dispersed by a 0.5 m single-grating spectrometer followed by a gated single-photon counter (for details see chapter 3.2.1). The analysis of the circular polarization degree of the PL is done by a PEM followed by a GT polarizer (for details, see chapter 3.1).

The PL spectrum is shown in figure 4.1 has four distinct peaks corresponding to recombination of the exciton (X), the exciton bound on neutral and charged donors (D^0X and D^+X) as well as the exciton acceptor complex (AX). The spectrum also demonstrates a non-monotonic behavior of the PL circular polarization degree (green line). The spin polarization is governed mostly by electrons localized on donors [MZ12]. Following Refs. [MZ12] and [KDV+16], the part of the spectrum corresponding to D^0X transition at $E_{\text{det}} = 1.514$ eV is further analyzed in the magnetic field. The choice of this spectral energy is motivated by minimizing the field-independent offset of the PL polarization and obtaining maximal deviation of ρ_c from its equilibrium value detected at zero fields, ρ_0, when the magnetic field is applied [SPK+17].

4.2 Polarization recovery in a longitudinal magnetic field and the Hanle effect

As a primarily experimental method of characterization of the sample, a magnetic field applied along the light propagation axis (Faraday geometry) increases ρ_c, this effect is known as polarization recovery (PR) [see Fig. 4.2(a)]. In contrast, the application of a transverse magnetic field (Voigt geometry) leads to a decrease of ρ_c with an increasing field due to the Hanle effect [see Fig. 4.2(b)]. Such phenomena are typical for GaAs and used for determination of the characteristic values of the electron correlation time, τ_c, and the electron spin relaxation time, τ_s.

It is known that at high enough modulation frequency $f_{\text{mod}} \gg T_2^{-1}$ the nuclear spin polarization is negligible [Dya17], the Hanle curve shown in figure 4.2(b) is, to a good approximation, a Lorentzian:

$$\rho_c(B_x) = \frac{\rho_0}{1 + B_x^2/B_{1/2}^2} \tag{4.1}$$

with $\rho_0 = 0.036$ and $B_{1/2} = 2.7$ mT. The corresponding spin relaxation time for steady state conditions is evaluated as $T_s^{-1} = \tau^{-1} + \tau_s^{-1}$ where $T_s = \hbar/\mu_B g B_{1/2}$, $\mu_B = 9.274 \times 10^{-24}$ JT^{-1} is the Bohr magneton, $g = 0.44$ [WH77] is the electron g factor. Thus, the electron lifetime $\tau = 10$ ns [PLSS77] taking into account that $\tau_s = 20$ ns for conditions as evaluated from the fitting of the experimental data in figure **??**(b).

To obtain τ_c, the dependence of the ρ_c in figure **??**(a) on the longitudinal magnetic field B_z is measured. In this case, the electron spin z component increases due to a change of the spin relaxation time [WH77]. Supposing a simple field dependence [Dya17]: $\tau_s' = \tau_s(1 + \mu_B^2 g^2 B_z^2 \tau_c^2/\hbar^2)$ and $\rho_c = \rho_\infty \tau_s'/(\tau + \tau_s')$, it gives

$$\rho_c(B_z) = \frac{\rho_\infty}{1 + \frac{\tau}{\tau_s}\left[1 + (\mu_B g B_z \tau_c/\hbar)^2\right]^{-1}} \tag{4.2}$$

where ρ_∞ is the polarization degree reached in the limit of large magnetic fields.

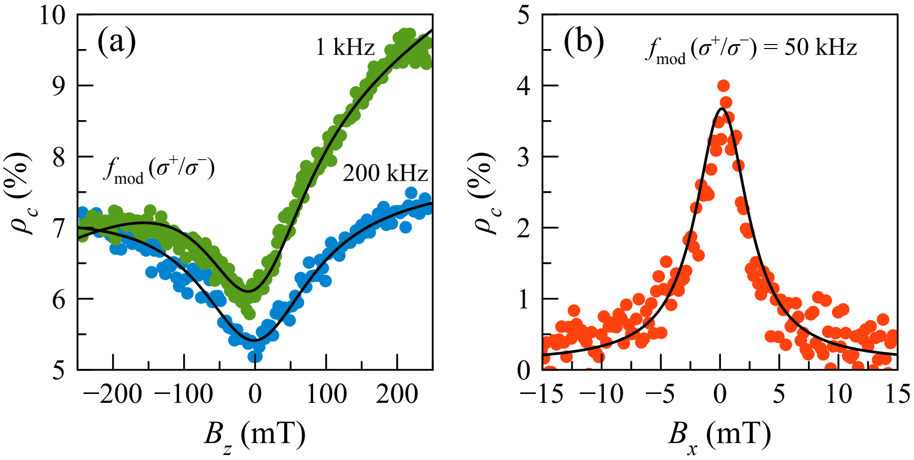

Figure 4.2: (a) Magnetic field dependencies of the circular polarization degree (Faraday configuration, $B_x = 0$) measured for the D^{0}X transition ($E_{\mathrm{det}} = 1.514$ eV) at fast modulation of the helicity of excitation $f_{\mathrm{mod}} = 200$ kHz (blue dots) and $f_{\mathrm{mod}} = 1$ kHz (green dots). The corresponding electron correlation time $\tau_c = 310$ ps. Solid lines in panels (a) and (b) result from fitting with Eqs. (4.1) and (4.2), respectively. (b) Circular polarization degree versus transverse magnetic field (Voigt geometry, $B_z = 0$) measured at alternating helicity of excitation $f_{\mathrm{mod}} = 50$ kHz. The electron spin relaxation time $\tau_s = 20$ ns is evaluated.

The ρ_c dependence on the longitudinal magnetic field up to $B_z = 0.25$ T is shown in figure 4.1(a). The electron spin polarization saturates at a certain value purporting to be a PR curve that represents a broad and inverted Lorentzian curve described by equation (4.2). The extracted correlation time of the donor bound electron is $\tau_c = 310$ ps. A small linear asymmetry of the PR amplitude at positive and negative values of the magnetic field is due to the equilibrium paramagnetic polarization of electron spins. On the other hand, a fast modulation of the pump helicity at $f_{\mathrm{mod}} = 200$ kHz removes this asymmetry, as shown in figure 4.1(a). The width of the obtained PR curve does not strongly depend on the frequency f_{mod} in the range of 0.9 – 12 kHz. This leads to the conclusion that the condition of short correlation time $\tau_c \ll \tau_s$ [DKM$^+$02] is fulfilled throughout the experiments reported in the rest of this chapter.

4.3 Measurement of the Knight field

As mentioned above, no dynamic nuclear polarization is expected if NSS is not subjected to an external magnetic field. If electrons are spin-polarized, the total magnetic field at the nucleus is a sum of the external magnetic field B and the mean Knight field B_e. It goes to zero if these two terms compensate each other, i.e. $B = -B_\mathrm{e}$ [Dya17]. In this case, the dip on the longitudinal magnetic field B_z dependence of the electron spin is seen in figure 4.3, indicating lower polarization of nuclei at $B = -B_\mathrm{e}$.

Figure 4.3 indicates that the Zeeman splitting does not disappear entirely and present due to the inhomogeneity of the electron density. It is impossible to precisely compensate the Knight field for all the nuclei interacting with the electron. The diminishing of the nuclear polarization at $B = -B_\mathrm{e}$ is also reflected in the polarization of PL because, at lower B_N, the electron spin relaxation rate is accelerated. This latter effect is associated with donor-bound electrons, which will be discussed later in this chapter.

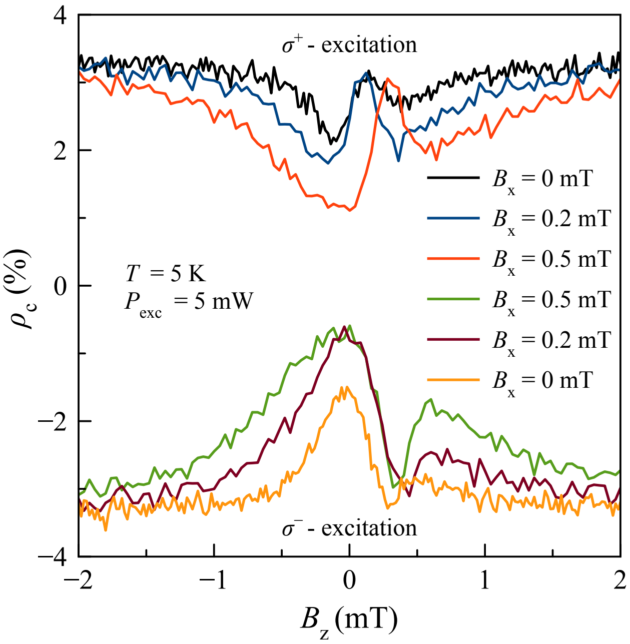

Figure 4.3: Polarization ρ_c of the PL as a function of applied external longitudinal magnetic field B_z, measured in the n-doped GaAs. The right deeps on the right side of the curves correspond to compensation of the mean Knight field B_e by the external magnetic fields. At these points, B_N is close to zero.

Even for such a simple measurement, it was evident that the Overhauser field modifies the energy spectrum of electrons, and, as a consequence, the efficiency of the nuclei polarization by electron changes. The electron spin and NSS reveal the behavior of the strongly coupled system with positive feedback, which, in turn, may be either positive or negative depending on the specific positions of electron energy levels, on the helicity of the excitation light and the sign of the total external magnetic field.

4.4 The spin inertia in the longitudinal magnetic field

In this subsection, the spin dynamics in a tilted external magnetic field was investigated. Scanning a longitudinal field B_z, a tiny additional PR signal in small longitudinal fields [see Fig. 4.4] can be observed. After applying a small transverse field B_x with a magnitude of the order of $B_{1/2}$ and scanning B_z, a wider PR signal [see Fig. 4.5(a)] can be found. These scans are presented in figure 4.5(a) where the relative comparison of several PR curves at $B_x = 0$ and $B_x = 1$ mT are given. It can be noted that the narrow recovery of ρ_c is observed already when $B_x = 0$, indicating the uncompensated transverse component of the laboratory magnetic field of about ±0.2 mT.

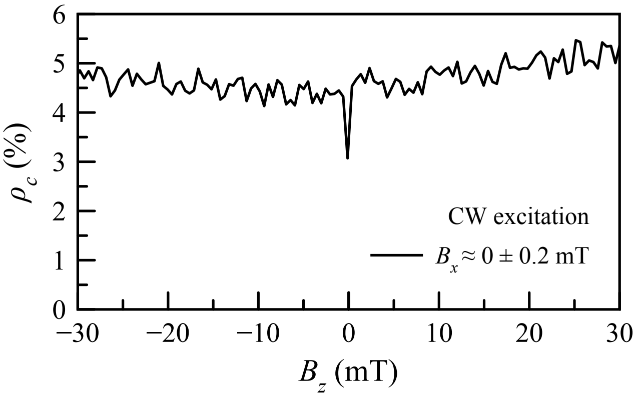

Figure 4.4: Manifestation of the additional tiny PR signal in small longitudinal fields (Faraday configuration, $B_x = 0$) measured for the D^{0}X transition ($E_{\text{det}} = 1.514$ eV) at CW excitation.

Using the measured PR curves, the dynamics of the PR curves was investigated. As shown in Ref. [HZG$^+$15], a measurement of the PR curves as a function of the modulation frequency, f_{mod}, provides information on the dynamics of the electron or nuclear spins. As one can see from figure 4.5(b), the amplitude of the dip centered near $B_z = 0$, A_{PR}, decreases with increasing f_{mod}. There is a suggestion that the observed polarization dynamics is associated with nuclear spin polarization: the polarization-modulated excitation influences on the nuclear spin cooling [MZ12], the cooled nuclear spin system is aligned by the static transverse field and create the nuclear field that enhances the Hanle effect. In order to study the dynamics of the Overhauser field, experimental data are processed according to Ref. [KDV$^+$16]. Starting with a set of Hanle curves obtained at fast modulation ($f_{\text{mod}} = 50$ kHz) is analyzed from which ρ_0 and $B_{1/2}$ are extracted as functions of P_{exc}. Next, the values of ρ_c ($B_z = 0$) demonstrated in figure 4.5(b) are associated with the corresponding points in the Hanle curves and the magnitude of the effective magnetic field B_{eff} acting on the electron spin is found.

It is important to note that the PR curves shown in figure 4.5(b) are obtained at a fixed transverse field $B_x = 1$ mT. Following the above, the Overhauser field can be expressed as $B_N = B_{\text{eff}} - B_x$.

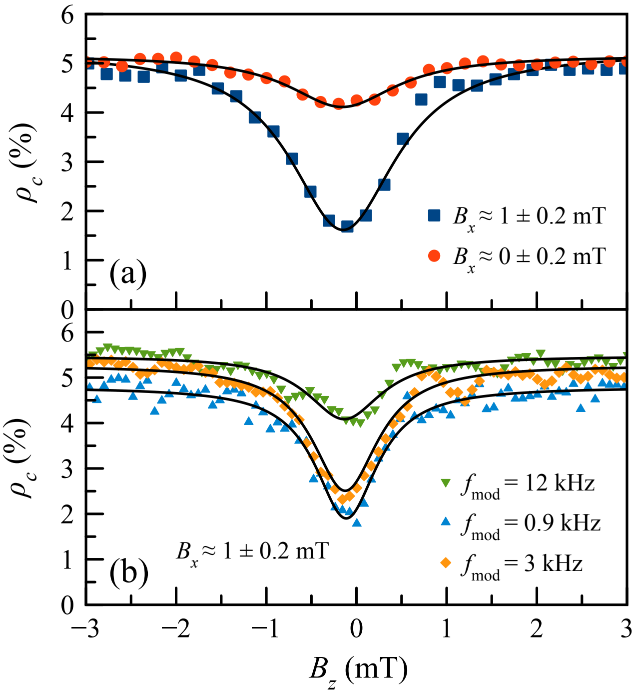

Figure 4.5: (a) Recovery of the PL circular polarization degree by a longitudinal magnetic field in absence of a transverse magnetic field (circles) and in presence of $B_x = 1$ mT (squares). (b) PR curves measured at different frequencies of modulation in presence of a transverse magnetic field. Solid lines in panels (a) and (b) result from fitting with a bell shaped function: $\rho_c(B_z) = \rho_{\text{sat}} - A_{\text{PR}}/\left(1 + B_z^2/\Delta_B^2\right)$ with ρ_{sat}, A_{PR} and Δ_B being fitting parameters.

The results of the performed analysis are shown in the figure 4.6. It is obvious that the dependencies B_N on the modulation frequency f_{mod} represent decreasing functions that are in the following expressed by equation (4.18), and the best fit for these dependencies are provided by Lorentzian functions with characteristic widths of about 1 kHz, which corresponds to time on the order of several milliseconds. The NSS polarization is suppressed when the frequency of modulation is close enough to or larger than T_2^{-1} [MZ12]. The observed phenomena, on the other hand, develops on a longer time

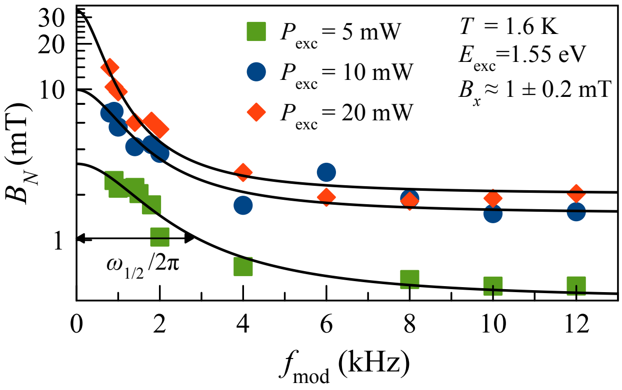

Figure 4.6: Calculated Overhauser fields (B_N) versus f_{mod}. Solid lines are fits with Lorentzian functions given by equation (4.20), from which the values of the cut-off frequencies $\omega_{1/2}$ are extracted.

scale ($0.5 \lesssim \omega_{1/2}/2\pi \lesssim 1.5$ kHz) and is power dependent. Summing up all the above in this section, it is shown that the observed cut-off frequency is not exactly T_2^{-1}, even though this data can be related to T_2 and can be used for its estimation.

4.5 Model: nuclear spin warm-up and cooling in the oscillating Knight field

Based on considerations found in Ref. [MZ12], the nature of the observed effects can be understood as follows. The observed phenomenon is measured for excitation by light with alternating helicity creating a time-dependent non-equilibrium average spin of the resident electrons [SPK+17]

$$\langle \mathbf{S} \rangle = S_0 \cos(\omega t), \tag{4.3}$$

where S_0 is the initial electron polarization and $\omega = 2\pi f_{\mathrm{mod}}$. As a result of the dynamic polarization, a time-dependent spin flow into the NSS appears given by $j(t) = Q\langle \mathbf{S}(t) \rangle / T_{1e}$, where $Q = 4I(I+1)/3$, I is the nuclear spin number and T_{1e} is the time of nuclear spin relaxation by electrons via the hyperfine interaction [MZ12].

The electron spin influences on the NSS also as an oscillating magnetic field (Knight field) $B_e = b_e \langle \mathbf{S} \rangle$. Given the fact that the nuclear spins are subjected to a magnetic field, the spin flow induces an energy flow

$$q_s(t) = -\hbar\gamma_N \left[B + B_e(t)\right] j(t) = -\frac{\hbar\gamma_N Q}{T_{1e}} \left[B_z S_0 \cos(\omega t) + b_e S_0^2 \cos^2(\omega t)\right]. \tag{4.4}$$

Here, γ_N is the nuclear gyromagnetic ratio, $B_e = b_e S_0$ is the Knight field amplitude with b_e being the strength of the Knight field of a fully polarized electron, and the negative sign reflects cooling of the NSS. On averaging over the modulation period, the first term in equation (4.4) vanishes, while the second one contributes to the time-averaged energy flow

$$\overline{q}_s = -\frac{Q}{2T_{1e}}\hbar\gamma_N b_e S_0^2. \tag{4.5}$$

On the other hand, the oscillating Knight field heats up the nuclear spins and the corresponding heating energy flow is

$$q_\omega(t) = -\hbar\gamma_N \frac{dB_e(t)}{dt} I_B(t) = \hbar\gamma_N \omega b_e S_0 \sin(\omega t) I_B(t), \tag{4.6}$$

where $I_B(t)$ is the projection of the time-dependent average nuclear spin on the direction of the Knight field. The time-dependent $I_B(t)$ includes two contributions: $I_B(t) = I'_B(t) + I''_B(t)$. The term $I'_B(t)$ is induced by the Knight field via the magnetic susceptibility, $\hat{\chi}(\omega)$, of the NSS as $I'_B(t) = \hat{\chi}(\omega)B_e(t)$. In turn, $I''_B(t)$ results from the accumulation of the spin flow $j(t)$ coming from optically pumped electrons. The relation of $I''_B(t)$ and $j(t)$ is determined by relaxation of the non-equilibrium nuclear spin and can be written as

$$I''_B(t) = \int_0^t G_N(t-\tau) j(\tau) d\tau, \tag{4.7}$$

where the Green function, $G_N(t)$, is expressed via a correlator of the nuclear spin fluctuations [Lan96]

$$G_N(\tau) = \frac{3}{I(I+1)} \left\langle \delta I(t) \delta I(t-\tau) \right\rangle. \tag{4.8}$$

As follows from the definition, $G_N(0) = 1$ and, at weak fields, it falls down on the time scale of T_2, so that $\int_0^\infty G_N(\tau)d\tau = T_2$.

Since I_B consists of two principal components, the energy flow is given by equation (4.6) also has two terms: $q_\omega = q'_\omega + q''_\omega$, which contribute to the energy balance in different ways. While, according to the fluctuation-dissipation theorem [Lan96], the imaginary part of susceptibility in the high-temperature approximation is inversely proportional to the system temperature: $\hat{\chi}_\omega \propto \Theta_N^{-1}$, the first term, $q'_\omega(t) \propto I'_B(t)$, depends on the nuclear spin temperature Θ_N explicitly. By averaging over the modulation period, one can find

$$\overline{q}'_\omega(t) = \frac{Q}{8}(\hbar\gamma_N)^2\omega^2(b_e S_0)^2\beta\hat{G}'_\omega. \tag{4.9}$$

Here, $\beta = (k_B\Theta_N)^{-1}$ and

$$\hat{G}'_\omega = \int_0^\infty G_N(\tau)\cos(\omega\tau)\,d\tau. \tag{4.10}$$

Consequently, $\overline{q}'_\omega$ provides an additional energy relaxation channel, known as the warm-up of the NSS by the oscillating Knight field. The second term, $q''_\omega(t) \propto I''_B(t)$, on the other hand, does not explicitly depend on Θ_N:

$$\overline{q}''_\omega(t) = \frac{\hbar\gamma_N b_e Q S_0^2}{2T_{1e}}\omega\hat{G}''_\omega \tag{4.11}$$

where

$$\hat{G}''_\omega = \int_0^\infty G_N(\tau)\sin(\omega\tau)\,d\tau. \tag{4.12}$$

Therefore, $\overline{q}''_\omega(t)$ enters the balance equation for the inverse spin temperature β as a source, similarly to $\overline{q}_s$.

The balance equation reads as

$$\frac{\partial\beta}{\partial t} = -\frac{\beta}{T_1} + \frac{\overline{q}_s + \overline{q}'_\omega + \overline{q}''_\omega}{C_N}, \tag{4.13}$$

where

$$C_N = \frac{1}{3}I(I+1)(\hbar\gamma_N)^2(B^2 + B_L^2) \tag{4.14}$$

is the heat capacity of the NSS. Taking $\partial\beta/\partial t = 0$ the following expression for the inverse spin temperature can be obtained

$$\beta = -\left(1 + \frac{1}{2}\frac{b_e^2 S_0^2}{B^2 + B_L^2}\omega T_1 \hat{G}'_\omega\right)^{-1} \frac{3T_1 b_e Q S_0^2}{2I(I+1)T_{1e}\hbar\gamma_N(B^2 + B_L^2)}\left(1 - \omega\hat{G}''_\omega\right). \tag{4.15}$$

The steady-state nuclear spin polarization corresponding to β and established in the external magnetic field is given by

$$\frac{\langle I\rangle}{I} = \frac{I+1}{3}\hbar\gamma_N\beta B = -\frac{B b_e Q S_0^2 T_1}{2IT_{1e}}\left(1 + \frac{1}{2}\frac{b_e^2 S_0^2}{B^2 + B_L^2}\omega^2 T_1 \hat{G}'_\omega\right)^{-1}\frac{1 - \omega\hat{G}''_\omega}{B^2 + B_L^2}. \tag{4.16}$$

In the vicinity of a donor, $T_1 \approx T_{1e}$ and estimate its value according to Ref. [DP75]

$$\frac{1}{T_{1e}} = \frac{2}{3}S(S+1)b_e^2\gamma_N^2\tau_c\frac{B^2 + \xi B_L^2}{B^2 + B_L^2}, \tag{4.17}$$

where $\xi \leq 3$. Remarkably, the steady-state nuclear spin polarization linearly scales with b_e, as follows from equation (4.16) when T_1 is determined by equation (4.17). Thus, the normalized frequency dependence

$$\frac{\langle I\rangle_\omega}{\langle I\rangle_0} = \left(1 + \omega^2\hat{G}'_\omega\frac{S_0^2}{\gamma_N^2(B^2 + \xi B_L^2)\tau_c}\right)^{-1}\left(1 - \omega\hat{G}''_\omega\right) \tag{4.18}$$

does not contain b_e and, therefore, is not sensitive to the shape of the wave function of the donor-bound electron. Hence, equation (4.18) can be used universally.

4.6 The nuclear spin correlator

At high frequencies of polarization modulation the following condition is fulfilled

$$\lim_{\omega\to\infty}\omega\hat{G}''_\omega = G_N(0) = 1. \tag{4.19}$$

Therefore, $\langle I \rangle_\omega$ approaches to zero. For this reason, no cooling of the NSS is possible at the high modulation frequency, i.e., at $\omega \gg T_2^{-1}$. The exception is the case when a strong transverse field is applied, and $G_N(t)$ oscillates at the frequency of the nuclear magnetic resonance. In this case, resonant cooling is observed [MZ12].

On the other hand, at low frequencies of modulation, $\omega \ll T_2^{-1}$, $1 - \omega \hat{G}''_\omega \simeq 1$ and $\hat{G}'_\omega \simeq \hat{G}'_0$. As a result, equation (4.18) simplifies to

$$\frac{\langle I \rangle_\omega}{\langle I \rangle_0} = \frac{1}{1 + \omega^2/\omega_{1/2}^2} \tag{4.20}$$

where the cut-off frequency is given by

$$\omega_{1/2} = \frac{1}{S_0} \sqrt{\frac{\tau_c}{\hat{G}'_0}} \gamma_N \sqrt{B^2 + \xi B_L^2}. \tag{4.21}$$

Note that $\omega_{1/2}^{-1}$ is not equal to any nuclear spin relaxation time, neither T_1 nor T_2, but related to T_2 via the zero-frequency Fourier component of G_N.

The magnitude of S_0 can be extracted from the experiment assuming that $\rho_0 = S_0$. As shown in figure 4.7(a), the power dependence of S_0 demonstrates saturation behavior that can be fitted with a single exponent, this follows from a rate equation for the populations of the spin-up and spin-down states defining P_{exc}. The frequency dependencies of the Overhauser field shown in figure 4.7 are fitted with Lorentzian functions, from which the cut-off frequencies are extracted as a function of the excitation power P_{exc}. Taking into account that τ_c does not depend on P_{exc}, as shown in figure 4.7(b), the power dependence of $\omega_{1/2}$ is determined by S_0 and represents a curve decaying with increasing P_{exc}, as shown in figure 4.7(c). Equation (4.21) was used to fit this dependence with a single variable parameter $\hat{G}'_0 \approx 12\ \mu s$, as displayed by the solid line in the figure 4.7(c). In the equation 4.21 $\gamma_N/(2\pi) \approx 9.3$ kHz/mT as an estimate for the nuclear gyromagnetic ratio averaged over all nuclear species (^{75}As, ^{69}Ga, ^{71}Ga with weights 0.5, 0.3 and 0.2, respectively [HBDM+01]), $\xi = 3$, and $B_L = 0.15$ mT [VCS+17].

Fitting experimental data the value of $\hat{G}'_0$ was determined. It schould be noted that when $B \ll B_L$, $\hat{G}'_0 \approx T_2$. At $B = 0$, the correlator G'_ω is centered at zero frequency, and at the field, $B > B_L$ its maximum is shifted to the Larmor frequency in the field B. Therefore, the zero-frequency value, in this condition, does not determine T_2, and the relaxation time should be extracted from the spectrum G'_ω. To evaluate T_2 from experimental data, a simple model of the nuclear spin correlator was implemented. Consider, the correlator in a weak external magnetic field to have the form of a decaying oscillation

$$G_N(t) = \cos(\Omega_L t) \exp(-t/T_2), \tag{4.22}$$

with the Fourier components being:

$$\hat{G}'_\omega = \frac{T_2}{2} \left(\frac{1}{1 + (\Omega_L + \omega)^2 T_2^2} + \frac{1}{1 + (\Omega_L - \omega)^2 T_2^2} \right), \tag{4.23a}$$

$$\hat{G}''_\omega = \frac{T_2}{2} \left(\frac{T_2(\Omega_L + \omega)}{1 + (\Omega_L + \omega)^2 T_2^2} + \frac{T_2(\Omega_L - \omega)}{1 + (\Omega_L - \omega)^2 T_2^2} \right), \tag{4.23b}$$

where $\Omega_L = \gamma_N B$ is the nuclear Larmor frequency.

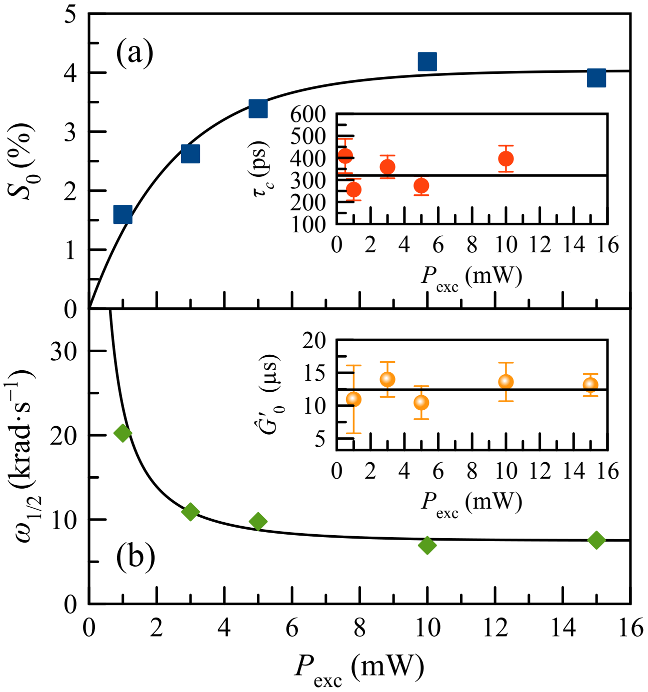

Figure 4.7: (a) Electron mean spin polarization (squares) and its fit with a saturating exponential function: $S_0(P_{\rm exc}) = S_\infty[1 - \exp(-P_{\rm exc}/P_0)]$ (solid line). The fit parameters are: $S_\infty = 0.041$ and $P_0 = 2.6$ mW. Inset shows the power dependence of the electron correlation time. The solid line shows a linear fit with $\tau_c = 320$ ps. (b) Cut-off frequency of the nuclear field build-up versus excitation power $P_{\rm exc}$ (diamonds). The solid line shows a fit of the data with equation (4.21). Inset shows the corresponding nuclear spin correlator $\hat{G}'_0$ as a result of normalization of $\omega_{1/2}$ to S_0. The solid line shows a linear fit with $\hat{G}'_0 = 12\ \mu s$.

Having this approximation, the fitting parameter $\hat{G}'_0$ extracted from the experimental data provides an estimate of the nuclear spin relaxation time T_2 in a weak external magnetic field. Since the correlator at $B_x = 1$ mT demonstrates clearly a resonant type of behavior (see Fig. 4.8), its value close to zero frequency is determined by the isotope with the smallest gyromagnetic ratio: $\gamma_N[^{75}\text{As}] = 4.596 \times 10^7$ rad/(Ts), $\gamma_N[^{69}\text{Ga}] = 6.439 \times 10^7$ rad/(Ts), $\gamma_N[^{71}\text{Ga}] = 8.181 \times 10^7$ rad/(Ts), i.e. arsenic. Therefore, it seems reasonable to plot the frequency dependence $\hat{G}'_\omega$ calculated for $B = 0$ and 1 mT

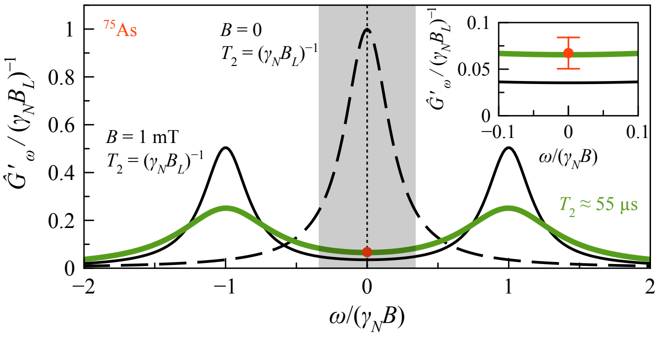

Figure 4.8: Normalized real Fourier component of the correlator of the nuclear-nuclear interactions versus frequency for $B = 0$ (dashed line) and $B = 1$ mT (solid lines) calculated for the ^{75}As nuclear species. Filled area defines the range of frequencies $\omega < \omega_{1/2}$ observed in the experiment. The red filled circle represents the value of the correlator determined from experiment [see inset on the Fig. 4.7(c)]. The thick red line represents the $\hat{G}'_\omega$ calculated for the best fit of G'_0 ($T_2 = 55\ \mu s$) and the thin, solid and dashed black lines are calculated for the spin-spin relaxation time $T_2 = (\gamma_N B_L)^{-1} \approx 114\ \mu s$.

(Fig. 4.8). Thus, calculating the value $T_2 = (\gamma_N B_L)^{-1} \approx 114\ \mu s$, which is in agreement with accepted and previously measured values $T_2 \sim 10^{-4}$ s [PLSS77]. As one can see from the figure 4.8, the correlator has the maximum value of $\hat{G}'_0 = T_2$ at $B = 0$. In a situation where the external field is not equal to zero, the Fourier maxima are shifted markedly to the positive and negative frequency values of the Larmor precession, and $\hat{G}'_\omega$ loses its value in amplitude. However, the value of $\hat{G}'_\omega$ extracted from the experiment still larger than the simple model predicts (point in Fig. 4.8). Therefore, an extended model for the correlator $G_N(t)$ needs to be developed which explains the experimental value of $G'_0 = 12\ \mu s$. It should be especially emphasized that for the frequencies of modulation used in all experiments (demonstrated with the filled area in Fig. 4.8), the correlator G'_ω weakly changes and its value equal to G'_0 with good fitting accuracy. This result supports the assumptions of the theoretical model. The value of $T_2 = 55\ \mu s$, which is two times smaller than the one estimated through $B_L \approx 0.15$ mT [PLSS77] that was used to evaluate the complex behavior of the nuclear spin relaxation in NMR [CRWB11, OIS+14]. It should be noted that it is also several times smaller than the $T_2 = 100\ \mu s$ measured in GaAs/AlGaAs quantum wells [SKM+06] and $T_2 = 270\ \mu s$ for lattice-matched GaAs/AlGaAs quantum dots [MKS+11], where the measurements were done at $B \sim 1$ T. The assumption of why this is so may be as follows. For the weak-field experiments, the external magnetic field B is comparable to the local field B_L and, therefore, the non-secular part of the dipole-dipole interaction may come into play, thus increasing the rate of the nuclear spin relaxation.

4.7 Conclusions

To conclude the main results of this chapter, the spin relaxation of the nuclear spin ensemble have been studied in n-doped GaAs crystal by a modified spin inertia method. It was shown that optical pumping with the light of alternating helicity induces a fast build-up of the nuclear field. The dynamics is observed on a sub-second time scale showing a frequency cut-off varied by several times with increasing the pumping power. The experimental results are interpreted within a developed model, which predicts a drop of the nuclear spin polarization when the light helicity modulation rate reaches a characteristic frequency $\omega_{1/2}$, determined by the spin correlation time of donor-bound electrons and the nuclear spin-spin relaxation time T_2, which was estimated as $T_2 = 55\ \mu s$, i.e. noticeably shorter than the $T_2 \sim 2 \times 10^{-4}$ s determined by NMR methods at high magnetic fields.

5 Subsecond nuclear spin dynamics in n-type GaAs

Adapted from Phys. Rev. B **99**, 075307 (2019).

The spin fluctuations of lattice nuclei are known to be one of the main factors limiting spin coherence of charge carriers in III-V semiconductors at cryogenic temperatures [MER02, KLG03]. The hyperfine interaction couples the electron or hole spin to the nuclear spin system (NSS).The NSS comprising N spins produces a fluctuation scaled as $\sqrt{N}$ that, for example, for nuclei located inside donor's orbit ($N \sim 10^5$), corresponds to a randomly distributed effective magnetic field of about several mT in GaAs, i.e., the characteristic spin relaxation time might be as short as a few ns. On the other hand, the NSS acts as a thermal bath, well isolated from the crystal lattice and characterized by a spin temperature different from the lattice temperature. To achieve a spin state characterized by a reduced influence of the nuclear spin fluctuations on the carrier spin coherence, either for the electron or hole spin, several ways are proposed, including optical orientation [PLSS77, MZ12] in combination with the adiabatic demagnetization [MZ12]. Particular effort has been achieved by utilizing pulsed techniques based on the electron-nuclear spin system dynamic decoupling [BFN$^+$11, MMC$^+$17] and multiple-pulse nuclear magnetic resonance [ELFS02, ES04].

In 1982 D. Paget has described the pattern of optical polarization of nuclear spins in GaAs at low temperatures [Pag82]. The essence of the proposed description as follows, optically-oriented spins of localized electrons dynamically polarize nuclear spins in the vicinity of localization centers (typically, donor impurities); the nuclear spin polarization spreads over the crystal by spin diffusion mediated by the dipole-dipole interaction. D. Paget measured the time increment of the dynamic polarization by using optically detected NMR in high-purity GaAs and found it to be about 3 seconds [Pag82].

Abragam's classic theory [Abr61] postulates that the relaxation time of nuclear spins due to their hyperfine coupling with electrons, T_{1e}, is inversely proportional to the mean squared hyperfine frequency ω_{hf} and to the electron spin correlation time τ_c

$$T_{1e} \propto \left[\langle\omega_{\text{hf}}^2\rangle\,\tau_c\right]^{-1}. \tag{5.1}$$

After determining the electron spin density in the probed region (at the distance of one Bohr radius of the hydrogen-like shallow donor from the impurity center), Paget calculated the spin correlation time of the donor-bound electron, $\tau_c \approx 25$ ps. This relatively short time was attributed to spin-exchange with itinerant photoexcited electrons in the conduction band. Theoretical calculations of the exchange scattering rates made by D. Paget [Pag81] and K.V. Kavokin [Kav08], support this interpretation. Recently, T_{1e}

of about 10 seconds was measured, using off-resonant Faraday rotation [GCG$^+$13], for nuclei interacting with localized electrons in a structure with free electron gas, where strong exchange scattering is presented even in the absence of optical pumping. From the research made by Giri *et al.* [GCG$^+$13] an estimate of $\tau_c \approx 10$ ps was found, corroborating the Paget model [Pag82].

For n-doped semiconductors with donor concentrations n_D notably below the metal-to-insulator transition and characterized by long electron spin lifetimes [DKK$^+$02] and, therefore, very prospective for achieving a high polarization of the NSS, the electron spin correlation times are above the standard values. For example, in n-GaAs with $n_D \approx 10^{15}$ cm^{-3} spin correlation time τ_c is about 300 ps [DKK$^+$02], which demonstrates a very efficient nuclear-spin relaxation near donors, with $T_{1e} \approx 300$ ms. Therefore, donor impurities act as “killer centers” for nuclear spin polarization. The nuclei situated far from the donors lose their spin polarization by spin diffusion towards donors [KDV$^+$16], which determines a much longer time $T_{\text{bulk}} \sim 10^2$ s, characterizing their spin relaxation rate. In magnetic fields weaker than the local fields of nuclear spin-spin interactions, the relaxation by quadrupole interaction takes the lead over all other interactions. It wouldn't be superfluous to point out that nuclear polarization and relaxation by spin diffusion from or to donors in n-type semiconductors are well studied experimentally [MZ12]. But on the other hand, the millisecond time scale of nuclear dynamic polarization and hyperfine relaxation for donor-bound electrons have not been experimentally measured, for the lack of appropriate experimental methods.

Another important aspect of the investigations of nuclear spin dynamics of donor-bound electrons is the implementation of the nuclear spin cooling protocols for decoherence control in semiconductor structures. However, so far, this was hindered by the fact that the thermodynamics and kinetics of the optically cooled NSS have been poorly investigated even in bulk GaAs. In this particular case, the electron spin is used as a carrier of angular momentum transferred from light onto the nuclei, thereby establishing dynamic nuclear spin polarization. Importantly, the application of the external magnetic field exceeding the magnitude of the local fields of the dipole-dipole interaction. If in the steady-state, the populations of nuclear spin sublevels split in this field, are distributed with Boltzman statistics, the state of this distribution might be described by a single parameter, the nuclear spin temperature, which is verified for GaAs bulk [VCS$^+$18] and individual quantum dots (QD) [CUZ$^+$17] and might be hindered for strained QDs due to the enhanced quadrupole interaction [MKI09]. There are two main approaches to achieving the lowest nuclear spin temperatures: the adiabatic demagnetization [OL97] into small external magnetic fields $B \sim B_L$ and by demagnetization with radio-frequency sequences in the rotating frame [CGCA70] at high external magnetic fields at $B \gg B_L$. For both these approaches, the initial polarization of nuclear spins along B is required.

In this chapter, a method based on measuring the Hanle effect (depolarization of photoluminescence by magnetic fields) with millisecond time resolution [SPK$^+$17] to study the nuclear spin dynamics in the vicinity of donors in n-GaAs was used. The rise times of the nuclear spin polarization under optical pumping and its decay times in the dark were measured. The relation between these times supports the suggestion of

Ref. [Pag82] on the crucial role of photoexcited electrons in the nuclear spin dynamics. For experiments with NSS cooling, several questions were addressed, i) what is the minimum nuclear spin temperature that can be achieved in the initial short-period stage, and ii) how fast this initial stage should be to achieve a saturation of the dynamically pumped Overhauser field. The influence of fast polarization modulation on the cooling dynamics of donor-bound nuclear spins in the external magnetic field, thus evaluating the dynamics of nuclear spin temperature establishment in n-GaAs was studied.

5.1 Spin relaxation of the bulk nuclei

The n-doped GaAs epitaxial layer (for the detailed description of the sample see section 4.1) at D^0X transition is selected to measure the spin polarization of electrons interacting with the nuclear spins situated in the vicinity of donor centers.

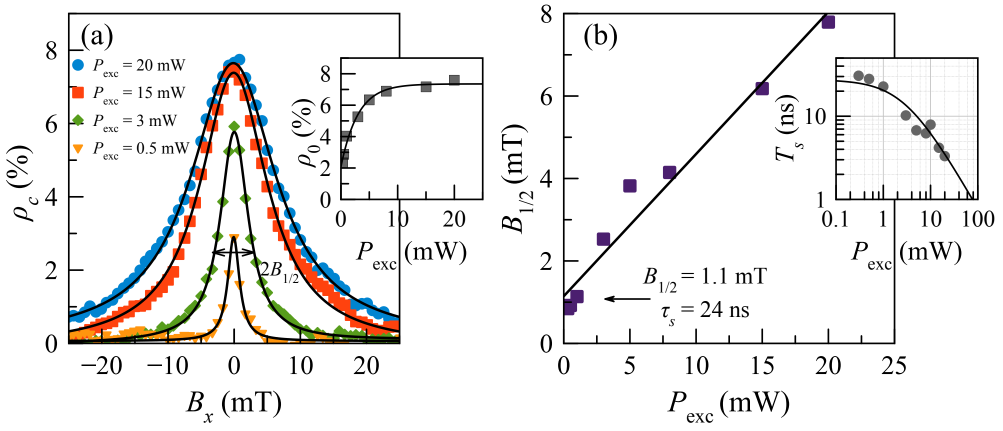

Figure 5.1: (a) The Hanle curves of D^0X line measured for fast polarization modulation $f_{\text{mod}}(\sigma^+/\sigma^-) = 50$ kHz at various pumping powers (symbols) and their fitting with Lorentzians (lines). Inset shows the power dependence of the Hanle curve amplitude ρ_0 (squares) and its fit with an exponential function (line). (b) Power dependence of $B_{1/2}$ (squares) and its linear fit (line). Inset shows the power dependence of the electron spin lifetime (circles) extracted from the HWHM of the Hanle curves and its linear fit (line).

As it was demonstrated in section 4.2, in order to minimize the possible action of the nuclear spin polarization, the helicity of the pumping light (σ^+/σ^-) was modulated at a high frequency. In case when the frequency of polarization modulation of light between σ^+ and σ^- f_{mod} exceeds 10 kHz, the NSS remains unpolarized, and the dependence $\rho_c(B)$ (the Hanle curve) obeys Lorentzian law with the half-width at HWHM, $B_{1/2}$ [MZ12]. In figure 5.1(a), a set of Hanle curves measured at different powers of excitation, using fast modulation of the helicity of the pumping light at $f_{\text{mod}} = 50$ kHz, is shown. Therefore, when the conditions $f_{\text{mod}} \gg T_2^{-1}$ are satisfied (where T_2 is the thermal equilibrium establishment time) the nuclear spin polarization is negligible [MZ12]. It should be noted that the dynamics of reaching this equilibrium may be different for different isotopes because of different neighboring spins and, therefore, different dipole-dipole or quadrupole interactions exhibited by these nuclei [CRWB11].

The Hanle curves shown in figure 5.1(a) are, to a good approximation, Lorentzians, $\rho_c(B_x) = \rho_0 / \left(1 + B_x^2/B_{1/2}^2\right)$. Thus, the electron spin lifetime, $T_s = \hbar/(\mu_B g_e B_{1/2})$ can be calculated, where g_e is the electron g-factor in GaAs [MZ12]. As seen from the inset in figure 5.1(b), T_s becomes shorter with increasing excitation power due to the increase of recombination rate of electrons with photoexcited holes. By plotting the power dependence of the $B_{1/2}$ values and taking the cut-off at zero pump power with $B_{1/2} = 1.1$ mT and $|g_e| = 0.44$, the intrinsic electron-spin relaxation time $\tau_s = 24$ ns is extracted [see Fig. 5.1(b)]. The inset in figure 5.1(a) shows the power dependence of the electron spin polarization degree determined at zero magnetic fields, ρ_0. At pumping powers $P_{\text{exc}} \gtrsim 5$ mW ($W_{\text{exc}} = 200$ W/cm^2), ρ_0 is saturated, while the spin lifetime decreases. The power of $P_{\text{exc}} = 5$ mW provides efficient pumping of the NSS and will be used in all the experiments described in the following chapter.

As it is was mentioned above, the nuclear spin dynamics in n-GaAs is characterized by two timescales: the short time of the hyperfine relaxation inside the donor orbit ($\sim 10^{-1}$ s) and the long time of spin diffusion far from donor centers ($\sim 10^{2}$ s) [MZ12]. Both times are experimentally demonstrated in the current chapter.

In order to investigate the spin relaxation time of the bulk nuclei, the experimental protocol [MZ12] shown in figure 5.2(a) was implemented. The electron-nuclear spin system is pumped with circularly-polarized light during 5 minutes in the longitudinal magnetic fields $B_z = \pm 2$ mT. After that (at $t = 0$ s), the longitudinal magnetic field is switched off and a small transverse field $B_x \approx 0.5 \pm 0.05$ mT is turned on in about 100 milliseconds. With switching off both the pumping light and the longitudinal field, the nuclear spin cooling is interrupted, and the further dynamics of the electron spin polarization is driven by nuclear spin demagnetization in the small transverse magnetic field B_x. As evidence of this demagnetization, the degree of electron spin polarization saturates near the level corresponding to the stationary value S_0 in the applied magnetic field B_x [see Fig. 5.2(b)].

Depending on the mutual orientation of the mean electron spin and longitudinal magnetic field B_z during the cooling period, the Overhauser field develops in the direction along with B_z or opposite to B_z. Consequently, at $t = 0$ s the B_N is directed either along B_x or opposite to it [MZ12]. As a result, the curves shown in figure 5.2(b) have different behavior over time. In order to relate the time dependence of ρ_c, shown in figure 5.2, to the Overhauser field B_N decay, the model represented in Ref. [GCV$^+$12] was used. At $t > 0$, $\rho_c(t)$ represents the time evolution of a point in the Hanle curve where the total magnetic field, including the time-dependent Overhauser field, acting on the electron spin is aligned along or against the applied external magnetic field B_x, it is given by the following equation

$$\rho_c \propto \left[1 + \left(B_x + B_N(t=0)e^{-t/T_{\text{bulk}}}\right)^2 / B_{1/2}^2\right]^{-1}, \tag{5.2}$$

where $B_{1/2}$ is the Hanle curve HWHM measured at the same excitation power with rapidly modulated pumping helicity [see Fig. 5.1(b)], the parameters $B_N(t=0)$ and T_{bulk} are obtained from fitting. The dynamics of the Overhauser field decay is characterized by a monoexponential process with characteristic time $T_{\text{bulk}} = 90$ s for $B_z = +2$ mT and $T_{\text{bulk}} = 120$ s for $B_z = -2$ mT. These times are of the same order of magnitude as those obtained earlier for the nuclear spin relaxation in bulk n-GaAs [VCS+17]. It is supposed that the difference between these relaxation times is due to a weak dynamic polarization of nuclear spins by the circularly polarized pump light in the transverse magnetic field. This influence on the nuclear polarization occurs due to nuclear spin cooling in the Knight field which creates the Overhauser field that is always directed along B_x [MZ12]. Feeling the impact of the relaxation of nuclear polarization, this effect either increases or decreases T_{bulk}, depending on the initial direction of B_N.

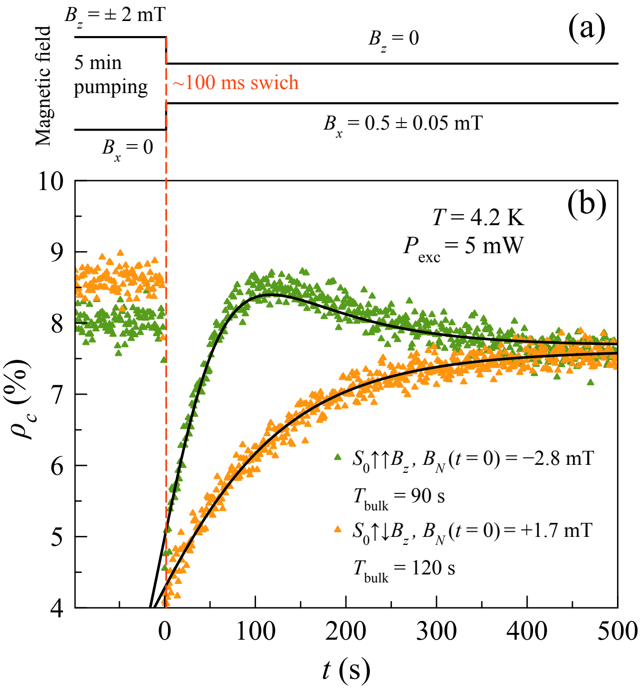

Figure 5.2: (a) Schematic of the pumping protocol. (b) Time dependence of the PL circular polarization degree after demagnetization from the longitudinal $B_z = +2$ mT (green curve) and $B_z = -2$ mT (orange curve) fields in a small transverse magnetic field $B_x = 0.5 \pm 0.05$ mT and its fitting (solid lines) with equation (5.2).

The time resolution used in the experiment represented in figure 5.2(b) is insufficient to resolve the fast millisecond nuclear spin dynamics in the vicinity of the donor center. In order to study the dynamics of the onset of the nuclear spin polarization under pumping, the time-resolved detection of the light intensity was used [SPK+19].

5.2 Time-resolved spin dynamics in the Hanle effect

To prove the existence of a fast nuclear spin pumping dynamics, the time protocol shown in figure 5.3(a) was used, where the pumping helicity is alternated each 500 ms.

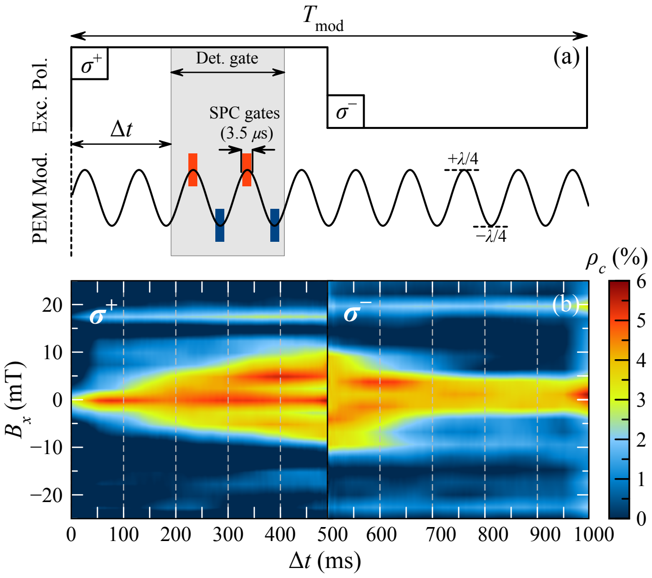

Figure 5.3: (a) Schematics of the measurement protocol. (b) Dynamics of ρ_c measured for the σ^+ and σ^- half-periods ($T_{\mathrm{mod}} = 1$ s) at different B_x and fixed $B_z = +2$ mT.

The extracted time dependence of ρ_c is mapped in figure 5.3(b) for B_x varied from -25 to $+25$ mT at fixed value of $B_z = +2$ mT. The time resolution in figure 5.3(b) is $\delta t = 2$ ms. B_x is scanned very slowly because such a measurement requires a long accumulation time for the time traces of the ρ_c dynamics. Each slice of figure 5.3(b) at a given time interval represents a Hanle curve. Starting from the first 100 ms, the Hanle curve is almost Lorentzian, with the maximum at $B_x = 0$. Next, one can see the development of additional peaks (shoulders), which are shifting towards higher fields with time. These dynamics occurs due to the onset of the Overhauser field, partly compensating for the external magnetic field. In contrast, in the next half-period, the pumping helicity is switched for the opposite, and the Overhauser field adds to the external field, which leads to the destruction of side peaks and narrowing of the Hanle curve by the end of the modulation period.

To explore further details of the experimental data shown in figure 5.3(b), the time-resolved Hanle measurement (see section 3.2.3) was implemented. Using the same period $T_{\mathrm{mod}} = 1$ s of excitation polarization, the 50 ms long detection gate sequentially scans over the modulation period [see Fig. 5.3(a)]. The Hanle curves are measured by scanning the B_x field [with the scanning rate similar to that used for the measurements in figure 5.3(b)] at fixed $B_z = +2$ mT for various delay times Δt. Examples of the Hanle curves obtained using this detection protocol are shown in figure 5.4(a). Using this method, it is possible to qualitatively estimate the time of the Hanle curve evolution shown in the colormaps of figure 5.3(b). However, with the upgrade of time resolution, the signal to noise ratio is increased and the evolution of the Overhauser field can be assessed more qualitatively.

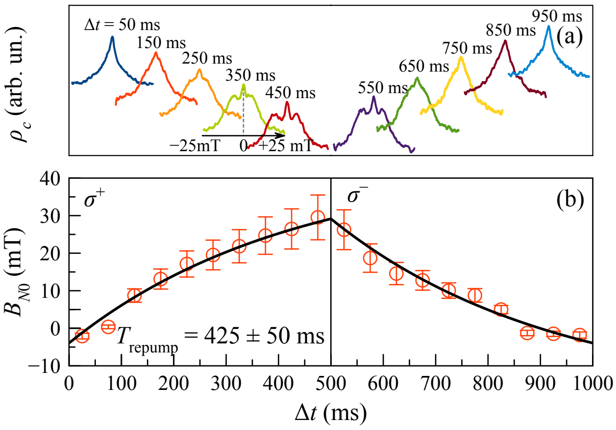

Figure 5.4: (a) Hanle curves corresponding to the gated detection in the time intervals shown in the figure 5.3(b). (b) Magnitude of the Overhauser field, B_{N0}, extracted from fitting the Hanle curves (symbols) with equation (5.5) (solid line).

The presence of the shoulders in the Hanle curves can be understood as a result of the partial compensation of the external magnetic field by the Overhauser field. The electron spin polarization is governed by the balance of the generation of oriented electrons by circularly polarized light, S_0, and their spin depolarization caused by Larmor precession in the total magnetic field $B_\Sigma = B + B_N$, as well as by the electron spin relaxation.

In zero magnetic field, $S_z(0) = S_0/(1 + \tau/\tau_s)$, where τ is the electron lifetime and the dependence of z-projection of the electron spin on the magnetic field is given by the following expression [see Fig. 5.5]:

$$S_z(B) = S_{z\parallel} + S_{z\perp} = S_z(0)\frac{(B_z + B_{Nz})^2}{B_\Sigma^2} + S_z(0)\frac{(B_x + B_{Nx})^2}{B_\Sigma^2}\frac{1}{1 + B_\Sigma^2/B_{1/2}^2}, \tag{5.3}$$

where $B_\Sigma^2 = (B_z + B_{Nz})^2 + (B_x + B_{Nx})^2$ is the total field acting on the electron spin and $B_{1/2}$ is the Hanle amplitude and HWHM in the absence of the nuclear spin polarization, while B_{Nx} and B_{N_z} are the Overhauser field projections.

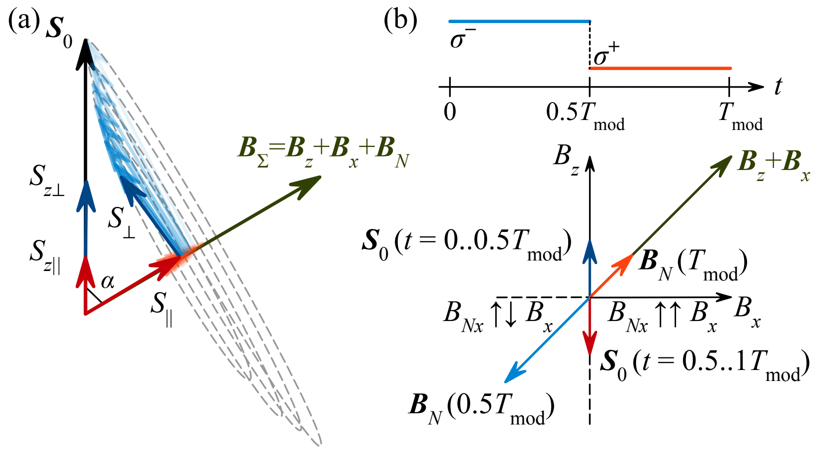

Figure 5.5: Diagram showing the various components of the electron (a) and nuclear (b) spins in an tilted external magnetic field (the Hanle effect for oblique geometry). The sign of the Overhauser field is dependent on the orientation of the pump (σ^+ or σ^-) as follows from the inset of panel (b).

The time dependence of B_{Nx} and B_{N_z} can be evaluated [see Fig. 5.5] as

$$B_{Nx} = \frac{B_z B_x}{B_z^2 + B_x^2} B_{N0}(t), \tag{5.4a}$$

$$B_{Nz} = \frac{B_z^2}{B_z^2 + B_x^2} B_{N0}(t). \tag{5.4b}$$

Here, $B_{N0}(t)$ is a scalar function of time representing the magnitude of the Overhauser field obtained under repumping conditions with a step-like switching of S_0 from $+|S_0|$ to $-|S_0|$. As follows from equation (5.7b), B_{N0} gives the value of the Overhauser field at $B_x = 0$. The temporal dependence of B_{N0} within a half-period is determined by the convolution of the step-like and the exponential decay functions

$$B_{N0}(t) = \mathcal{K}S_0\left(1 - \frac{2e^{-t/T_{\mathrm{repump}}}}{1 + e^{-T_{\mathrm{mod}}/(2T_{\mathrm{repump}})}}\right) + \mathcal{P}S_0^2, \tag{5.5}$$

where $\mathcal{K}$, $\mathcal{P}$, and T_{repump} are the fitting parameters.

Equation (5.6) is used to fit the Hanle curves shown in figure 5.4(c) with the following set of the fixed parameters: $S_z(0) = 0.06$, $B_z = +2$ mT and $B_{1/2} = 4$ mT, and a varied parameter $B_{N0}(t)$. From this fit, $B_{N0}(t)$ is obtained, which dynamics are shown by the symbols in figure 5.4(b). Fitting this dependence by equation (5.5) gives a characteristic time $T_{\text{repump}} = 425 \pm 50$ ms. The coefficient $\mathcal{K}S_0 = 31 \pm 3$ mT reflects the efficiency of the dynamic polarization of the nuclear spins inside the donor orbit. The time-independent contribution to B_{N0} given by $\mathcal{P}S_0^2 = 13 \pm 2$ mT results from the nuclear spin cooling in the oscillating Knight field [SPK+17, MZ12].

5.3 Nuclear spin cooling dynamics

To evaluate the nuclear spin dynamics of the localized electron and its influence on the Hanle effect, the experimental procedures mainly following to the ones described in chapter 5.2 and shown as an inset in figure 5.6(b) with alternating helicity of the pump every 500 ms was used.

The measurement of each Hanle curve was performed for σ^+ and σ^- excitation with averaging over full half-period, i.e., over 500 ms, for every external magnetic field value B_x varied from -25 to $+25$ mT and a set of fixed values of B_z field aligned along the direction of optical pumping. The colormap of the Hanle curves for different B_z and $f_{\text{mod}}\,(\sigma^+/\sigma^-) = 1$ Hz is mapped in figure 5.6(a). Each slice of figure 5.6(a) represents a Hanle curve. One can see that the curve width is different for the opposite B_z. Note, that the Hanle curve contains two small maxima sited symmetric concerning $B_x = 0$ only when $B_z > 0$. These additional maxima in the Hanle curve are caused by NSS cooling and appear due to either full or partial compensation of the external magnetic field by the Overhauser field [MZ12, SPK+17]. Thus, due to nuclear spin polarization, the influence of the external magnetic field on the electron spin is reduced, and the Hanle curves turn out to be symmetrical for $B_x = 0$. Figure 5.6(a) shows an example of the Hanle curves measured for opposite directions of B_z. It is evident that the Hanle curves are shown in figure 5.6(b) different in shape. For $B_z = +3$ mT, the curve contains two additional shoulders indicating the presence of the Overhauser field, B_N, and partial compensation of its transverse component by the external magnetic field B_x. On the contrary, when $B_z = -3$ mT experimental points approach the Lorentzian having width reduced comparing to the Hanle curve obtained at $B_z = 0$. In this case, the Overhauser field effectively adds to the external field when scanning B_x.

The observed difference in the magnitude of ρ_c at $B_x = 0$ mT and $B_z = 0$ mT [green curve in figure 5.6(b)] is caused by stabilization of the electron spin S_0 in the external longitudinal magnetic field B_z [MZ12] and due to the presence of a small magnetic field component in the superconducting coils inside the cryostat. The observed slight asymmetry (broadening for $B_x < 0$ mT and shrinkage for $B_x > 0$ mT) for curves demonstrated in figure 5.6 represents the oblique Hanle effect and may also be associated with inhomogeneity of the Overhauser field [MZ12]. Hereafter $B_z = +2$ mT is chosen to obtain the noticeable B_N. Note that, for efficient NSS cooling, the magnitude of B_z

should be higher than the so-called *mixing field*, which has the value of a few B_L where B_L is the local field of the dipole-dipole interaction in the NSS [VCS+18].

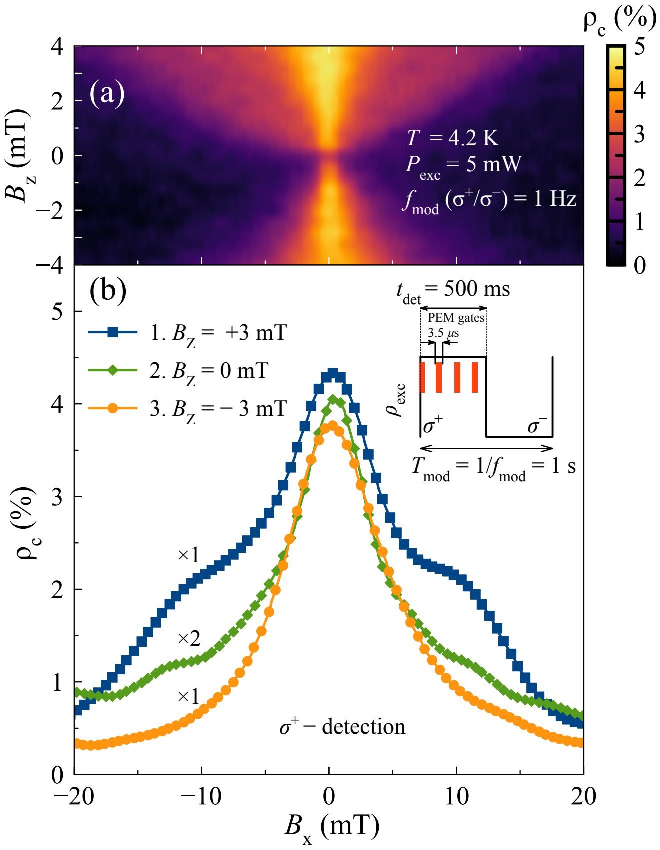

Figure 5.6: (a) Colormap of the PL circular polarization degree for different orientations and magnitudes of B_z measured for σ^+ excitation time at polarization modulation $f_{\text{mod}}(\sigma^+/\sigma^-) = 1$ Hz. (b) An example of the Hanle curves measured for σ^+ excitation time for opposite in direction B_z. [Note, that amplitude of the green curve in figure 5.6(b) was multiplied by two.]

Since a tilted geometry for an external magnetic field with $B_z = +2$ mT and $\rho_c \sim \langle S_z \rangle$ [MZ12] was used, it is necessary to take into account all components of B_N:

$$\begin{aligned} S_z(B) = S_{z\|} + S_{z\perp} = S_0 n_\| \frac{B^2_{\sum z}}{B^2_{\sum}} + S_0 n_\perp \frac{B^2_{\sum x}}{B^2_{\sum}} \frac{B^2_{1/2}}{B^2_{1/2} + B^2_{\Sigma}} = \\ = S_0 \left[n_\| \frac{(B_z + B_{Nz})^2}{B^2_{\Sigma}} + n_\perp \frac{(B_x + B_{Nx})^2}{B^2_{\Sigma}} \frac{B^2_{1/2}}{B^2_{1/2} + B^2_{\Sigma}} \right], \end{aligned} \tag{5.6}$$

where $n_{\parallel} = (1 + \tau/\tau_{s\parallel})^{-1}$, $n_{\perp} = (1 + \tau/\tau_{s\perp})^{-1}$ and $B_{\Sigma}^2 = (B_z + B_{Nz})^2 + (B_x + B_{Nx})^2$ is the total field acting on the electron spin and B_{Nx} and B_{Nz} are the Overhauser field projections.

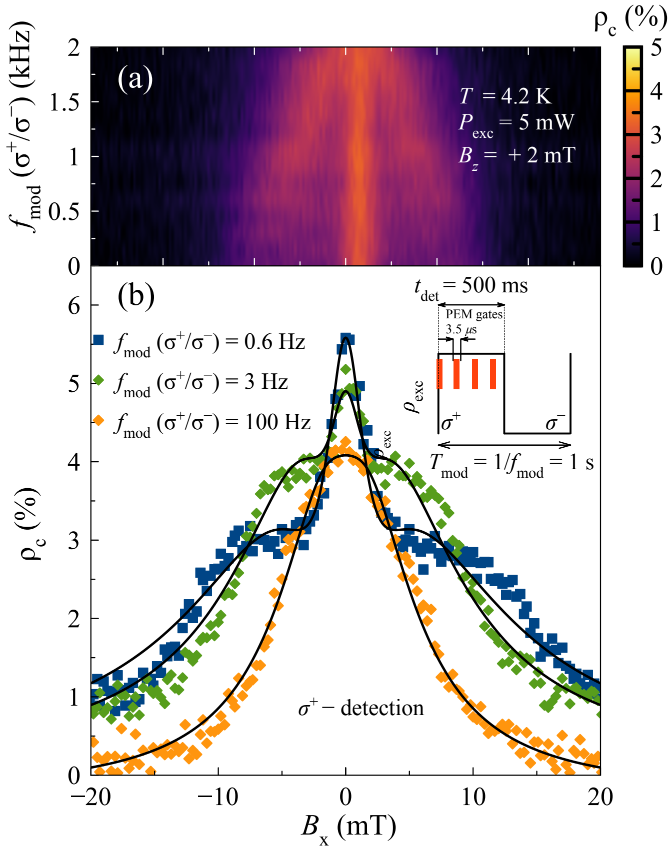

Figure 5.7: (a) Colormap of the PL circular polarization degree for different polarization modulation frequencies f_{mod} measured for σ^+ excitation time. (b) An example of the Hanle curves measured for different f_{mod} taken from the panel (a) of figure 5.7. Solid lines are fitting with equation 5.6.

Time dependencies of the $B_{Nx}(t)$ and $B_{Nz}(t)$ components during the measurement time T_{det} are neglected. Therefore, the Overhauser $\overline{B}_N$ is averaged over time and corresponds to the effective amplitude of the Overhauser field for the single Hanle curve. Thus, the parameter $\overline{B}_N$ corresponds to the Overhauser field magnitude under polarization modulation at $B_x = 0$ immediately after switching of polarization excitation ($\sigma^+ \rightarrow \sigma^-$ or $\sigma^- \rightarrow \sigma^+$). Then, the $\overline{B}_N$ projections on the axis of laboratory coordinates can be evaluated as

$$B_{Nx} = \frac{B_z B_x}{B_z^2 + B_x^2} \overline{B}_N, \tag{5.7a}$$

$$B_{Nz} = \frac{B_z^2}{B_z^2 + B_x^2} \overline{B}_N. \tag{5.7b}$$

In this way, fitting each Hanle curve with single scalar value of $\overline{B}_N$ allowing determining the Overhauser field magnitude as $B_N = \sqrt{B_{Nx}^2 + B_{Nz}^2}$ averaged over measurement time T_{det} under excitation polarization switching at f_{mod}. As follows from Eqs. (5.7a) and (5.7b), B_N gives the value of the Overhauser field developed over single half-period of modulation. As seen from figure 5.6(b), the Hanle dependencies can be properly fitted by equation (5.6) with B_{Nx} and B_{Nz} determined by Eqs. (5.7a) and (5.7b).

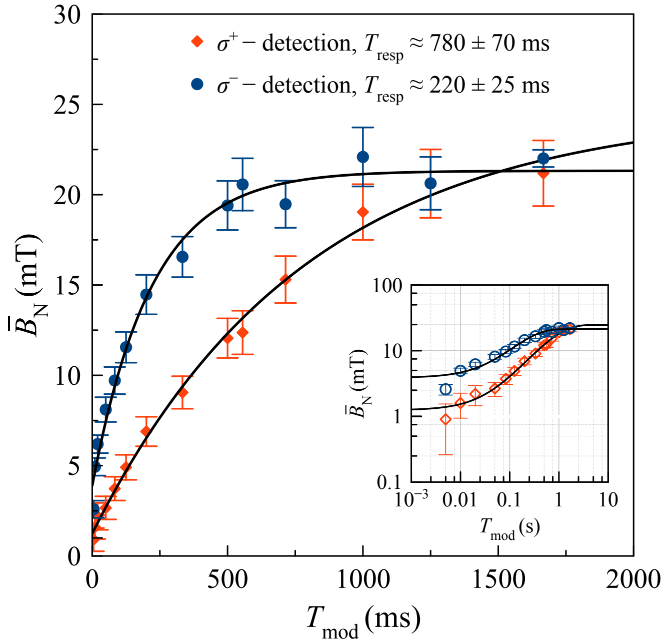

Figure 5.8: The dependence of $\overline{B}_N$ versus T_{mod}. The inset shows the double logarithmic scale of the data in figure 5.8. Solid lines are fitting with exponential functions.

To study the response dynamics of the donor-bound nuclei, the method of synchronous polarization modulation and detection of the Hanle curves [SPK+17, SPK+19] was used. The technique used is similar to the one shown in Fig. 5.6, but with the exception that polarization detection is now carried out in both half-periods of modulation (σ^+ and

σ^-) and f_{mod} is varied in the range from 0.6 Hz to 2 kHz. By choosing such a range of modulation frequencies, it is possible to achieve a significant nuclear spin polarization at a slow modulation of polarization. On the other hand, at higher modulation frequencies, it is expected that the Hanle curves should not be affected by the Overhauser field [MZ12]. Thereby, the nuclear spin response dynamics on polarization switching of the nuclei located inside the donor orbit [SPK+17] can be probed.

As an example, the the Hanle curves for different f_{mod} and fixed $B_z = +2$ mT are colormapped in figure 5.7(a). Each slice of figure 5.7(a) represents a Hanle curve for different f_{mod} for σ^+ excitation half-period. One can see the development of additional side peaks, which shift towards higher values of B_x with a decreasing of f_{mod}. A set of the Hanle curves obtained using the detection protocol described above is shown in figure 5.7(b).

Equation (5.6) is used to fit the Hanle curves shown in figure 5.7(b) with the following set of the fixed parameters: $B_z = +2$ mT, $B_{1/2} = 4$ mT and $S_0 = 0.25$, and the varied parameters $\overline{B}_N$, $n_\perp$ and $n_\parallel$. Figure 5.7(b) (solid lines) shows an example of the fitting with equation (5.6) for three different f_{mod}. From this fitting, $\overline{B}_N$ is obtained, which frequency dependencies for two different half-periods of modulation (σ^+ and σ^-) are shown in figure 5.8. One can see that $\overline{B}_N$ exponentially increases with increasing T_{mod}. In the fitting of experimental data, the values of $n_\perp$ and $n_\parallel$ are changed with the accuracy of up to 30%. The dependencies of $n_\perp$ and $n_\parallel$ on the frequency modulation are due to the field-dependent behavior of $\tau_\perp$ and $\tau_\parallel$ [Dya17]. The fitting value of $\overline{B}_N$ depends, first of all, on the width of the Hanle curve and position of additional shoulders [SPK+17] [as seen from Fig. 5.7(b)], and does not depend on S_0, $n_\perp$ and $n_\parallel$, thus, ensuring a reliable and unique fit of each experimental curve with the single value of $\overline{B}_N$.

As mentioned above, the appearance of the shoulders in the Hanle curves shown in figure 5.7(b) can be understood as a partial compensation of the external magnetic field by $\overline{B}_N$. In this case, the electron spin polarization is governed by the balance of the generation of spin-polarized electrons by circularly polarized light, S_0, and their depolarization caused by the Larmor precession in the total magnetic field $B_\sum = B + B_N$, as well as by the electron spin relaxation τ_s. The dependence of $\overline{B}_N$ on T_{mod} is shown in figure 5.8 for two different excitation half-periods (σ^+ and σ^-) with their fitting by saturating exponential functions. From this fitting, the characteristic response times T_{resp} are extracted. For σ^+ excitation half-period: $T_{\text{resp}} = 780 \pm 70$ ms, and for σ^- excitation $T_{\text{resp}} = 220 \pm 25$ ms are observed. Summarizing all of the above, the measured time T_{resp} characterizes the relaxation of nuclei inside the donor orbit, i.e., it provides an experimental estimate of the hyperfine relaxation time $T_{1\text{e}}$ under pumping [SPK+17].

The observed difference in the T_{resp} times could be understood as follows. The order of the magnitude of $T_{1\text{e}}$ due to interaction with electrons inside donors orbit can be estimated using the equation 5.1. The correlation time τ_c is determined by the spectral power density $b^2_{\text{ex}}(\omega)$ of fluctuating fields acting upon an electron spin due to its exchange interaction with its neighbors [AP58]. In the presence of a magnetic field, τ_c is determined by the spread of Larmor frequencies of the electron spins [BKYB17]:

$$\begin{aligned} \frac{1}{\tau_c} \approx \frac{(\langle g\rangle \mu_B)^2}{\hbar^2} \langle b_{\mathrm{ex}}^2(\omega)\rangle_g &= \frac{\langle J^2\rangle}{\hbar^2}\frac{\hbar}{\mu_B B_{\sum}}\int_{-\infty}^{\infty}\rho_g^2\frac{\hbar\omega}{\mu_B B_{\sum}}dg = \\ &= \frac{\langle J^2\rangle}{\hbar^2}\frac{\hbar}{\delta_g\mu_B B_{\sum}} = \frac{\hbar}{\tau_{c0}^2\delta_g\mu_B B_{\sum}}, \end{aligned} \tag{5.8}$$

where ρ_g is the distribution function of the electron g factors, $\delta_g = (\int_{-\infty}^{\infty}\rho_g^2(g)dg)^{-1}$, $\langle J^2\rangle$ is the mean squared exchange constant and $\tau_{c0} = \hbar/\sqrt{\langle J^2\rangle}$ is the correlation time at zero magnetic field and temperature. Equation (5.8) is derived for the range of magnetic fields $B_{\sum} > 1/\delta_g\tau_s$ when transverse relaxation of electron spins is determined by the g factor spread. One can suggest an approximate expression for τ_c: $\tau_c \approx \sqrt{B_{\sum}^2 + B_s^2}(\tau_{c0}^2\delta_g\mu_B)/\hbar$ where $B_s = 1/\delta_g\tau_s$. Taking $B_N \approx \pm 20$ mT, one can obtain a rough estimate of $B_s \approx 10$ mT, which is a reasonable agreement with the data of Ref. [BKYB17], obtained for n-GaAs with similar donor concentration. Since the magnitude of the total magnetic field $B_{\sum} = B \pm B_N$ acting on the electron spin depends on the excitation polarization helicity, thus, τ_c is longer and T_{resp} is shorter for σ^- excitation when the Overhauser field B_N develops in the same direction as external magnetic field B [see Fig. 5.8].

5.4 Estimations of the nuclear spin temperature

The nuclear spin temperature concept [OL97] can also describe the behavior of the NSS dynamics. For experimental conditions used in this work, where $B \gg B_L$ (where $B_L \approx 0.2$ mT is the local field for GaAs [MZ12]), the spin temperature characterizes the Boltzmann distribution of the nuclear spin populations between equidistant Zeeman energy levels. The expression for the nuclear spin polarization in the high-temperature approximation [Dya17] is

$$P_N = \frac{\langle I\rangle}{I} = \frac{B}{3k_B\Theta_N}\hbar\langle\gamma_N\,(I+1)\rangle, \tag{5.9}$$

where k_B is the Boltzmann constant, Θ_N is the nuclear spin temperature and γ_N is the nuclear gyromagnetic ratio. Here, I is the nuclear spin, the angular brackets denote averaging over all nuclear species in GaAs [HBDM+01]: ^{69}Ga, ^{71}Ga and ^{75}As.

The Overhauser field acting upon electron spins

$$B_N = b_N\frac{\langle I\rangle}{I}, \tag{5.10}$$

where b_N is the maximum value of the Overhauser field corresponding to complete polarization of all nuclei, for GaAs, $b_N = 5.3$ T [MZ12]. Combining Eqs. (5.7a), (5.7b), (5.9), and (5.10), the expression for the nuclear spin temperature [MZ12] dependent on B_N calculated in figure 5.8 reads as

$$\Theta_N = \frac{b_N B\hbar\langle\gamma_N\,(I+1)\rangle}{3k_B B_N}, \tag{5.11}$$

where $B = \sqrt{B_x^2 + B_z^2}$ is the external magnetic field.

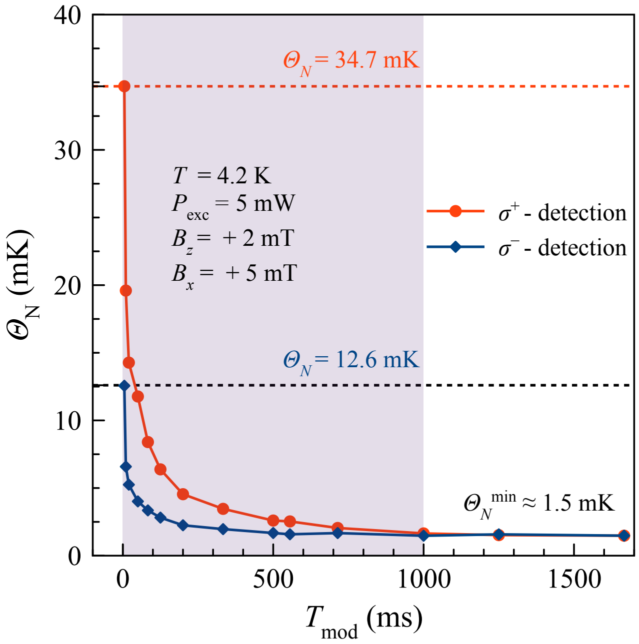

Figure 5.9: Magnitude of the nuclear spin temperature Θ_N, calculated from the data in figure 5.8 with equation (5.11). The filled area defines the range of modulation frequencies $T_{\text{mod}} \leq 10^3$ ms, where the nuclear spin temperature Θ_N generally decreases.

Figure 5.9(a) shows the calculated Θ_N with equation (5.11) for different T_{mod} at the compensation point of external magnetic field $B_x = 5$ mT by the Overhauser field B_N [Eqs. 5.7a and 5.7b]. One can see that during fast modulation with $T_{\text{mod}} = 5$ ms, the Θ_N values differ almost three times in magnitude 34.7 mK for σ^+- detection and 12.6 mK for σ^--detection. This difference is due to the mutual orientation of the mean electron spin $\langle S_z \rangle$ and B_N, which grows in the direction along with B_z or opposite to it. In the case when $S_0 \uparrow\uparrow B_z$ realized for σ^+ polarization a better initial cooling and lower spin temperatures Θ_N are observed. The cooling of the NSS occurs already when $T_{\text{mod}} \sim 1$ s and the nuclear spin temperature approaches the steady-state value of $\Theta_N \approx 1.5$ mK and remains constant for both of different half-periods of modulation in the region where $T_{\text{mod}} > 1$ s. This stability of Θ_N for higher f_{mod} is due to its primary dependence on the magnitude of the external magnetic field and total NSS pumping efficiency.

5.5 Nuclear spin relaxation "in the dark"

For detailed study of the nuclear spin relaxation mediated by the hyperfine interaction with donor bound electrons in the absence of illumination, the experimental setup described in section 3.2.4 was used. During the dark and bright time intervals, the external magnetic fields $B_z = +2$ mT and $B_x = +5$ mT are applied. The PL kinetics is analyzed using a multi-channel photon-counting system (see section 3.2.4). The protocol consists of two alternating time intervals: the bright interval $t_{\text{pump}} = 500$ ms is followed by a dark time of various duration (from $t_{\text{dark}} = 10$ ms to $t_{\text{dark}} = 1.3$ s).

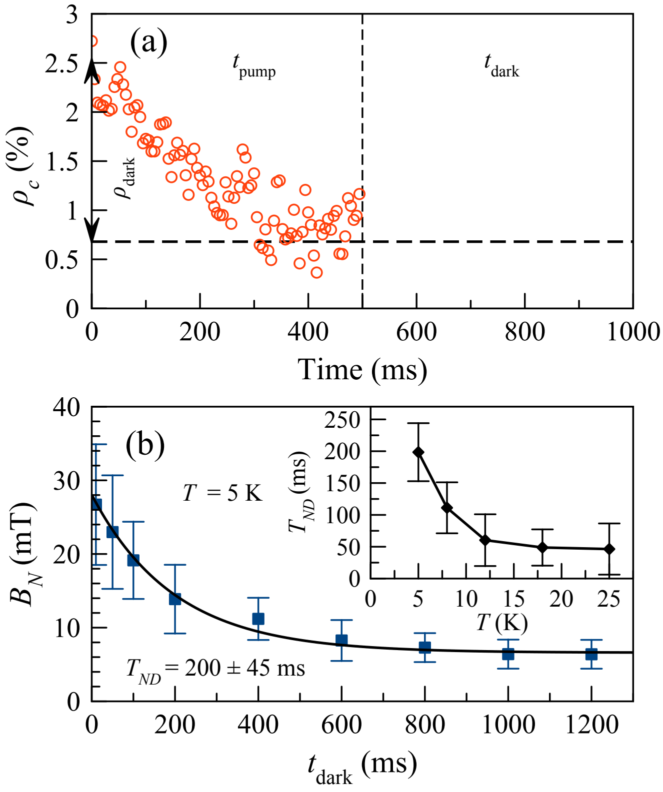

Figure 5.10: (a) Time dependence of the ρ_c for the presence of circularly polarized pump. (b) The Overhauser field values calculated for different dark time intervals using equation 5.12 (squares) and its fitting with an exponential decay function (solid line). Inset shows the temperature dependence of the nuclear spin relaxation time.

After measurement in co-circular and cross-circular polarizations of the PL detection, the ρ_c dynamics is evaluated [see Fig. 5.10(a)]. Note, that the value of the the electron spin polarization degree immediately after the dark interval, $\rho_{\text{dark}} = \rho_c(t = 0)$ was used.

The Overhauser field immediately after the dark interval can be calculated from the PL polarization degree [KDV+16]

$$B_N = B_{1/2}\sqrt{\frac{\rho_0 - \rho_{\text{dark}}}{\rho_{\text{dark}} - \rho_0 \sin^2\theta}} - \sqrt{B_x^2 + B_z^2}, \tag{5.12}$$

where ρ_0 and $B_{1/2}$ are obtained in the absence of nuclear spin polarization [see Fig. 5.1(b)], and $\theta \approx 12^\circ$ is the angle between the external magnetic field and x axis.

Figure 5.10(b) shows an example of the evolution of B_N calculated using equation (5.12) for different t_{dark}. Fitting these values by an exponential decay function gives the spin relaxation time in the dark due to interaction with electrons, $T_{ND} = 200 \pm 50$ ms. This time is shorter than T_{bulk} shown in figure 5.2(b) by three orders of magnitude and can be compared with T_{repump} measured at step-like polarization modulation. As an initial conclusion, the measured times T_{repump} and T_{ND} characterize the relaxation of nuclei under the donor orbit, i.e., they provide an experimental estimate of the hyperfine relaxation time T_{1e} under pumping and in the dark, respectively. Treating T_{repump} as time characterizing the hyperfine relaxation of nuclei inside the donor orbit in the presence of optical excitation and comparing with the results of Paget [Pag82], the estimate of the correlation time of the donor-bound electron is equal to $\tau_c \approx 200$–300 ps. These values agree well both with the data of Ref. [DKK+02] and Ref. [SPK+17], where τ_c was determined from polarization recovery under optical pumping in longitudinal magnetic fields.

On the other hand, the time T_{ND} at low temperature is two times shorter and corresponds to the electron correlation time of about 500 ps. This difference is not crucial as compared to that between the spin relaxation times of donor-associated and bulk nuclei. This effect can be explained by a shortening of τ_c due to the exchange interaction with itinerant photoexcited electrons [Pag81]. As discussed in the chapter 1, this mechanism was invoked in Ref. [Pag82] to explain the short electron correlation time found in high-purity GaAs. The result presented in the current chapter confirms the model of nuclear spin relaxation proposed in Ref. [Pag82] and expands it to moderately n-doped semiconductors.

The effect of another kind connected with the pumping of the nuclear spin relaxation, discussed in Ref. [PAK08]. It can be explained by taking into account the modulation of the quadrupole splitting of nuclear spins by electric fields induced by charge fluctuations at the donor center. These fluctuations may result from the recombination of donor-bound electrons with photoexcited holes and subsequent trapping of photoexcited electrons at the donor center that has been emptied by recombination. Obviously, if this mechanism work, nuclear relaxation under pumping would have been faster than in the dark. The last prediction contradicts the behavior observed in the experiment of the current thesis.

Nevertheless, it can be concluded that within the range of pumping levels of this chapter, donor perturbation induced by the pump is not enough to induce noticeable nuclear spin relaxation. This mechanism sheds light on the observed shortening of T_{ND} with temperature increase [see inset to Fig. 5.10(b)]. For elevated temperatures $T > 4$ K, the donor filling factor decreases due to thermal activation of electrons to the conduction band, giving rise to charge fluctuations. It should also be made clear that the obtained experimental data so far are insufficient and incomplete to conclude whether the observed effect is due to this specific physical mechanism and it leaves this question open for future investigations.

5.6 Conclusions

To conclude this chapter, the nuclear spin dynamics has been experimentally studied in n-GaAs with donor concentration $n_D = 4 \times 10^{15}$ cm^{-3} by measuring the Hanle effect with millisecond time resolution under time-varying optical pumping. Two timescales of nuclear build-up and relaxation have been observed. One of them is slow (on the order of hundreds of seconds) relaxation of bulk nuclei via spin diffusion from (build-up) or to (relaxation) donor centers. The measured characteristic time $T_{\text{bulk}} \approx 10^2$ s is typical for the dielectric phase of n-GaAs with the studied donor concentration [VCS+17].

At the same time, a faster dynamics is observed on the timescale from 200 to 780 ms, which is attributed to the spin dynamics of nuclei inside the donor orbit. It has also been shown that the subsecond relaxation time of nuclear spin near donors is faster in the dark than in the presence of optical pumping. As suggested, this effect can be explained by taking into account the exchange scattering of photoexcited itinerant electrons at donors, which shortens the spin correlation time of donor-bound electrons and slows down the hyperfine relaxation.

The effect of the threefold increase of T_{resp} for σ^+ excitation is connected with stabilizing action of the longitudinal field B_z. Thus, the cooling of the NSS to several millikelvin $\Theta_N \approx 1.5$ mK is possible at relatively fast modulation of excitation polarization $T_{\text{mod}} = 1$ s. The method described in this chapter allows one to select a proper range of the light polarization modulation frequencies and magnitudes of the external magnetic fields to achieve the cooling of the NSS to the desired spin temperature.

6 Spin-lattice relaxation of optically polarized nuclei in p-type GaAs

Adapted from Phys. Rev. B **97**, 165206 (2018).

In this chapter, the measurements of nuclear spin-lattice relaxation time T_1 as a function of magnetic field and temperature in two insulating p-GaAs layers with different concentrations of acceptors are presented. The measured nuclear spin-lattice relaxation times are of the order of 100 ms and found to be independent of magnetic fields in the range of 0–100 G and demonstrate a slow increase with lowering the temperature in the range of 10–30 K, which unexpectedly becomes sharp below 10 K. This behavior is drastically different from that known for the nuclear spin relaxation in n-GaAs. The fact that nuclear spin relaxation in the dark, i.e., in the absence of photoexcited conduction-band electrons, is three orders of magnitude shorter than in n-GaAs, where resident electrons are abundant, is counterintuitive since hyperfine coupling in the valence band is weaker than in the conduction band. The theoretical model that qualitatively explains the whole set of the experimental data for p-GaAs was proposed. This model allows a quantitative recovery of the measured temperature dependence of the nuclear spin relaxation time T_1.

6.1 The investigated samples

The studied samples are two germanium-doped GaAs layers grown by liquid phase epitaxy on a GaAs substrate. The corresponding acceptor concentrations are $n_A = 2.6 \times 10^{16}$ cm^{-3} (sample A) and $n_A = 6 \times 10^{16}$ cm^{-3} (sample B). The samples are placed in a variable temperature cryostat (either helium flow or cold finger) [see section 3.1.1], surrounded by three pairs of Helmholtz coils. Such an arrangement allows for the compensation of laboratory magnetic fields and the application of a desired external magnetic field in an arbitrary direction. The spectra of PL intensity and its circular polarization degree ρ measured for two samples are shown in figure 6.1. The PL peaks can be identified as acceptor-bound exciton (ABX) emission and conduction band-to-acceptor (CBA) recombination. Figures 6.2(a) and 6.2(b) represents the PL polarization degree as a function of the magnetic field B applied at 80° relative to the growth axis, for samples A and B for a different sign of the excitation helicity. For studies of transient nuclear spin polarization P_N the experimental setup described in section 3.2.4 was used.

The three-stage experimental protocol implemented here is very similar to that used in works on n-GaAs [KDV+16, VCS+17, SPK+19]. The experimental protocol is shown in figure 5.10(a) in section 5.5. The first stage of the experiment is the optical pumping of nuclei by circularly (σ^+) polarized light with a wavelength of $\lambda = 800$ nm during 500 ms. The excitation power is $P_{\rm exc} = 4$ mW, focused on 90 μm^2 spot on the sample surface. The magnetic field $B_{\rm pump} = 4$ G is applied at 80° relative to the structure axis. At the second stage, the pump is switched off for an arbitrary time $t_{\rm dark}$ (typically from 2 ms to 1 s), and the magnetic field is set to the value $B_{\rm dark}$ at which the nuclear spin dynamics can be measured. $B_{\rm dark}$ is parallel to $B_{\rm pump}$ and ranges from 0 to 120 G. The switching time is about 1 ms for $B < 10$ G and increases to approximately 10 ms for $B > 10$ G. At the end of the dark interval $B_{\rm pump}$ is restored and the pump is switched on. At the same moment, the photon-counting system starts the PL detection in either right or left circular polarization. The PL signal was measured during 500 ms, which is sufficient to fully restore NSS polarization reply to the pumping. At the end of this stage, the cycle is repeated and averaged over 100 measurement cycles. The same procedure is performed for the opposite polarization of PL. From each pair of measurements, the degree of circular polarization of PL is evaluated, and plotted as a function of the photon-counting time $t_{\rm PCS}$.

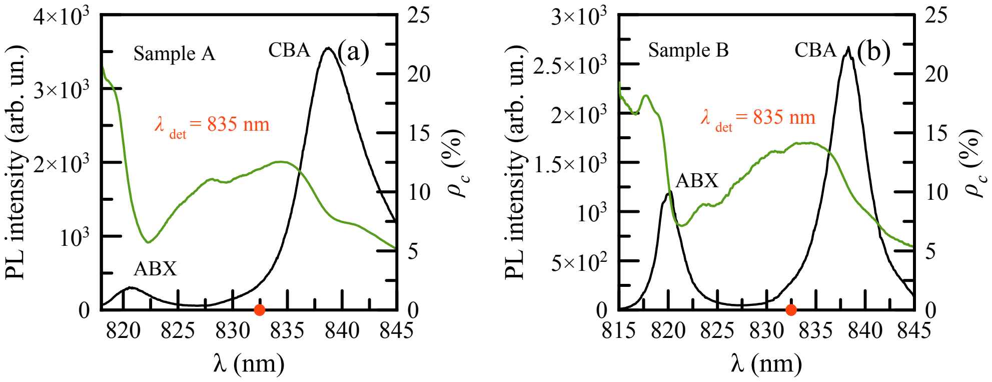

Figure 6.1: Polarization (right scale) and PL intensity (left scale) spectra for p-GaAs, Samples A (a) and B (b) at $B = 0$ and $T = 5$ K. The two PL peaks are identified as acceptor-bound exciton (ABX) emission and conduction band-to-acceptor (CBA) recombination. The red dots indicate the chosen PL detection wavelength.

During dark intervals, the nuclear polarization decreases, which results in a larger value of ρ measured when the pump is switched on again. Fitting $\rho(t_{\rm PCS})$ by exponential decay function gives the buildup time of the Overhauser field under optical pumping T_{NB}, as well as the value of $\rho_{\rm dark}$. The fitting procedure used reduces the influence of the probe light on the nuclei during measurement and allows a more precise determination of $\rho_{\rm dark}$ and nuclear field value [KDV$^+$16]. In the next step, the Overhauser field can be recovered from the PL polarization degree using the equation 5.12.

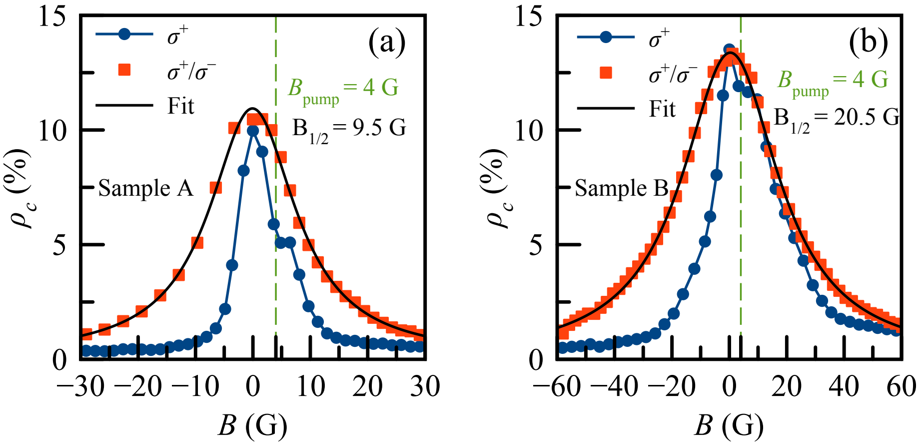

Figure 6.2: (a), (b) PL polarization as a function of oblique magnetic field in samples A and B. Pump polarization is either alternated by a photoelastic modulator at the frequency of 50 kHz (effect of the Overhauser field is reduced, red symbols), or fixed (blue symbols). The onset of the Overhauser field results in the asymmetry with respect to zero. Solid black lines are Lorentzian fits to the data, that allow for determination of $B_{1/2}$ and ρ_0.

It should be noted that even after the shortest dark intervals, B_N is a bit lower than before switching off the pump. It is assumed that this is due to the nuclear spin warm up by the Knight field of photoexcited electrons which is rapidly changes when the pump is switched off and on [SPK+17]. By repeating the protocol for different durations of t_{dark}, the values of B_N relaxation curves can be evaluated for given values of temperature and applied magnetic field B_{dark}.

6.2 Nuclear spin-lattice relaxation times

Examples of such dependencies for two different temperatures are shown in figure 6.3. One can see that B_N decreases with the increasing duration of the dark interval of t_{dark}. Exponential fitting of these curves (for details see section 5.5) yields the nuclear spin relaxation time in the dark, T_1. The next step will be to study T_1 dependence as a function of temperature and applied external magnetic field B_{dark}.

Magnetic-field dependence of nuclear spin relaxation time T_1 measured in sample B at $T = 10$ K is shown in figure 6.4. For comparison, the relaxation time in dielectric n-GaAs sample (from Refs. [KDV+16, VCS+17]) is shown on the same figure. One can see that in p-GaAs, nuclear spin relaxation is about three orders of magnitude faster than in n-GaAs. Furthermore, in n-GaAs, the relaxation time exhibits a magnetic field dependence, while in p-GaAs, it does not depend on the external magnetic field in the measured range.

The temperature dependence of T_1 is also untypical. Figure 6.5 shows spin relaxation time measured in samples A and B, as well as the comparison with n-GaAs sample from Refs. [KDV$^+$16, VCS$^+$17]. It turns out that in p-GaAs nuclear spin relaxation slows down significantly below $T = 10$ K. For example, in sample B, $T_1 = 45$ ms at $T = 30$ K and 310 ms at 4 K. This behavior has not been detected previously for p-GaAs. In order to understand and describe this data, a possible mechanism of nuclear spin-lattice relaxation in p-GaAs may be taken into account, similar to studies of n-GaAs.

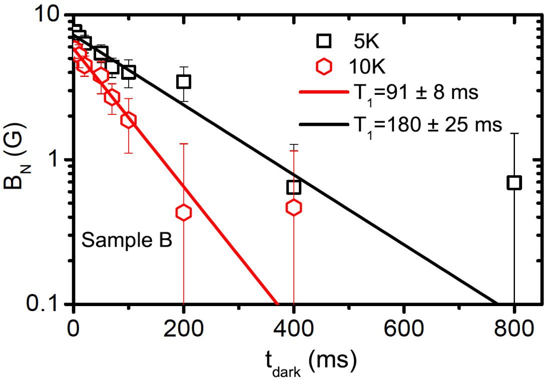

Figure 6.3: Overhauser field B_N derived using Eq. (5.12) from PL polarization measurements for various dark interval durations ($B = B_{\text{dark}} = 4$ G). The exponential decay fit (solid lines) yields T_1 for given temperatures [KDV$^+$18].

The spin-lattice relaxation of nuclei in n-GaAs is three orders of magnitude shorter comparing to p-GaAs. This observation excludes the diffusion-limited hyperfine relaxation [VCS$^+$17, Pag82] from possible relaxation mechanisms taking into account that the nuclear spin diffusion constant $D \approx 10^{-13}$ cm^2/s, the diffusion length during the time 100 ms is ≈ 1 nm (or two lattice constants of GaAs [Pag82]. This means that the nuclear spin polarization during this time cannot reach any remote center (e.g., paramagnetic impurity or neutral acceptor site) by diffusion, and participating in the decay within the same area where it has been created. Thus, the spin diffusion mechanism that controls nuclear spin relaxation in n-GaAs [VCS$^+$17, Pag82] can not help for fast nuclear spin relaxation in p-GaAs. Thus, it leaves two possible mechanisms for nuclear spin relaxation in p-GaAs: (i) when nuclear spins are polarized only in regions where some efficient relaxation mechanism is at work, or (ii), a new and unknown relaxation mechanism is acting everywhere in the crystal.

First, the second mechanism will be examined. Since the only long-range relaxation mechanism known for the dielectric GaAs at low temperatures is the quadrupole relaxation due to fluctuating electric charge. The reason for these fields is the hopping of localized charge carriers in the impurity band, but this mechanism is far too weak to explain the observed relaxation timescale. Indeed, the calculations reported in Ref. [KDV+16] shows that one cannot expect the relaxation times shorter than 20 s induced by this mechanism. This conclusion is supported by the experiments on n-GaAs where it was shown that the efficiency of quadrupole relaxation of bulk nuclei drops down in magnetic fields exceeding the nuclear spin local field of the order of a few Gauss [KDV+16]. On the other hand, in the studied p-GaAs samples no magnetic-field dependence of T_1 is observed at least up to 120 G (see figure 6.4).

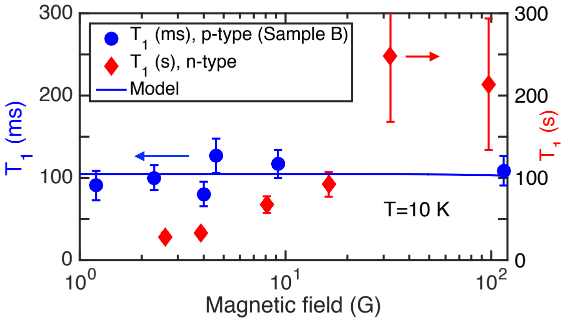

Figure 6.4: Magnetic-field dependence of nuclear spin relaxation time [KDV+18]. Sample B (circles, left scale) and n-GaAs with $n_D = 6 \times 10^{15}$ cm^{-3} (diamonds, right scale, data from Ref. [VCS+17]).

Analyzing the first scenario, it should be mentioned that the efficiency of the dynamic polarization of nuclear spins by free photoexcited electrons is very low. Nuclear spins are polarized by electrons trapped to donor centers, which in p-type crystals are empty in the absence of optical pumping. Under continuous optical excitation, the nuclear polarization can spread out from the vicinity of donors into the bulk of the crystal by spin diffusion (for example in n-type crystals). This is demonstrated in figure 6.6(b), where a sketch of the spatial distribution of the nuclear spin polarization in n-GaAs is shown. After sufficiently long pumping time, nuclear spins are not only polarized within the donor orbits but also everywhere in bulk, due to nuclear spin diffusion. The relaxation of this polarization in the dark occurs towards neutral donors D^0. At low magnetic fields, this relaxation is present directly in the bulk of the crystal via interaction of the nuclear quadrupole moments with the fluctuating electric field of hopping charges.

For p-type GaAs, the situation is different: the optical polarization of nuclear spins by photocarriers is very inefficient, nuclear pumping in p-GaAs is only possible in the vicinity of shallow donors. This is confirmed by the fact [PAK08] that in p-doped III-V semiconductors under optical pumping the nuclear polarization accumulates near donors sites only within the so-called "quadrupole radius" δ [see figure 6.6(a)] and it is determined by a competition between hyperfine polarization and quadrupole relaxation of nuclei. The reason for this is as follows. Dynamic polarization of nuclear spins occurs due to their hyperfine coupling with the electron spins captured by donors at the rate proportional to the electron spin density which falls exponentially with increasing the distance from the donor position. Since all photoexcited electrons spend some time at the donor position before recombination, the donor periodically changes its charge state from positively charged to neutral. This is called the "blinking charge" and creates a time-dependent electric field, which, obeying the Coulomb law, spreads far beyond the Bohr radius of the donor-bound electron a_{BD}. It is known that in piezoelectric semiconductors like GaAs, the electric field induces quadrupole splitting of nuclear spin states [BMMP63]; fluctuating electric fields thus act similarly to fluctuating magnetic fields, causing nuclear spin relaxation. At some distance from the donor center, quadrupole relaxation takes precedence over the dynamic polarization because the electric field decreases with growing distance slower than the electron density. According to the calculations reported in Ref. [PAK08], this effect takes place already at $\approx 0.4 a_{BD}$. The numerically calculated nuclear spin polarization versus distance from the donor is shown in figure 6.7. It should be noted that the presence of an additional relaxation channel under pumping is supported by the observed data for both p-GaAs samples. The buildup time of the nuclear polarization is even shorter than its decay time in the dark, about 50 ms.

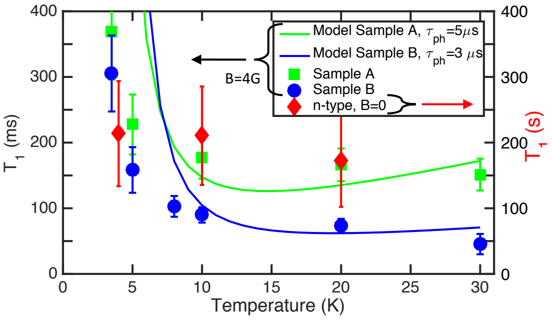

Figure 6.5: Temperature dependence of nuclear spin relaxation time [KDV+18]. In p-GaAs (left scale): sample B (circles), sample A (squares); in lightly doped n-GaAs (right scale: diamonds, data from Ref. [VCS+17]).

Therefore, the nuclear spin polarization induced by optical pumping in p-GaAs is demonstrated in figure 6.6(a). The following question may be raised: what relaxation mechanism can be responsible for this fast decay in the absence of the excitation and with an empty donor? The very first and obvious idea that it is the quadrupole relaxation induced by the electric field of a charged acceptor located in the vicinity of the donor. The presence of charged acceptors may be the result of the recombination of one of the acceptor-bound holes with the donor electron. At low temperature, the negative charge corresponding to the absence of a hole is located at the acceptor nearest to the positively charged donor with a 97.4% probability.

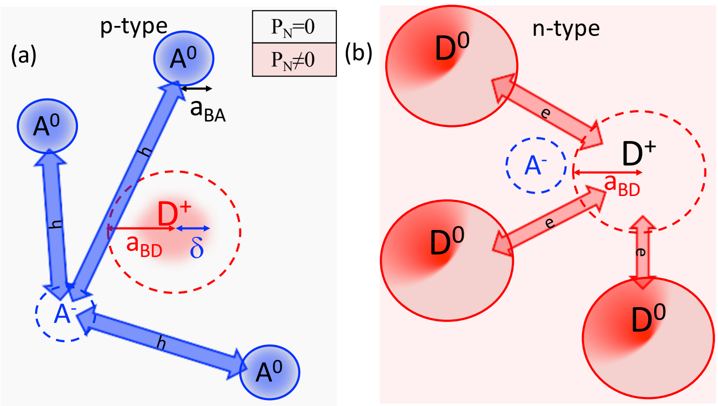

Figure 6.6: Sketch of nuclear spin polarization patterns that form as a result of optical pumping in p-GaAs (a) and n-GaAs (b) [KDV+18]. The degree of nuclear spin polarization P_N is schematically represented by the red color intensity. In n-GaAs, most of the donors are neutral; P_N created under orbits of donor-bound electrons spreads into the interdonor space so then $P_N \neq 0$ everywhere under the light spot. The relaxation of this polarization in the dark is provided by (i) diffusion towards neutral donors D^0, and (ii) directly in the interdonor space via interaction of the nuclear quadrupole moments with the fluctuating electric field of hopping electrons (between D^0 and D^+). In p-GaAs, all donors are charged; $P_N \neq 0$ only near donors because of its quadrupole relaxation during pumping. Almost every donor has an acceptor nearby, and the electric charge of this acceptor fluctuates while it captures and releases a hole. This induces quadrupole relaxation which is much faster in p-GaAs than in n-GaAs.

The distribution function of the distances from the donor to the nearest acceptor is shown in figure 6.7. It has the maximum at $R_{DA}^{(1)} = (2\pi n_A)^{-1/3}$. For the studied range of n_A, this is approximately $1.5a_{BD}$. At this distance, a charged acceptor produces an electric field E of several kV/cm at the donor site and so far as GaAs is a polar crystal, this electric field induces an effective quadrupole field:

$$B_Q = b_Q E, \tag{6.1}$$

with

$$b_Q = \frac{eQ\beta_Q}{4\gamma_N I(2I-1)}, \tag{6.2}$$

where β_Q is the experimentally determined and isotope-dependent constant, eQ is the nuclear quadrupole moment, e is the electron charge, γ_N is the nuclear gyromagnetic ratio, I is the numerical value of the nuclear spin [PAK08, BMMP63]. Here, B_Q depends on the mutual orientation of the electric field and nuclear magnetic moments at the low magnetic fields and taking into account the averaging over spherical distribution (see Eq. 6.1). Figure 6.7(b) shows the effective quadrupole field as a function of the distance from the charged and neutral acceptor. It is seen that at the distance $R_{DA}^{(1)}$ from the A^- acceptor $B_Q \approx 1$ G. In case when $T \neq 0$, a hole from a remote and neutral acceptor can jump to this site, thereby neutralizing it. Thus, fluctuations of the occupation number of the nearest acceptor produce fluctuating quadrupole fields. In section 6.3, it is shown that these fluctuations provide an efficient nuclear spin relaxation.

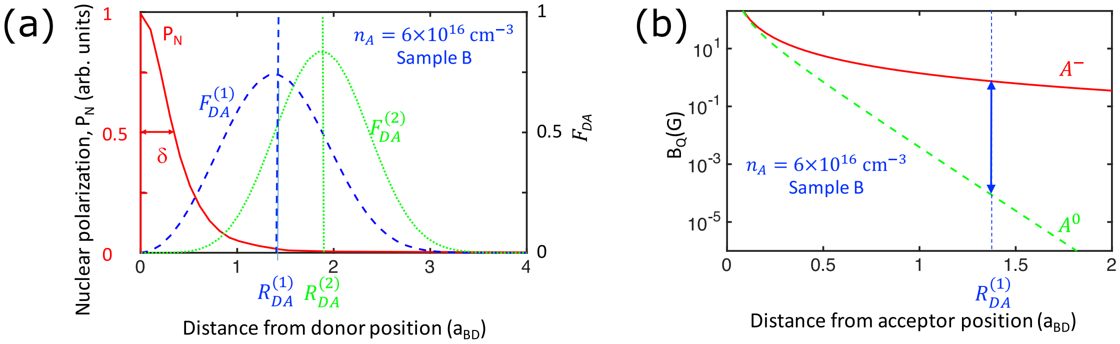

Figure 6.7: (a) Left scale: the nuclear spin polarization created by optical pumping as a function of the distance from the donor [PAK08]. Right scale: probability density for the first (blue dashed line) and second (green dotted line) neighboring acceptors calculated from Eq. 6.15 for sample B as a function of the distance from the donor. The distance is expressed in the units of donor Bohr radius $a_{BD} = 10$ nm. (b) Effective quadrupole field B_Q in the vicinity of the charged (red solid line) and neutral (green dashed line) acceptor. It is plotted as a function of the distance from the acceptor position. The distance is expressed in the units of donor Bohr radius $a_{BD} = 10$ nm. Blue arrow shows that at the distance $R_{DA}^{(1)}$ corresponding to the maximum probability to find the nearest donor (cf. figure 6.7(a)), the charged acceptor A^+ creates $B_Q \approx 1$ G, while B_Q in the vicinity of A^0 is negligibly small [KDV+18].

Figure 6.6 illustrates the above considerations via comparison of the nuclear spin polarization schemes in p-GaAs and n-GaAs. Within n-type GaAs crystal volume, most of the donors are neutral and the nuclear spin polarization created under orbits of donor-bound electrons travels into the interdonor space. In this particular case, the number of charged donor-acceptor pairs is small, and most of the nuclei are situated far from these pairs. In contrast, in p-GaAs, all the donors are electrically charged and the nuclear spin polarization is mainly present near donor sites because of quadrupole relaxation during pumping [PAK08]. Almost every donor has an acceptor nearby, and the electric charge of this acceptor fluctuates while it captures and releases a hole. It sheds light on the fact that spin relaxation induced by fluctuating charges is three orders of magnitude faster in p-GaAs as compared to n-GaAs. This model also explains the T_1 behavior as a function of temperature and magnetic field in p-GaAs. Indeed, with lower temperatures, the time during which the nearest acceptor site is charged, is increased since this state is energetically favorable. As a result, the charge distribution in the vicinity of the donor becomes frozen, and the electric field stops fluctuating. This obviously should lead to an increase of T_1, and this is precisely what is observed in experiments (see figure 6.5) [KDV$^+$18].

The T_1 independence of the applied magnetic field B can be interpreted as that $\omega_B \tau_c \ll 1$, where $\omega_B = \gamma_N B$ is the nuclear Larmor frequency in the field B and τ_c is the correlation time of the fluctuating field which causes the spin relaxation [Dya17]. For nuclear species of GaAs, the average nuclear gyromagnetic ratio $\langle \gamma_N \rangle \approx 9 \times 10^3$ rad/Gs. Using equation 5.1 it is possible to calculate the correlation time which fits the observed $T_1 \approx 100$ ms (see figure 6.4). Assuming the magnitude of the fluctuating quadrupole field of ~ 1 G [see figure 6.7(b)], the $\tau_c \approx 100$ ns. Summing up all of the above in this section, throughout the range of magnetic fields applied in our experiment, the condition $\omega_B \tau_C \ll 1$ is fully satisfied, which is not contradictory with T_1 independence of the applied external magnetic field.

6.3 Quadrupole charge fluctuation

In this chapter, the theoretical model which quantifies the above considerations will be presented.

First, the assumption is being made that the fluctuations of the electric field under the donor orbit result from the charge fluctuations on the nearest acceptor, as shown in figure 6.6. When the acceptor is negatively charged, it creates an electric field E_- in the vicinity of the donor [neglecting of the spherical (with the radius equal to δ) spatial variation of this field, where nuclear spins are polarized]. In the case when the nearest acceptor is neutral, the electric field takes a particular value E_0, and only remote impurities experience the change in charge density. Correspondingly, the average electric field at the donor is equal to

$$\langle E \rangle = \frac{E_- \tau_- + E_0 \tau_0}{\tau_- + \tau_0}, \tag{6.3}$$

where τ_- is the average time during which the nearest acceptor stays charged and τ_0 is the average time during which it is neutral. The mean-squared fluctuation of this field is

$$\delta E^2 = \langle (E - \langle E \rangle)^2 \rangle = \Delta E^2 \frac{\tau_- \tau_0}{(\tau_- + \tau_0)^2}, \tag{6.4}$$

where $\Delta E^2 = (E_- - E_0)^2$. The autocorrelation function of the fluctuating part of the electric field $E_f = E - \langle E \rangle$, which is, basically, an example of an asymmetric random telegraph signal, is determined by the shortest of the two times τ_- and τ_0:

$$\langle E(t) \cdot E(0) \rangle = \delta E^2 \exp \left[-t \left(\frac{\tau_- + \tau_0}{\tau_- \tau_0} \right) \right]. \tag{6.5}$$

On the other hand, the correlation time of the electric field fluctuations is equal to

$$\tau_c = \frac{\tau_- \tau_0}{\tau_- + \tau_0}. \tag{6.6}$$

The Fourier transform of the autocorrelation function in Eq. (6.5) allows calculating the spectral power density of electric field fluctuations at the donor site:

$$\delta E_\omega^2 = \frac{\delta E^2 \tau_c}{1 + \omega^2 (\tau_- \tau_0)^2 / (\tau_- + \tau_0)^2}. \tag{6.7}$$

Thus, the resulting spectral power density of the quadrupole-induced effective magnetic field is calculated as

$$\delta B_\omega^2 = b_Q^2 \delta E_\omega^2. \tag{6.8}$$

Following Abragam's theory [Abr61], the spin relaxation rate of the NSS in presence of the fluctuating magnetic field reads as

$$T_1^{-1} = \gamma_N^2 \delta B_\omega^2 \tau_c, \tag{6.9}$$

where $\omega = \omega_B$ and ω_B is the Larmor frequency of nuclear spin in the external field B. At low magnetic fields used in this chapter and satisfying the condition $\omega_B \tau_c \ll 1$, Eq. (6.9) reduces to Eq. (5.1).

Thus, the following expression for T_1^{-1} can be written down as follows:

$$\frac{1}{T_1} \approx \gamma_N^2 b_Q^2 \Delta E^2 \frac{(\tau_- \tau_0)^2}{(\tau_- + \tau_0)^3}. \tag{6.10}$$

The characteristic times τ_- and τ_0 are determined by probabilities of phonon-assisted transitions between the configurations with charged and neutral nearest acceptor. The assumption, that can be done to estimate the value of this times, is to assume that these transitions correspond to the hopping of a hole between two acceptors near the donor site [see figure 6.6(a)]. Denoting the hole energy at the nearest acceptor by ϵ_-, and at the second nearest acceptor as ϵ_0, the following expressions for τ_- and τ_0 can be written:

$$\tau_- = \frac{\tau_{\text{ph}}}{n_{\text{ph}}}, \tau_0 = \frac{\tau_{\text{ph}}}{n_{\text{ph}} + 1}, \tag{6.11}$$

where τ_{ph} is the characteristic time of the corresponding phonon-assisted transition, n_{ph} is the number of phonons given by the Planck distribution:

$$n_{\text{ph}} = \frac{1}{1 + \exp\left[\Delta\epsilon / (k_B T)\right]}, \tag{6.12}$$

and $\Delta\epsilon = \epsilon_- - \epsilon_0$.

As a result, the following expression for T_1 can be written

$$\frac{1}{T_1} \approx \gamma_N^2 b_Q^2 \Delta E^2 \tau_{\text{ph}} \times \frac{\left[1 - \exp\left(-\Delta\epsilon / k_B T\right)\right] \exp\left(-\Delta\epsilon / k_B T\right)}{\left[1 + \exp\left(-\Delta\epsilon / k_B T\right)\right]^3}. \tag{6.13}$$

Equation (6.13) was used to calculate the temperature dependence of T_1. First, the estimate $\Delta\epsilon$ and ΔE^2 was provided. These quantities are determined from the Coulomb energies and electric fields of two charges located at distances $r_{\mathrm{DA}}^{(1)}$ and $r_{\mathrm{DA}}^{(2)}$ from the donor to two nearest acceptors. As an estimate for these distances: the maxima of the first and second neighboring acceptor distributions have been taken into account:

$$\begin{aligned} F_{\mathrm{DA}}^{(1)} &= 4\pi r_{\mathrm{DA}}^2 n_{\mathrm{A}} \exp\left(-\frac{4}{3}\pi r_{\mathrm{DA}}^3 n_{\mathrm{A}}\right), \\ F_{\mathrm{DA}}^{(2)} &= \frac{16}{3}\pi^2 r^5 n_{\mathrm{A}}^2 \exp\left(-\frac{4}{3}\pi r^3 n_{\mathrm{A}}\right). \end{aligned} \tag{6.14}$$

The obtained distributions are demonstrated in figure 6.7(a) for sample B. The maxima of these distributions are given by

$$\begin{aligned} R_{\mathrm{DA}}^{(1)} &= (2\pi n_{\mathrm{A}})^{-1/3}, \\ R_{\mathrm{DA}}^{(2)} &= \left(\frac{4}{5}\pi n_{\mathrm{A}}\right)^{-1/3}. \end{aligned} \tag{6.15}$$

Thus,

$$\begin{aligned} \Delta\epsilon &= -\frac{e^2}{4\pi\epsilon\epsilon_0}\left[\frac{1}{R_{\mathrm{DA}}^{(1)}} - \frac{1}{R_{\mathrm{DA}}^{(2)}}\right], \\ \Delta E^2 &= \left(\frac{e}{4\pi\epsilon\epsilon_0}\right)^2 \left[\left(\frac{1}{R_{\mathrm{DA}}^{(1)}}\right)^4 + \left(\frac{1}{R_{\mathrm{DA}}^{(2)}}\right)^4\right], \end{aligned} \tag{6.16}$$

where squared electric field over angular distribution of the two acceptors is averaged.

Equation (6.13) together with Eqs.(6.2) and (6.16) leaves the only fitting parameter, τ_{ph}, to reproduce the measured low-field temperature dependence of the nuclear spin relaxation time shown in figure 6.5. The suppression of the spin relaxation by application of the magnetic field can be calculated from this value of T_1 using the motional narrowing formula 6.1:

$$T_1(B) = \frac{T_1}{1+\omega_B^2\tau_c^2}. \tag{6.17}$$

The results of the fitted data are shown in Figs. 6.4 and 6.5 by solid lines. One can see that the agreement between experimental data and theory is quite reasonable: there is no suppression of the nuclear spin relaxation up to 120 G (no magnetic-field dependence) and the stabilizing of spin relaxation at $T \gtrsim 10$ K is well reproduced assuming $\tau_{\mathrm{ph}} = 5\ \mu s$ in sample A and $\tau_{\mathrm{ph}} = 3\ \mu s$ in sample B. τ_{ph} obtained by fitting experimental data shows the correct functional behavior for the acceptor concentration. The phonon-assisted hops become more frequent with decreasing the average distance between the nearest acceptors. However, since the overlap of wave functions of impurity-bound holes decreases exponentially with growing distance, it is fair to assume a more significant difference in τ_{ph} between the two studied p-GaAs samples. This could mean that the presented model considering only two nearest acceptors is too simplistic. In the interests of clarifying this issue, detailed experimental investigations of nuclear spin relaxation over a broad range of doping in *p*-GaAs are needed.

6.4 Conclusions

Summing up the results of the current chapter, the relaxation of nuclear spin polarization created by optical pumping in bulk *p*-GaAs has been experimentally studied. The nuclear spin-lattice relaxation time T_1 in the absence of optical pumping belongs to the subsecond range and turns out to be longer than that under pumping. Turns out that T_1 in bulk *p*-GaAs is three orders of magnitude shorter than in *n*-GaAs. This result looks very unusual since the hyperfine coupling of holes is much weaker than that of conduction-band electrons. This paradox was solved by taking into account charge fluctuations at acceptors located in close vicinity of positively charged donor centers. The proposed theoretical model quantitatively describes the slowing down of nuclear spin relaxation below $T = 10$ K (due to slowing down of charge fluctuations), and magnetic-field independence (up to ≈ 100 G) of T_1. Reported results extend the general picture of nuclear spin relaxation in doped GaAs, where *p*-type doping has not been fully explored.

7 Summary

The present thesis contributes to the research field of semiconductor nuclear spin physics. In this work, the nuclear spin dynamics of a donor-bound electron was studied in GaAs with n and p doping via optical spectroscopy technique.

In chapter 4, the spin dynamics of localized donor-bound electrons interacting with the nuclear spin ensemble in n-doped GaAs epilayers is studied using nuclear spin polarization by light with modulated circular polarization. It was shown that the observed buildup of the nuclear spin polarization is a result of competition between nuclear spin cooling and the nuclear spin warm up in the oscillating Knight field. The developed model allows us to explain the dependence of nuclear spin polarization on the modulation frequency and to estimate the equilibration time of the NSS that appears to be shorter than the transverse relaxation time T_2 determined from nuclear magnetic resonance.

Another focus point of this thesis is studying the nuclear spin dynamics in the subsecond time range, which is most strongly manifested by the dynamics of nuclei associated with an electron at the donor. In chapter 5, the method of time-resolved detection of the Hanle effect and polarized photoluminescence with dark intervals was used to investigate the buildup and decay of the spin polarization of nuclei interacting with the donor-bound electrons in n-doped GaAs. It was shown that strong hyperfine coupling defines the millisecond time scale of the spin dynamics of these nuclei, as distinct from the nuclei far from impurity centers, characterized by a thousand times longer spin-relaxation time. The dynamics of spin polarization and relaxation attributed to the nuclei inside the donor orbit is observed on the time scale from 200 to 425 ms. The optical cooling dynamics of nuclei located inside the donor orbit in n-doped GaAs was also studied. This dynamics show that at slow modulation of excitation polarization $T_{\mathrm{mod}} \sim 1$ s, a noticeable Overhauser field can be observed. It was demonstrated that the initial cooling rate is strongly dependent on the direction of the external magnetic field concerning the initial electron polarization direction $\pm|S_0|$. The nuclear spin dynamics revealed in response times of 220 ms and 780 ms, attributed to the nuclei inside the donor orbit in n-GaAs is observed. The lowest nuclear spin temperature in n-GaAs, $\Theta_N = 1$ mK was achieved in this work after cooling for $T_{\mathrm{mod}} \sim 1$ s.

It was found that relaxation of nuclei in n-GaAs is dominated by the diffusion-limited hyperfine relaxation and quadrupole warmup in lightly doped dielectric crystals and by hyperfine relaxation involving both itinerant (Korringa mechanism) and localized electrons in heavily doped samples with the metallic conductivity. In what concerns p-GaAs, even the timescale of the nuclear spin-lattice relaxation has not been precisely known. Following the information that is already available for n-GaAs, in chapter 6, the spin-lattice relaxation of the NSS in p-type GaAs is studied using a three-stage experimental protocol including optical pumping and measuring the difference of the nuclear spin polarization before and after a dark interval of variable length. This method provided the spin-lattice relaxation time T_1 of optically pumped nuclei “in the dark”, that is, in the absence of illumination. The measured T_1 values fall into the subsecond time range, being three orders of magnitude shorter than that has been observed in n-type GaAs in chapter 5. The drastic difference is further emphasized by magnetic-field and temperature dependencies of T_1 in p-GaAs, showing no similarity to those in n-GaAs. This unexpected behavior finds its explanation in the spatial selectivity of the optical pumping in p-GaAs, which is only efficient in the vicinity of shallow donors, together with the quadrupole relaxation of nuclear spins, which is induced by electric fields within closely spaced donor-acceptor pairs. The developed theoretical model explains the whole set of experimental results.

To summarize, this thesis sheds some more light on the complex interdependent system formed by the electron spin and the ensemble of surrounding nuclear spins in the conventional semiconductor — the bulk GaAs. I believe that this work is another step towards the understanding of this challenging system that can lead to implementations in future quantum information technologies.

List of Figures

List of Acronyms

GaAs	Gallium Arsenide
dc	Direct Current
ac	Alternating Current
PL	Photoluminescence
NMR	Nuclear Magnetic Resonance
f.c.c.	Face-Centered-Cubic
hh	Heavy-Hole
lh	Light-Hole
so	Split-Off
NESD	Non-Equilibrium Spin Distribution
HWHM	Halfwidth on the Half Maximum
NSS	Nuclear Spin System
EFG	Electric Field Gradient
QD	Quantum Dot
MagnCryo	Magnetic Cryostat
UV	Ultra-Violet
AOM	Acousto-Optical Modulator
RF	Radio Frequency
EOM	Electro-Optical Modulator
TTL	Time To Live Modulator
PEM	Photoelastic Modulator
CW	Continuous Wave
Nd:YAG	Neodymium-Doped Yttrium Aluminum Garnet
GT	Glan-Teylor
CCD	Charge-Coupled Device
APD	Avalanche Photodiode
PC	Personal Computer
GPIB	General Purpose Interface Bus
PCS	Photon-Counting System
PCI	Peripheral Component Interconnect
PRC	Polarization Recovery Curve
3D	Three-Dimensional
NIM	Nuclear Instrument Modules
PR	Polarization Recovery
CBA	Band-To-Acceptor

List of Symbols

E_g	Bandgap energy
Γ	Center of the Brillouin zone
E_c	Valence band energy
E_v	Conduction band energy
E_{so}	Split-off band energy
V_1	Heavy-hole band
V_2	Light-hole band
V_3	Split-off band
Δ	Split-off band energy
ψ_{km}^c	The Bloch function
u_m	The Bloch amplitudes
ϵ_c	Energy spectra near Γ-point
$\hbar$	The Planck constant
$\mathbf{k}$	Wave vector
m_e	Electron effective mass
$\hat{H}$	The Hamiltonian
$\hat{\sigma}$	The Pauli matrices
$\Omega_{x,y,z}$	The Dresselhaus terms
α	Dimensionless coefficient
x, y, z	Coordinate axes
M	Magnetization projection
$J_{x,y,z}$	Angular momentum operators
ϵ_M	Energy spectrum values
χ_M	Energy spectrum coefficients
$\gamma_1, \gamma_2, \gamma_3$	The Latinger's parameters
m_0	Free electron mass
m_h	Heavy-hole mass
m_l	Ligh-hole mass
A, B	Quantities related to the effective masses of light and heavy holes
ϵ	Energy
I	PL intensity
$F_{mm'}$	The density matrix of thermalized electrons
D_{mM}	Dipole moments amplitudes
$e_{x,y}$	Unit vectors perpendicular to the direction of the light beam
$\hat{D}$	Dipole moment operator
Ψ	Wave function

t	Time
S	The average spin of the thermalized electrons
S_0	The average spin of the photoexcited electrons
τ	Electron lifetime
τ_s	Electron spin relaxation time
ω	Frequency
g	g-factor
B	Magnetic field
μ_B	Bohr magneton
T_s	Electron spin lifetime
Ω	The Larmor frequency
T	Temperature
P_{exc}	Excitation power
ρ_c	Circular polarization degree
W	Lifetime distributions function
$B_{1/2}$	HWHM of the Hanle curve
L	Diffusion length
D	Diffusion coefficient
T_1	Spin-lattice relaxation time
B_L	Local magnetic field
μ_I	Nuclear magnetic moment
a	Lattice constant
T_2	Spin-spin relaxation time
Θ	Deflecting angle
Θ_N	Nuclear spin temperature
k_B	The Boltzmann constant
H_Z	The Zeeman energy Hamiltonian
H_d	Spin-spin Hamiltonian
a_B	The Bohr radius
A_n	Hyperfine constant
B_N	Nuclear field
τ_c	Electron correlation time
θ	The angle between the magnetic field and an exciting light
g_n	Nuclear g-factor
v_0	Unit cell volume
H_{hf}	The Hamiltonian of the interaction between an electron and nuclear spins
a_n	Hyperfine constant normalized by the volume occupied by the electron
I_n	Nuclear spin operator
ω_N	Nuclear spin precession frequency
T_{1e}	Nuclear spin relaxation time due to interaction with electrons
r_0	Donor site radius
F	Filling factor
n	The concentration of bound electrons

N_D	Donor concentration
π	Pi (number)
H_Q	The Hamiltonian of the quadrupole interaction
$V_{\alpha\beta}$	Quadrupole interaction coefficients
H_{dd}	The Hamiltonian of the dipole-dipole interaction
$\mathbf{r}_{nm}$	Translation vector between n and m nuclei
d	Distance between neighboring nuclei
χ_N	Paramagnetic susceptibility
b_N	Total nuclear field created by nuclei of the same isotope
β	Reciprocal spin temperature
B_e	The Knight field
ξ	Numerical factor dependent on spin-spin interaction
λ	Light wavelength
v	Acoustic velocity in the crystal
f_{mod}	Frequency of the modulation
f	Focal distance
D_B	Beam diameter
U	Voltage
T_{mod}	Modulation period
I_{+-}	co/cross intensities of the detected light
σ^{+-}	Helicity of the pumping light
$\omega_{1/2}$	Cut-off frequency
n_d	Donor concentration
E_{exc}	Excitation energy
E_{det}	Detection energy
ρ_∞	Polarization degree reached in the limit of large magnetic fields
ρ_{sat}	Polarization saturation degree
A_{PR}	Amplitude of the polarization recovery curve
Δ_{PR}	HWHM of the polarization recovery curve
B_{eff}	Effective magnetic field
Q	Nuclear spin number
j	Spin flow
q_s	Energy flow
γ_N	Nuclear gyromagnetic ratio
I_B	Projection of the average nuclear spin on the direction of the electron field
$\hat{\chi}$	Magnetic susceptibility
G_N	The Green function
δ	The Dirac delta function
C_N	NSS heat capacity
G_ω	Nuclear spin correlator
ω_{hf}	Hyperfine frequency
T_{bulk}	Nuclear spin diffusion time
Δt	Delay time

$B_{\sum}$	Total magnetic field
T_{repump}	Characteristic repumping time
$n_{\perp,\parallel}$	Relaxation time fitting parameters
T_{det}	Detection time
T_{resp}	Response time
ρ_g	The distribution function of the electron g-factors
τ_{c0}	Correlation time at zero magnetic field and temperature
b_{ex}	Spectral power density
J	Exchange constant
T_{ND}	Spin relaxation time in the dark due to interaction with electrons
P_N	Nuclear polarization
T_{NB}	Nuclear spin relaxation time in the presence of optical pumping
B_Q	Quadrupole field
R_{DA}	Maximal distance between the donor and nearest acceptor
n_A	Acceptor concentration
E	Electric field
β_Q	Experimentally determined isotope-dependent constant
ω_N	Nuclear Larmor frequency
E_0	Electric charge
τ_-	The average time during which the nearest acceptor stays charged
τ_0	The average time during which the nearest acceptor is neutral
E_f	Fluctuating electric field
B_ω	Quadrupole-induced effective magnetic field
ϵ_-	Energy at the nearest acceptor
ϵ_0	Energy at the second nearest acceptor
τ_{ph}	Characteristic time of the corresponding phonon-assisted transition
n_{ph}	Number of photons given by the Planck distribution
$F_{\mathrm{DA}}^{1,2}$	Distances of the first and second neighboring acceptor distributions
$r_{\mathrm{DA}}^{1,2}$	Distances from the donor to two nearest acceptors
$R_{\mathrm{DA}}^{1,2}$	Maxima of the distances of the first and second neighboring acceptor distributions

Publications and Conference contributions

Publications

- Nuclear spin cooling by helicity-alternated optical pumping at weak magnetic fields in n-GaAs,
  P. S. Sokolov, M. Yu. Petrov, K. V. Kavokin, A. S. Kurdyubov M. S. Kuznetsova, R. V. Cherbunin, S. Yu. Verbin, N. K. Poletaev, D. R. Yakovlev, D. Suter, and M. Bayer,
  Phys. Rev. B **96**, 205205, 2017.

- Spin-lattice relaxation of optically polarized nuclei in p-type GaAs,
  M. Kotur, R. I. Dzhioev, M. Vladimirova, R. V. Cherbunin, **P. S. Sokolov**, D. R. Yakovlev, M. Bayer, D. Suter, and K. V. Kavokin,
  Phys. Rev. B **97**, 165206, 2018.

- Subsecond nuclear spin dynamics in n-GaAs,
  P. S. Sokolov, M. Yu. Petrov, K. V. Kavokin, M. S. Kuznetsova, S. Yu. Verbin, I. Ya. Gerlovin, D. R. Yakovlev, and M. Bayer,
  Phys. Rev. B **99**, 075307, 2019.

- Light-driven nuclei thermodynamics in bulk GaAs and (In,Ga)As/GaAs quantum dots,
  P. S. Sokolov, M. Yu. Petrov, K. V. Kavokin, M. S. Kuznetsova, S. Yu. Verbin, D. Reuter, A. D. Wieck, D. R. Yakovlev, and M. Bayer,
  In preparation for *Phys. Rev. B*

Conferences

- 13th International Workshop on Nonlinear Optics and Excitation Kinetics in Semiconductors, Dortmund, 9–13 October 2016.

- The 18th International Conference on Physics of Light-Matter Coupling in Nanostructures, Würzburg, 9–14 July 2017

- E. F. Gross-Symposium: Excitons in Crystals and Nanostructures, St. Petersburg, 10–12 October 2017.

- Joint Meeting of the DPG and EPS Condensed Matter Divisions, Berlin, 11–16 March 2018.

- 50 Years of Optical Orientation in Semiconductors, Paris, 18–19 June 2018.

- The 34th International Conference on the Physics of Semiconductors, Montpellier, 29 Juli – 3 August 2018.
- Joint Meeting of the Sections for Atomic, Molecular, Plasma Physics and Quantum Optics (SAMOP), Condensed Matter (SKM) and Matter and Cosmos (SMuK): Quantum Science and Information Technologies, Freiburg, 23–27 September 2019.

Bibliography

[A19] Elent A. Teo2 blanks for acousto-optical modulators, 2019.

[Abr61] Anatole Abragam. *The principles of nuclear magnetism.* Number 32. Oxford university press, 1961.

[AP58] A Abragam and WG Proctor. Spin temperature. *Physical Review*, 109(5):1441, 1958.

[APBS74] A. Abragam, V. I. Perel, V. L. Berkovits, and V. I. Safarov. *Proc. XII Int. Conf. on the Physics of Semiconductors, Stuttgart, ed. M. H. Pilkuhn*, 1974.

[APE05] APE. Acoustooptical intensity modulator manual, 2005.

[BFN$^+$11] H Bluhm, S Foletti, I Neder, M Rudner, D Mahalu, V Umansky, and A Yacoby. Dephasing time of gaas electron-spin qubits coupled to a nuclear bath. *Nat. Phys*, 7(2), 2011.

[BKYB17] VV Belykh, KV Kavokin, DR Yakovlev, and M Bayer. Electron charge and spin delocalization revealed in the optically probed longitudinal and transverse spin dynamics in n-gaas. *Physical Review B*, 96(24):241201, 2017.

[BMMP63] E Brun, RJ Mahler, H Mahon, and WL Pierce. Electrically induced nuclear quadrupole spin transitions in a gaas single crystal. *Physical Review*, 129(5):1965, 1963.

[BS78] VL Berkovits and VI Safarov. Optical detection of nuclear quadrupole resonance in doped semiconductors. *Sov. Phys. Solid State,*, 20(8):1468–1469, 1978.

[BW54] N Bloembergen and S Wang. Relaxation effects in para-and ferromagnetic resonance. *Physical Review*, 93(1):72, 1954.

[CGCA70] M Chapellier, M Goldman, Vu Hoang Chau, and A Abragam. Production and observation of a nuclear antiferromagnetic state. *Journal of Applied Physics*, 41(3):849–853, 1970.

[CRWB11] YS Chen, D Reuter, AD Wieck, and G Bacher. Dynamic nuclear spin resonance in n-gaas. *Physical review letters*, 107(16):167601, 2011.

[CUZ⁺17] EA Chekhovich, A Ulhaq, E Zallo, F Ding, OG Schmidt, and MS Skolnick. Measurement of the spin temperature of optically cooled nuclei and gaas hyperfine constants in gaas/algaas quantum dots. *Nature materials*, 16(10):982, 2017.

[DKK⁺02] RI Dzhioev, KV Kavokin, VL Korenev, MV Lazarev, B Ya Meltser, MN Stepanova, BP Zakharchenya, D Gammon, and DS Katzer. Low-temperature spin relaxation in n-type gaas. *Physical Review B*, 66(24):245204, 2002.

[DKM⁺02] RI Dzhioev, VL Korenev, IA Merkulov, BP Zakharchenya, D Gammon, Al L Efros, and DS Katzer. Manipulation of the spin memory of electrons in n-gaas. *Physical review letters*, 88(25):256801, 2002.

[DP75] MI D'yakonov and VI Perel. Cooling of a system of nuclear spins following optical orientation of electrons in semiconductors. *Soviet Journal of Experimental and Theoretical Physics*, 41:759, 1975.

[Dya17] Michel I Dyakonov. *Spin physics in semiconductors*, volume 1. Springer, 2017.

[ELFS02] Marcus Eickhoff, Björn Lenzman, Gregory Flinn, and Dieter Suter. Coupling mechanisms for optically induced nmr in gaas quantum wells. *Physical Review B*, 65(12):125301, 2002.

[ES04] Marcus Eickhoff and Dieter Suter. Pulsed optically detected nmr of single gaas/algaas quantum wells. *Journal of Magnetic Resonance*, 166(1):69–75, 2004.

[EW14] Norman G Einspruch and William R Wisseman. Gaas microelectronics: Vlsi electronics microstructure science. volume 11. Academic Press, 2014.

[FKI⁺15] Abram L Falk, Paul V Klimov, Viktor Ivády, Krisztián Szász, David J Christle, William F Koehl, Ádám Gali, and David D Awschalom. Optical polarization of nuclear spins in silicon carbide. *Physical review letters*, 114(24):247603, 2015.

[Fra09] Alexander Franzen. Component library: a vector graphics library for illustrations of optics experiments, 2009.

[GCG⁺13] Rakshyakar Giri, Steeve Cronenberger, MM Glazov, KV Kavokin, A Lemaître, J Bloch, Maria Vladimirova, and Denis Scalbert. Nondestructive measurement of nuclear magnetization by off-resonant faraday rotation. *Physical review letters*, 111(8):087603, 2013.

[GCV⁺12] Rakshyakar Giri, Steeve Cronenberger, Maria Vladimirova, Denis Scalbert, KV Kavokin, MM Glazov, Michal Nawrocki, Aristide Lemaître, and Jacqueline Bloch. Giant photoinduced faraday rotation due to the spin-polarized electron gas in an n-gaas microcavity. *Physical Review B*, 85(19):195313, 2012.

[Gol08] M Goldman. Overview of spin temperature, thermal mixing and dynamic nuclear polarization. *Applied Magnetic Resonance*, 34(3-4):219–226, 2008.

[GSY$^+$07] A Greilich, A Shabaev, DR Yakovlev, Al L Efros, IA Yugova, D Reuter, AD Wieck, and M Bayer. Nuclei-induced frequency focusing of electron spin coherence. *Science*, 317(5846):1896–1899, 2007.

[GYS$^+$06] A Greilich, DR Yakovlev, A Shabaev, Al L Efros, IA Yugova, R Oulton, V Stavarache, D Reuter, A Wieck, and M Bayer. Mode locking of electron spin coherences in singly charged quantum dots. *Science*, 313(5785):341–345, 2006.

[Han91] Wilhelm Hanle. Über magnetische beeinflussung der polarisation der resonanzfluoreszenz. *Zeitschrift für Physik D Atoms, Molecules and Clusters*, 18(1):5–10, 1991.

[HB16] Fritz Henneberger and Oliver Benson. *Semiconductor quantum bits*. Pan Stanford, 2016.

[HBDM$^+$01] Robin K Harris, Edwin D Becker, Sonia M Cabral De Menezes, Robin Goodfellow, and Pierre Granger. Nmr nomenclature. nuclear spin properties and conventions for chemical shifts (iupac recommendations 2001). *Pure and Applied Chemistry*, 73(11):1795–1818, 2001.

[HZG$^+$15] F Heisterkamp, EA Zhukov, A Greilich, DR Yakovlev, VL Korenev, A Pawlis, and M Bayer. Longitudinal and transverse spin dynamics of donor-bound electrons in fluorine-doped znse: Spin inertia versus hanle effect. *Physical Review B*, 91(23):235432, 2015.

[Ins19] HINDS Instruments. Pem 100 photoelastic modulator: User manual, 2019.

[JH80] C Julien and C Hirlimann. Ebert-fastie monochromator alignment. *Journal of Physics E: Scientific Instruments*, 13(9):923, 1980.

[KA98] J. M. Kikkawa and D. D. Awschalom. Resonant spin amplification in n-type GaAs. *Physical Review Letters*, 1998.

[KA99a] J. M. Kikkawa and D. D. Awschalom. Lateral drag of spin coherence in gallium arsenide. *Nature*, 1999.

[KA99b] JM Kikkawa and DD Awschalom. Lateral drag of spin coherence in gallium arsenide. *Nature*, 397(6715):139, 1999.

[Kav08] KV Kavokin. Spin relaxation of localized electrons in n-type semiconductors. *Semiconductor Science and Technology*, 23(11):114009, 2008.

[KDV$^+$16] M Kotur, RI Dzhioev, Maria Vladimirova, Benoit Jouault, VL Korenev, and KV Kavokin. Nuclear spin warm up in bulk n-gaas. *Physical Review B*, 94(8):081201, 2016.

[KDV$^+$18] M Kotur, RI Dzhioev, Maria Vladimirova, RV Cherbunin, PS Sokolov, DR Yakovlev, M Bayer, D Suter, and KV Kavokin. Spin-lattice relaxation of optically polarized nuclei in p-type gaas. *Physical Review B*, 97(16):165206, 2018.

[Khu69] GR Khutsishvili. Spin diffusion and nuclear magnetic relaxation in a crystal containing a magnetic impurity. *Soviet Physics Uspekhi*, 11(6):802, 1969.

[KLG03] Alexander Khaetskii, Daniel Loss, and Leonid Glazman. Electron spin evolution induced by interaction with nuclei in a quantum dot. *Physical Review B*, 67(19):195329, 2003.

[Lam68] Georges Lampel. Nuclear dynamic polarization by optical electronic saturation and optical pumping in semiconductors. *Physical Review Letters*, 20(10):491, 1968.

[Lan96] LD Landau. *Course of Theoretical Physics Volume 9 Statistical Physics Part 1.* Heinemann, Oxford, 1996.

[LG67] IJ Lowe and S Gade. Density-matrix derivation of the spin-diffusion equation. *Physical Review*, 156(3):817, 1967.

[LHZ$^+$09] C Latta, A Högele, Y Zhao, AN Vamivakas, P Maletinsky, M Kroner, J Dreiser, I Carusotto, A Badolato, D Schuh, et al. Confluence of resonant laser excitation and bidirectional quantum-dot nuclear-spin polarization. *Nature Physics*, 5(10):758, 2009.

[LMBI06] CW Lai, P Maletinsky, A Badolato, and Atac Imamoglu. Knight-field-enabled nuclear spin polarization in single quantum dots. *Physical Review Letters*, 96(16):167403, 2006.

[MBI07] P Maletinsky, A Badolato, and Atac Imamoglu. Dynamics of quantum dot nuclear spin polarization controlled by a single electron. *Physical Review Letters*, 99(5):056804, 2007.

[MBSA01] I Malajovich, JJ Berry, Nitin Samarth, and DD Awschalom. Persistent sourcing of coherent spins for multifunctional semiconductor spintronics. *Nature*, 411(6839):770, 2001.

[McL86] M McLean. *Encyclopedia of materials science and technology.* Taylor & Francis, 1986.

[MER02] IA Merkulov, Al L Efros, and M Rosen. Electron spin relaxation by nuclei in semiconductor quantum dots. *Physical review B*, 65(20):205309, 2002.

[MKI09] P Maletinsky, M Kroner, and A Imamoglu. Demagnetization of quantum dot nuclear spins: breakdown of the nuclear spin temperature approach. *arXiv preprint arXiv:0901.2289*, 2009.

[MKS+11] MN Makhonin, KV Kavokin, P Senellart, A Lemaître, AJ Ramsay, MS Skolnick, and AI Tartakovskii. Fast control of nuclear spin polarization in an optically pumped single quantum dot. *Nature materials*, 10(11):844, 2011.

[MMC+17] Filip K Malinowski, Frederico Martins, Łukasz Cywiński, Mark S Rudner, Peter D Nissen, Saeed Fallahi, Geoffrey C Gardner, Michael J Manfra, Charles M Marcus, and Ferdinand Kuemmeth. Spectrum of the nuclear environment for gaas spin qubits. *Physical review letters*, 118(17):177702, 2017.

[MZ12] Felix Meier and Boris Petrovich Zakharchenya. *Optical orientation.* Elsevier, 2012.

[Nan13] Oxford Instruments Omicron NanoScience. Microstat he2 / microstat he2 rectangular tail optistat cf-v2 Operator's Handbook, 2013.

[OIS+14] M Ono, Jun Ishihara, G Sato, S Matsuzaka, Y Ohno, and H Ohno. Strain and origin of inhomogeneous broadening probed by optically detected nuclear magnetic resonance in a (110) gaas quantum well. *Physical Review B*, 89(11):115308, 2014.

[OL97] AS Oja and OV Lounasmaa. Nuclear magnetic ordering in simple metals at positive and negative nanokelvin temperatures. *Reviews of Modern Physics*, 69(1):1, 1997.

[OYB+99] Y Ohno, DK Young, B al Beschoten, F Matsukura, H Ohno, and DD Awschalom. Electrical spin injection in a ferromagnetic semiconductor heterostructure. *Nature*, 402(6763):790, 1999.

[Pag81] Daniel Paget. Optical detection of nmr in high-purity gaas under optical pumping: Efficient spin-exchange averaging between electronic states. *Physical Review B*, 24(7):3776, 1981.

[Pag82] Daniel Paget. Optical detection of nmr in high-purity gaas: Direct study of the relaxation of nuclei close to shallow donors. *Physical Review B*, 25(7):4444, 1982.

[PAK08] Daniel Paget, Thierry Amand, and J-P Korb. Light-induced nuclear quadrupolar relaxation in semiconductors. *Physical Review B*, 77(24):245201, 2008.

[Par69] RR Parsons. Band-to-band optical pumping in solids and polarized photoluminescence. *Physical Review Letters*, 23(20):1152, 1969.

[PLSS77] D Paget, G Lampel, B Sapoval, and VI Safarov. Low field electron-nuclear spin coupling in gallium arsenide under optical pumping conditions. *Physical review B*, 15(12):5780, 1977.

[Pob07] Frank Pobell. *Matter and methods at low temperatures*, volume 2. Springer, 2007.

[PP51] Edward M Purcell and Robert V Pound. A nuclear spin system at negative temperature. *Physical Review*, 81(2):279, 1951.

[QIO19] QIOPTIQ. Laser modulator series lm 0202 - operating instructions, 2019.

[RKS+16] Ivan I Ryzhov, Gleb G Kozlov, Dmitrii S Smirnov, Mikhail M Glazov, Yurii P Efimov, Sergei A Eliseev, Viacheslav A Lovtcius, Vladimir V Petrov, Kirill V Kavokin, Alexey V Kavokin, et al. Spin noise explores local magnetic fields in a semiconductor. *Scientific reports*, 6:21062, 2016.

[Sca17] Denis Scalbert. Nuclear polaron beyond the mean-field approximation. *Physical Review B*, 95(24):245209, 2017.

[SCK00] E Fred Schubert, Jaehee Cho, and Jong Kyu Kim. *Light-emitting diodes*. Wiley Online Library, 2000.

[SFK+01] G Salis, DT Fuchs, JM Kikkawa, DD Awschalom, Y Ohno, and H Ohno. Optical manipulation of nuclear spin by a two-dimensional electron gas. *Physical review letters*, 86(12):2677, 2001.

[SKM+06] H Sanada, Y Kondo, S Matsuzaka, K Morita, CY Hu, Y Ohno, and H Ohno. Optical pump-probe measurements of local nuclear spin coherence in semiconductor quantum wells. *Physical review letters*, 96(6):067602, 2006.

[SN06] Simon M Sze and Kwok K Ng. *Physics of semiconductor devices*. John wiley & sons, 2006.

[SPK+17] PS Sokolov, M Yu Petrov, KV Kavokin, AS Kurdyubov, MS Kuznetsova, RV Cherbunin, S Yu Verbin, NK Poletaev, DR Yakovlev, D Suter, et al. Nuclear spin cooling by helicity-alternated optical pumping at weak magnetic fields in n-gaas. *Physical Review B*, 96(20):205205, 2017.

[SPK+19] PS Sokolov, M Yu Petrov, KV Kavokin, MS Kuznetsova, S Yu Verbin, I Ya Gerlovin, DR Yakovlev, and M Bayer. Subsecond nuclear spin dynamics in n-gaas. *Physical Review B*, 99(7):075307, 2019.

[UMA+13] Bernhard Urbaszek, Xavier Marie, Thierry Amand, Olivier Krebs, Paul Voisin, Patrick Maletinsky, Alexander Högele, and Atac Imamoglu. Nuclear spin physics in quantum dots: An optical investigation. *Reviews of Modern Physics*, 85(1):79, 2013.

[VCS+17] Maria Vladimirova, Steeve Cronenberger, Denis Scalbert, M Kotur, RI Dzhioev, II Ryzhov, GG Kozlov, VS Zapasskii, A Lemaître, and KV Kavokin. Nuclear spin relaxation in n-gaas: From insulating to metallic regime. *Physical Review B*, 95(12):125312, 2017.

[VCS+18] Maria Vladimirova, Steeve Cronenberger, Denis Scalbert, II Ryzhov, VS Zapasskii, GG Kozlov, A Lemaître, and KV Kavokin. Spin temperature concept verified by optical magnetometry of nuclear spins. *Physical Review B*, 97(4):041301, 2018.

[WE24] RW Wood and Alexander Ellett. Polarized resonance radiation in weak magnetic fields. *Physical Review*, 24(3):243, 1924.

[WH77] Claude Weisbuch and Claudine Hermann. Optical detection of conduction-electron spin resonance in gaas, ingaas, and algaas. *Physical Review B*, 15(2):816, 1977.

[Wik19] Wikipedia. Photoluminescence, 2019.